CLOUD DROP EFFECTIVE RADIUS FOR TRADE WIND CUMULI OBSERVED DURING RICO BY AIRCRAFT AND MODIS

BY

CONOR O. HANEY

THESIS

Submitted in partial fulfillment of the requirements
for the degree of Master of Science in Atmospheric Sciences
in the Graduate College of the
University of Illinois at Urbana-Champaign, 2013

Urbana, Illinois

Adviser:

Professor Larry Di Girolamo

ABSTRACT

Warm, tropical boundary clouds represent one of the biggest sources of uncertainty in climate sensitivity to anthropogenic forcing. Information useful for gaining a better understanding about such clouds is relatively plentiful from satellites. But warm tropical clouds, such as those found in the trades, are often horizontally heterogeneous over the pixel scales of meteorological satellite imagers; the clouds may even be sub-pixel in size. Due to the 1-D nature of the radiative transfer calculations used in retrieving cloud drop effective radius and cloud optical depth from satellites, systematic errors in the satellite retrievals can be introduced due to the 3-D radiative transfer through heterogeneous clouds found in nature. To date, validation for these satellite retrievals of cloud properties have been for stratiform clouds, not for cumulus. Here, we use in-situ aircraft measurements from RICO ("Rain In shallow Cumulus over the Ocean") for these cumuli, and investigate how they compare to satellite retrievals from MODIS ("Moderate Resolution Imaging Spectroradiometer"). In doing so, the vertical structure of the cloud drop effective radius and liquid water content of these trade-wind cumuli are also investigated from the FSSP-100 and 2D-C cloud probes aboard the C-130 aircraft flown during RICO.

The constructed profiles show a general increase in cloud drop effective radius with increasing height up to around 2000 m altitude, followed by a decrease with height beyond that point, though with less samples. The liquid water content profile shows similar behavior. When using the aircraft data to compare to MODIS 2.1 μm band retrievals, the FSSP r_e mean is 10.8 μm, much smaller than the MODIS Terra mean $r_e(2.1)$ of 23.6 μm and Aqua mean $r_e(2.1)$ of 20.7 μm. The MODIS 3.7 μm band shows an r_e distribution closer to that of the aircraft, where the Terra mean $r_e(3.7)$ is 14.1 μm and the Aqua mean $r_e(3.7)$ is 15.0 μm. Analysis of the spatial

heterogeneity metric, H_σ, shows that the difference between the 2.1 µm and 3.7 µm band MODIS r_e retrievals show an increasingly large disparity as H_σ increases, where $r_e(2.1)$ is much larger than $r_e(3.7)$. The MODIS 2.1 µm band retrievals for more homogeneous clouds have a lower mean r_e of 17.7 µm compared to heterogeneous retrievals, while cloud optical depth retrievals for homogeneous clouds have a higher mean τ of 14.4, compared to 5.7 for heterogeneous clouds. This overestimation of effective radius and underestimation of optical depth is in line with what is expected when 3-D radiative transfer effects play a major role. The results of this study reinforce the fact that analysts should use caution when using such satellite retrievals.

ACKNOWLEDGEMENTS

I would like to thank my adviser, Larry Di Girolamo, for his endless wisdom and patience during this point in my life. His guidance brought me to the spot that I am at today, and I am extremely grateful to have been working for him for these past several years. I would also like to thank Bob Rauber for his guidance during this process and his knowledge of the specifics of the RICO campaign.

I would like to thank my friends and family for their continued support. Whether I'm going through good times or bad times, they have always been there for me when I've needed them most, and they always know how to make me smile.

We thank the NCAR Earth Observing Laboratory RICO scientists and staff for their efforts in the field. This research was supported by the National Science Foundation (NSF) under grants ATM-03-46172 and ATM-08-54954, and LARRYS NASA GRANTS.

TABLE OF CONTENTS

CHAPTER 1

INTRODUCTION

1.1 Overview

Clouds are among the most important influences on Earth's radiation budget, and are an essential part of many scientific studies of the atmosphere. Clouds have been shown to have strong impacts on radiative forcing, and the links between their susceptibility and factors such as aerosols and cloud droplet spectra have been explored in detail over the years (*Twomey, 1974; Platnick and Twomey,1994; Oreopoulos and Platnick, 2008*). While in-situ measurements of these clouds are highly sought after for scientific analysis, the infrequent occurrence of field campaigns severely limits analysis to the regions of the experiment. In addition to this, low quality data formats, improper handling on the data precision and uncertainty, and lack of properly updated documentation makes this data difficult to use. Satellites, however, offer the opportunity for frequent, global data coverage, and have the potential to give us an extensive timeline of data that we need for climate studies. Microphysical properties, such as effective radius and optical depth, are obtainable from satellite instruments using a popular technique involving simultaneously retrieving both properties by using a channel with a spectral wavelength in the visible region of the electromagnetic spectrum, and another channel with a near-infrared spectral wavelength (*Nakajima and King, 1990)*. This method is based upon the plane-parallel approximation, where it is assumed that all clouds are horizontally homogeneous and extend outward infinitely in the horizontal direction. This assumption is favorable for operational radiative transfer calculations, as it reduces the radiative transfer to a one-dimensional computation, where the radiation field only varies in the vertical direction. This in

turn makes for computationally fast calculations that allows for efficient operational processing of the vast amounts of satellite data collected each day. Past studies have shown that this one-dimensional assumption is a decent assumption for stratocumulus clouds observed under high sun (*Di Girolamo et al.,2010*). However, this assumption in general does not hold well; in reality no cloud is actually one-dimensional—clouds are three-dimensional, as they vary in both horizontal directions and vertical directions. This variation introduces 3-D radiative effects, for example where clouds next to each other may affect each other's emerging radiation field. This can cause more errors as the raw data is processed further down the line into higher level products. As the data becomes the input into an advanced algorithm, where the output of this algorithm is input into another algorithm, and so on, the errors in earlier stages of the process creates a larger potential for differences in later stages of the process. Level 2 cloud product processing for products such as cloud drop effective radius and cloud optical depth is an example of one of these higher processed forms that could potentially be affected in such a way. Why this happens, and how much this affects the product quantitatively, forms the basis for this study.

1.2 Background

First defined by *Hansen and Travis, (1974)*, cloud drop effective radius is a cross-sectional, area weighted mean of a droplet size distribution, and is defined as:

$$r_e = \frac{\int_0^\infty \pi \cdot r^3 \cdot n(r) dr}{\int_0^\infty \pi \cdot r^2 \cdot n(r) dr} \qquad \text{Eq. 1}$$

where r_e is the effective radius of the drop size distribution (hereafter referred to as just *effective radius*), r is the cloud droplet radius, and $n(r)dr$ is the number of cloud droplets with radii between r and $r+dr$.

Cloud optical depth is defined as:

$$\tau = \int_{z_b}^{z_t} \int_0^{\infty} \pi \; r^2 Q_s n(r) dr dz \qquad \text{Eq. 2}$$

where τ is the cloud optical depth (hereafter referred to as just *optical depth*), r is the cloud droplet radius, Q_s is the scattering efficiency (about 2 at visible wavelengths), z_b is the bottom of the cloud, and z_t is the top of the cloud.

For the MODIS instrument, both of these variables are retrieved in an operationally efficient manner, using a bispectral technique that utilizes pre-made *Look-Up Tables (LUT)* of various 1-D radiative transfer calculations done for different pairs of r_e and τ. The measured radiance (or reflection functions) at a visible channel and a near-infrared channel are used in these LUTs to retrieve r_e and τ. An example of this is shown in Figure 1.1, which is taken from *Nakajima and King (1990)*. Using the measured visible reflection function on the horizontal axis and the near infrared reflection function on the vertical axis, one can easily find the corresponding r_e and τ.

Since the LUT is constructed using 1-D radiative transfer from the plane-parallel approximation, this method works fairly well for stratocumulus clouds with only small margins of error, as prior validation studies have shown (*Nakajima et al., 2005*; *Platnick and Valero, 1995*; *Wetzel et. al., 2001*; *Nakajima et al., 1991*; *Szczodrak et al., 2001*; *Kuji et al., 2000*). However, in more recent studies, these assumptions for stratocumuli have been shown to demonstrate a small bias in r_e (*Bréon and Doutriaux-Boucher, 2005*; *King et al., 2013*; *Painemal and Zuidema, 2011*). Furthermore, other studies have shown that this does not hold so well for heterogeneous clouds, and in fact can lead to large systematic errors in retrievals for r_e and τ (e.g., *Marshak et al., 2006*). In particular, these errors often lead to an overestimation of effective radius and underestimation of optical depth. An example of one of these errors is a 3-D effect

known as *shadowing*. As the term implies, shadowing can occur when an obstacle (i.e. a higher cloud) is in the way of the incoming sunlight, and therefore darkens the lower cloud adjacent to it. This adjacent obstacle would then lower the reflection function across all wavelengths for the cloud under consideration. Complementary to shadowing, there is also the 3-D effect known as *illumination*, wherein a pixel on the aforementioned obstacle appears brighter. Looking back at Figure 1.1, one can see that lowering the reflection function for both channels results in a lower optical depth and a higher effective radius (the intersection point moves to the lower left), and increasing the reflection functions results in a higher optical depth and lower effective radius (the intersection point moves to the upper right). It should be noted these are simplified 3-D effects, since in a 3-D environment the reflectance of a pixel is dependent on *all* other pixels in the path of radiation (*Varnai and Marshak, 2003*).

Effects such as these 3-D complications in an assumed 1-D scene should be taken seriously, as they obviously could skew important data products, such as effective radius or optical depth, which in turn may distort important studies that they are based upon. If the effect of the heterogeneity of the clouds plays role in the degree to which an overestimation or underestimation of such products takes place, then it would be beneficial to be able to quantitatively represent these heterogeneous clouds based on their spatial complexity. If they can be quantitatively classified, then it would be possible to operationally identify them and apply corrections as needed.

In a study done by *Liang et. al. (2009)*, a variable known as the spatial heterogeneity metric, or H_σ, was explored, and it was defined as follows:

$$H_\sigma = \frac{\sigma}{\bar{R}} \ , \qquad \text{Eq. 3}$$

where $\bar{R}$ is the mean 0.866 μm BRF of the 12 x 12 275 m pixels centered on the considered 1 km pixel, and σ is its standard deviation. Low values of H_σ indicate a more spatially homogeneous pixel, and higher values represent a more spatially heterogeneous pixel. In *Di Girolamo et. al (2010)*, global distributions of H_σ were analyzed for 2001 to 2008 for the months of January and July. They showed that the marine stratocumulus regions (such as the west coast of the Americas) show strong homogeneity, especially in July, and the high latitudes in the summer hemisphere also show strong homogeneity. These conform to observations of stratiform clouds under high sun conditions.

Several field campaigns have been used for validation studies of satellite derived r_e and τ for warm marine clouds, such as APEX, ASTEX, COSAT, FIRE, SOCEX II, VOCALS, and WENPEX (*Nakajima et al., 2005*; *Platnick and Valero, 1995*; *Wetzel et. al., 2001*; *Nakajima et al., 1991*; *Szczodrak et al., 2001*; *Painemal and Zuidema, 2011*; *Kuji et al., 2000*). However, these have been done in regions of typical marine stratiform clouds and under high-sun scenarios, both of which are favorable for homogeneous plane-parallel conditions (*Di Girolamo et al., 2010*). But what about heterogeneous and non plane-parallel conditions, such as those for cumulus clouds? This analysis explores this realm, using the "Rain In Shallow Cumulus over the Ocean" campaign, or simply *RICO*, as validation of MODIS r_e retrievals for trade wind cumulus clouds. Using aircraft data from RICO, a general vertical profile of the trade wind cumuli will be explored. This data will then be compared to MODIS r_e retrievals, and heterogeneity of the retrieved MODIS pixels will also be analyzed in order to assess potential 3-D effects and validity of the claims of a systematic bias in retrievals.

1.3 Figures

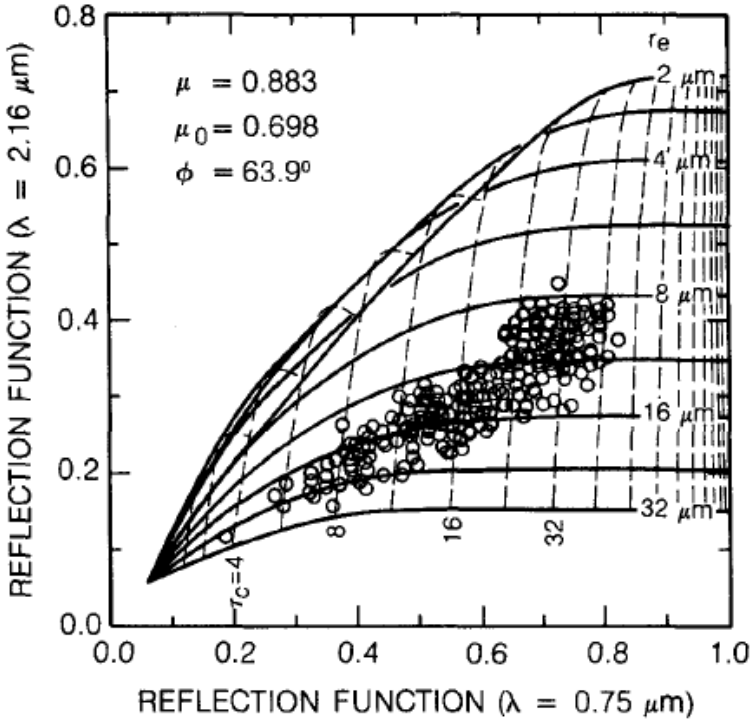

Figure 1.1 – Relationship between reflection function at 0.75 µm and 2.16 µm at the listed sun/view geometry (Figure taken from *Nakajima and King (1990)*)

CHAPTER 2

RICO DATA OVERVIEW AND METHODOLOGY

2.1 Overview

The RICO field campaign took place in the Caribbean off of the coasts of Antigua and Barbuda between November 2004 and January 2005, and aimed to explore how rain affects the structure and statistics of trade wind cumuli (*Rauber et al., 2007*). The domain used in this area for the field campaign was based around the range of the NCAR SPolKa radar. Within this domain, three aircraft were used for the experiment: the NSF/NCAR Hercules C-130Q, the FAAM BAE 146-301, and the University of Wyoming King Air 200T. In addition to the three aircraft, the Research Vessel *Seward Johnson* was also taking measurements to the north-east of the island of Barbuda during the month of January. Three surface stations, one on Antigua and two in Puerto Rico, focused on aerosol measurements during the experiment. All of this was also supported by various rawindsonde sites.

The analysis within this dissertation will focus on the NSF/NCAR C-130Q Hercules aircraft (hereafter referred to as the C-130), and the instruments aboard that provide the microphysical measurements of the cumuli as they are flown through.

2.2 NSF/NCAR C-130Q Hercules

The C-130 performed 19 research flights between December 7, 2004 and January 24, 2005. The dates and times of each flight are shown in Table 1. Specifically, two instruments aboard this aircraft are assessed—the FSSP-100 and the OAP 2D-C probes.

2.2.1 FSSP-100

The PMS Forward Scattering Spectroradiometer Probe (FSSP-100) is a cloud probe created by Particle Measuring Systems, Inc. The FSSP-100 (hereafter referred to as just the *FSSP*) detects a particle by measuring the intensity of light scattered by the particle as it passes through a Helium – Neon laser. The particle scatters this light in all directions, but the light scattered forward travels through a prism that focuses the light through condensing lenses and into a beam splitter. The beam splitter splits the scattered light onto two photodetectors, which define the instrument's sample volume. Using Mie Theory and assuming that the light scattered passes through liquid, spherical droplets with a refractive index of 1.33, the particle size can be sized accordingly (*Pinnick et al.,1981*; *Dye and Baumgardner, 1984*). This probe was chosen as the basis for this analysis due to its flexible data rate, as it is given as either low rate 1 hz data or high rate 10 hz data. FSSP effective radius is reported at the low rate resolution, but due to some inconsistences that were noted with the low rate data, specifically that the raw counts of the low rate data were not the correct summation of the high rate counts, it was decided that this study will focus on using the high rate 10 hz data. For the C-130 flights, the FSSP has a usable size diameter range of 2.35 – 45.75 µm with 1.55 µm diameter size bins, which is large enough to encompass the size spectrum of typical cloud droplets. Figure 2.1 shows a schematic of the instrument positions aboard the C-130 for the RICO campaign, and the FSSP is located at position *LPC*.

2.2.2 OAP 2D-C

The PMS OAP 2D-C probe, located at position *LWO* in Figure 2.1, records two-dimensional shadows of drops as they pass through a Helium-Neon laser, and its shadow is cast onto a linear diode array, which is later interpreted into information about size and shape (*Heymsfield and Parrish, 1978*). The data available on this probe for the RICO flights is given with at a 1 hz rate, and it is reported as two different datasets—the *reconstruction* dataset and the *260X emulation* dataset. The 2D-C reconstruction dataset uses the height and width detected to determine the particle size, and has a usable size diameter range of 62.5 – 1587.5 μm with 25 μm diameter size bins. The 2D-C 260X emulation dataset uses only the height detected in order to determine particle size, and, as the name implies, is intended to simulate distributions detected by the OAP 260X probe, a one-dimensional probe located at position *RWI* in Figure 2.1. The 2D-C 260X emulation dataset has a usable size diameter range of 62.5 – 787.5 μm with 25 μm size bins.

2.3 Vertical Profile Analysis

In order to get a general idea of the cloud droplet structure of trade cumuli in the RICO region, the FSSP data is first assessed. This data is given in the form of a designated high rate netCDF file, which has several different variables measured from various instruments aboard the aircraft. Out of the 19 Research Flights (hereafter abbreviated to *RF*), it was decided not to include RF01, RF02, and RF19, due to potential difficulties and irregularities with the FSSP data during these flights. RF17 is also excluded from this analysis, as it was a flight dedicated to

passing through rain shafts (*Snodgrass et al., 2008*). Data from RF17 is still included in Appendix A for reference. From these flights, 10 hz data from the FSSP droplet size distribution, liquid water content (LWC), and number concentration (N) are extracted. For these same data points, geolocation data is also acquired; this, however, is given at a higher data rate of 25 hz, so it must be scaled down to 10 hz, in order to match the data points. Once this basic data is extracted, the data is filtered to only contain data points that have a number concentration of $N \geq 10$ cm^{-3}, which we have defined as "cloudy". These points are also assigned a same "cloud number" if they are consecutive, the idea being that these consecutive points are part of the same cloud being observed. Next, one second of data from each side of the clouds (which ends up being slightly more than about 100 m from each side) is removed; this is intended to remove the influence of entrainment from the data. Now, in order to get a better representation of the mean of this data, we average the remaining consecutive points into 1 hz data points; areas without a complete consecutive 1 second of data (i.e. blocks of less than 10 of the consecutive 10 hz data points) are removed. The only variable that was not averaged across a whole second of data is the droplet size distribution—instead, the distribution was added together, and then the effective radius was calculated from this 1 second distribution. Since the effective radius itself is a form of a mean, it was decided that this method would be more properly representative of it than averaging the distributions and then calculating r_e from them. From this final dataset, vertical profiles of the cloud droplet effective radius and liquid water content are constructed, using 100 m altitude bins, 0.5 μm effective radius bins, and 0.05 g/m^3 LWC bins. Various studies (*Arabas et al., 2009*; *Colón-Robles et al., 2006*) served as inspiration for the methods used here, though several parameters have been tailored to fit the needs of this analysis. The results of this are shown in chapter 3.

2.3.1 Particle Shattering

It has been suggested that a potential complication with datasets from the FSSP-100 is the possibility of particle shattering, where very large drops strike the side of the probe and shatter into numerous smaller droplets in the measuring range of the FSSP, thereby potentially distorting the size distribution measured (*Baker et al., 2008*). We attempt to counteract this possibility by analyzing the 2D-C probe for this dataset as well, since the 2D-C measures much larger particles and is located relatively close to the FSSP on the aircraft. In this version of the analysis, the same steps are carried out as in the regular vertical profile analysis in section 2.3, but an extra step is added after defining the cloudy points and cloud numbers. Data points are rejected that have 2D-C total concentrations greater than either 10/L or, more conservatively, 0/L. The results are shown in section 3.3. It should be noted that the reconstruction and the emulation versions of the 2D-C data showed nearly identical results, so for consistency and simplicity's sake, any analysis done in this study using the 2D-C data is using the emulation version. The actual 260X instrument is located on the other side of the aircraft, so the closer proximity 2D-C will make for a better choice.

2.3.2 FSSP-100 + 2D-C Interpolation

For reasons that will be described later in section 5.2, another dataset was made that effectively combined the full range of the FSSP distribution and part of the 2D-C distribution to create a size distribution that covers a slightly higher range that the normal FSSP range. Using the full FSSP concentration distribution, interpolation between the last bin of the FSSP

concentration distribution and the first bin of the 2D-C concentration distribution was done, creating four new, equal-sized bins in between. This interpolated distribution covers a *radius* range of 1.175 – 43.25 um. After the 1 second averaging process, like before, the distributions are added together instead of averaged, and then the effective radius is calculated from the interpolated distribution. The results of this are shown in section 5.2.

2.4 Figures and Tables

RAF Flight #	Date	Start Time (UTC)	End Time (UTC)
FF02	12/4/2004	13:57:00	19:04:00
RF01	12/7/2004	16:09:56	21:51:15
RF02	12/8/2004	14:15:00	16:24:00
RF03	12/9/2004	14:01:00	22:19:30
RF04	12/10/2004	14:04:00	22:31:50
RF05	12/13/2004	14:47:00	22:13:40
RF06	12/16/2004	13:55:00	22:08:00
RF07	12/17/2004	13:49:00	22:22:15
RF08	12/19/2004	11:10:00	19:54:00
RF09	12/20/2004	10:56:00	19:05:40
RF10	1/5/2005	14:44:00	23:18:25
RF11	1/7/2005	13:55:00	22:21:00
RF12	1/11/2005	13:58:00	22:31:30
RF13	1/12/2005	14:17:00	22:46:30
RF14	1/14/2005	14:57:00	23:25:55
RF15	1/16/2005	14:12:10	22:27:00
RF16	1/18/2005	11:28:44	19:11:57
RF17	1/19/2005	11:47:00	20:19:00
RF18	1/23/2005	10:00:00	18:31:00
RF19	1/24/2005	10:00:00	17:42:00
FF05	1/26/2005	14:31:00	22:07:00

Table 2.1 – Date and time for each C-130 research flight.

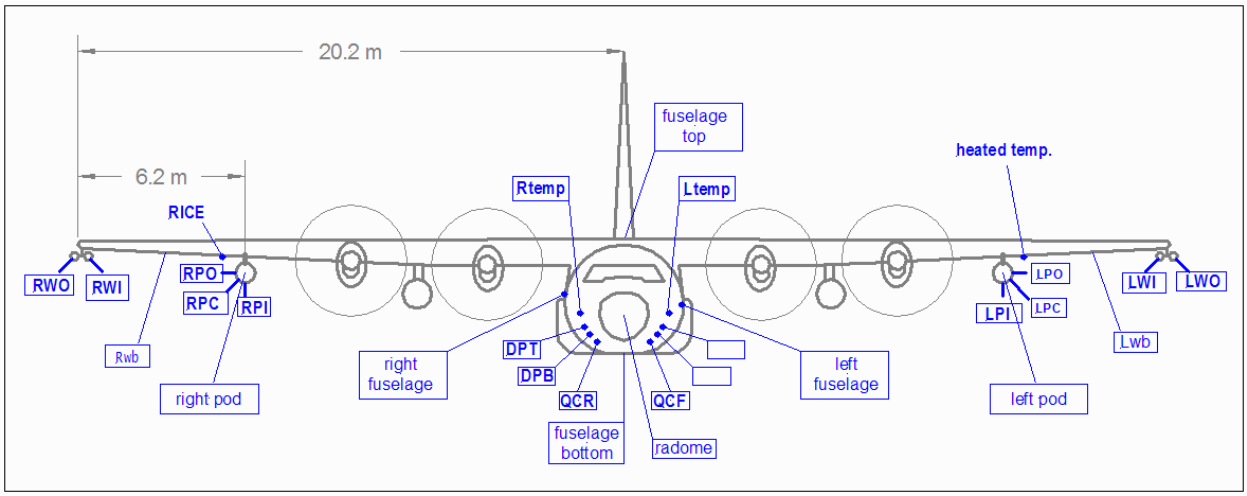

Figure 2.1 – Location codes for the various instruments aboard the C-130 during RICO (image taken from *http://www.eol.ucar.edu/raf/Projects/RICO*).

CHAPTER 3

AIRCRAFT RESULTS

3.1 FSSP-derived r_e Profile

As described in section 2.3, the aircraft data was binned according to effective radius and altitude, and then constructed into a mean vertical profile of the cumulus clouds observed. The FSSP-derived effective radius profile for all of the considered flights is shown in Figure 3.1, and the profiles for each flight individually are listed in Appendix A. The color bar represents the frequency of occurrence of the data points over the whole period under consideration. The figure suggests that there is a general increase in r_e in these clouds with increasing altitude, but after reaching around the 2 km altitude mark, the profile begins to slightly decrease with increasing altitude up to our altitude of consideration (the approximate altitude of the freezing level), below which the vast majority of trade wind cumuli exist (*Zhao and Di Girolamo, 2007*). Admittedly, there is significant reduction in the amount of data at these altitudes, but nevertheless this is the pattern observed. A noteworthy feature here is the high concentration of about 13 μm droplets points around 2 km altitude, which is at about the altitude when the trend of the sizes begins to decrease with height. Another feature to note are the few 11 μm droplets located at very low altitudes. Since this is below cloud base, these are likely shattering events caused by flying through a small rainshaft.

The total profile seen here is similar to the Fast-FSSP r_e profiles constructed by *Arabas et al., 2009*. In that study, only RF06, RF07, RF09, and RF12 were considered, so results shown in this study encompass more flights (individual flight profiles may be viewed in Appendix A). It

should also be noted that *Arabas et al.,2009* used different thresholding values and used the data at the full 10 hz, whereas this study used the 10 hz data but averaged it into 1 hz data. They also used a 10/L 2D-C concentration threshold for their entire analysis. Our study also shows similar results to the LES study done in *Zhang et al., 2010*. In that study, three different r_e profiles of shallow convective clouds were assessed based on different aerosol mixing ratios, leading to a *polluted, intermediate,* and *clean* case. The intermediate-pollution case is the most similar to this study's total r_e profile. The evolution of the cloud behaves remarkably similar, where near cloud has low r_e values that increase with altitude, and begin to decrease around the 2 km mark. However, their results do not extend far beyond that point.

3.2 FSSP LWC

The FSSP liquid water content was also binned according to size and altitude to construct a mean vertical profile of the LWC of a cumulus cloud. The FSSP-derived LWC for all considered flights is shown in Figure 3.2, and the individual flights are listed in Appendix A. Again, the color bar represents the frequency of occurrence of the data points over the considered period. Although not as clear-cut as the r_e profile, what is seen here is a similar pattern—a general increase in LWC with increasing altitude up to a certain level, and then a general decrease in LWC with increasing height, although with far less samples at these altitudes. The first thing to note should be the very low LWC points at around 100 m altitude. Again, since this is below cloud base, this is most likely particle shattering from the C-130 flying through a rainshaft. The concentration of low LWC points at 2 km, which is the same altitude as the cluster of 13 μm droplets shown in Figure 3.1, could potentially be an in-cloud shattering event. There is

also a cluster of about 0.01 g/m^3 LWC around 800 m altitude. The next section will utilize the 2D-C probe to assess whether or not there actually are any measurable shattering events in the dataset.

3.3 2D-C Filtering

As explained in section 2.3.1, the FSSP is known to have some issues with particle shattering, potentially skewing the distributions observed and therefore distorting the statistics in our analysis. We use the 2D-C total concentration thresholds of 10/L and 0/L in order to see the effect of possible particle shattering upon the constructed vertical profiles of r_e and LWC. The new r_e profiles are shown in Figure 3.3 and the new LWC profiles are shown in Figure 3.4, where the thresholds are (a) 10/L and (b) 0/L for both figures. Going from no threshold to the 10/L threshold, it is immediately noticeable that the 2 km event in both the r_e and LWC profiles is no longer the center of focus. However, the 100 m altitude events, which are being stamped as particle shattering events, are still prevalent. Tightening the threshold down to 0/L, the 100 m events disappear completely. This suggests that in order to truly remove particle shattering events (at least based on this study's approach), any data points that coincided with a 2D-C total concentration greater than 0/L must be removed. Looking at the 0/L threshold profiles, it can be noted that the majority of the valid cloud droplets lie between 600 and 900 m, and the general increasing trend seen in the non-filtered profiles is still present, but too many points above around 1.5 km have been removed to be able to establish any kind of meaningful pattern those altitudes.

3.4 Figures

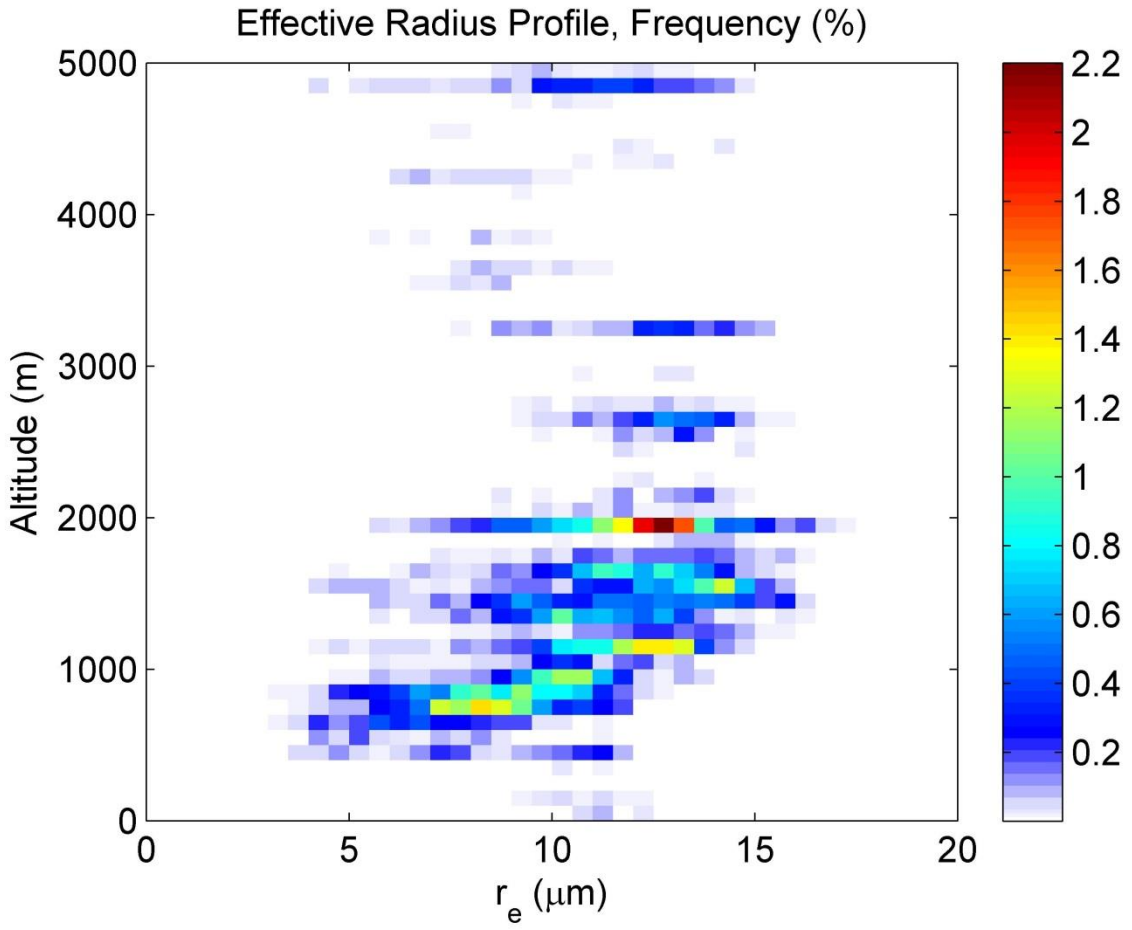

Figure 3.1 – FSSP effective radius profile using all data from considered flights, where the x-axis is r_e in μm, the y-axis is the altitude in meters, and the colors represent the frequency in percent.

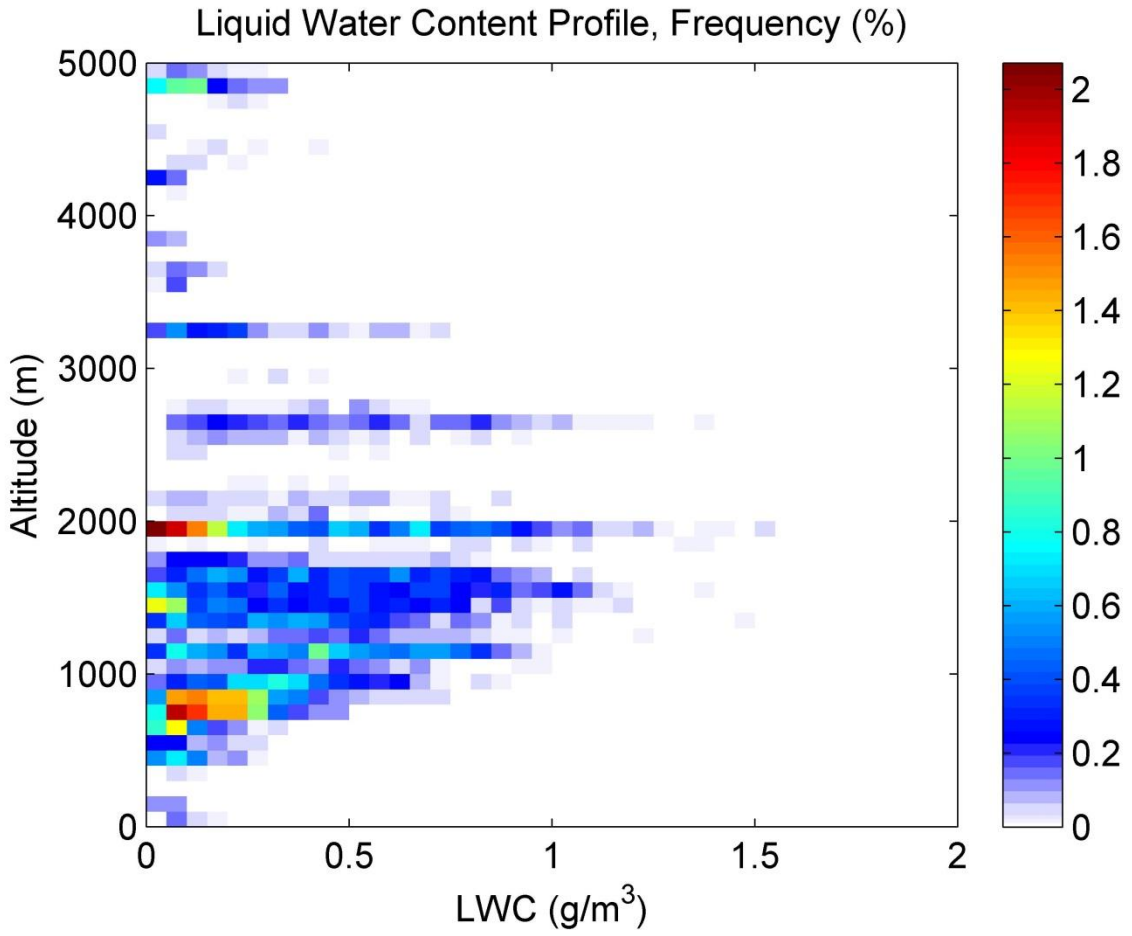

Figure 3.2 – FSSP LWC profile using all data from considered flights, where the x-axis is LWC in g/m^3, the y-axis is the altitude in meters, and the colors represent the frequency in percent.

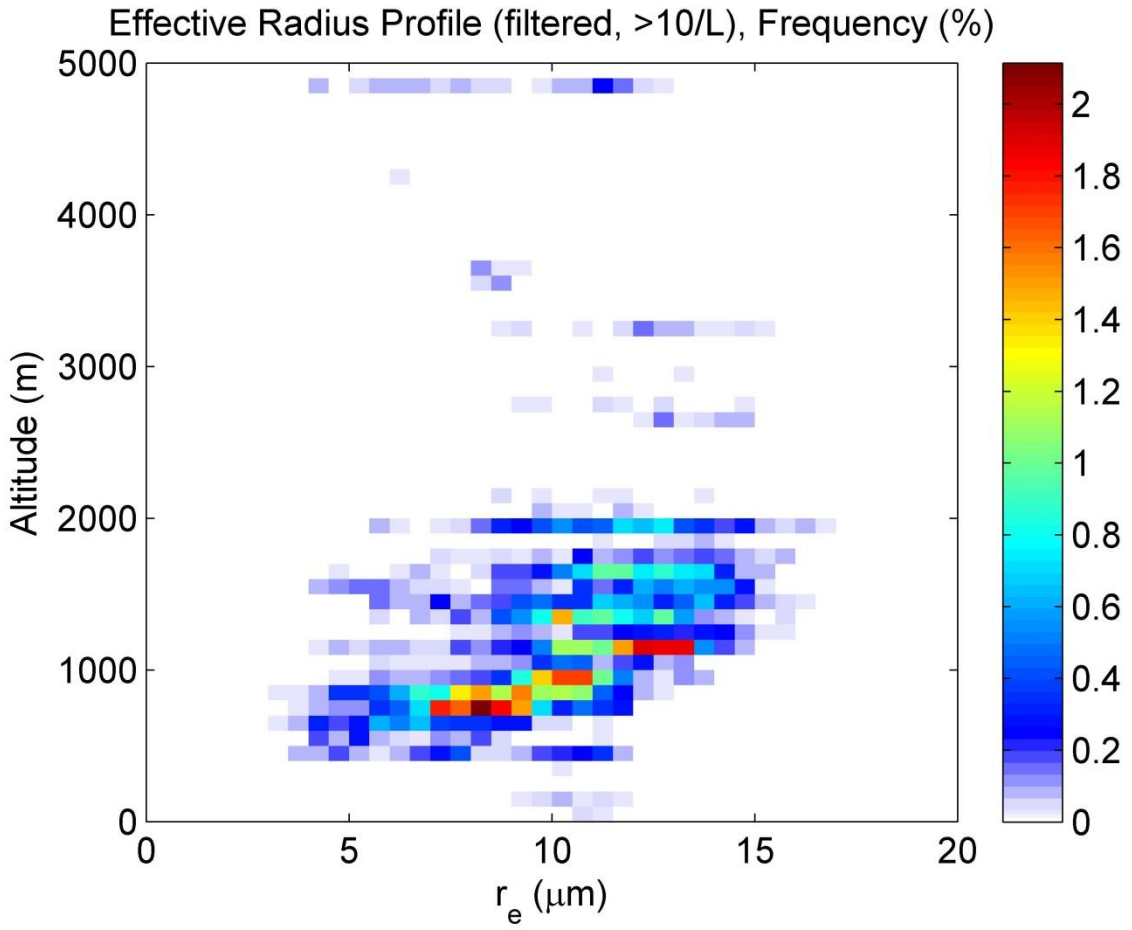

Figure 3.3(a) – FSSP effective radius profile for RF03-RF18 using 2D-C 10/L concentration threshold, where the x-axis is r_e in µm, the y-axis is the altitude in meters, and the colors represent the frequency in percent.

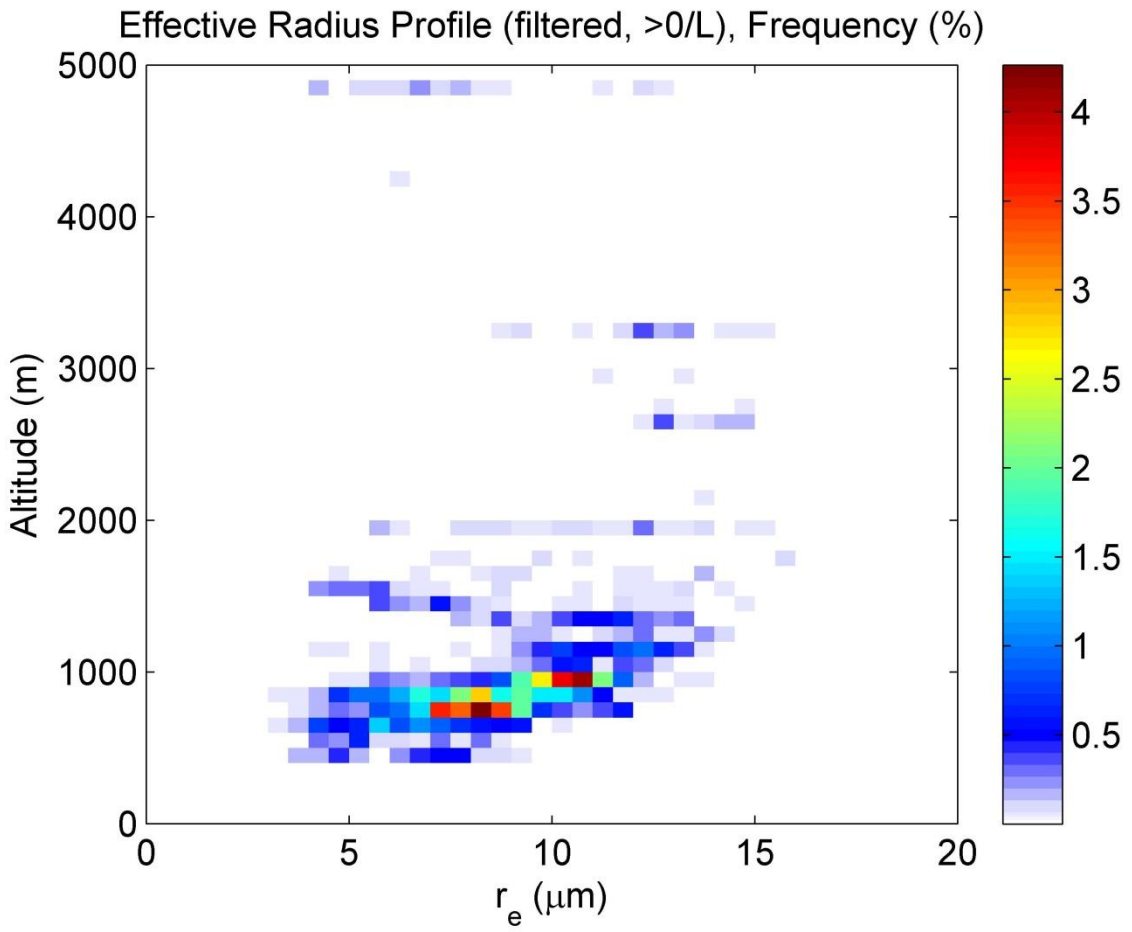

Figure 3.3(b) – FSSP effective radius profile for RF03-RF18 using 2D-C 0/L concentration threshold, where the x-axis is r_e in µm, the y-axis is the altitude in meters, and the colors represent the frequency in percent.

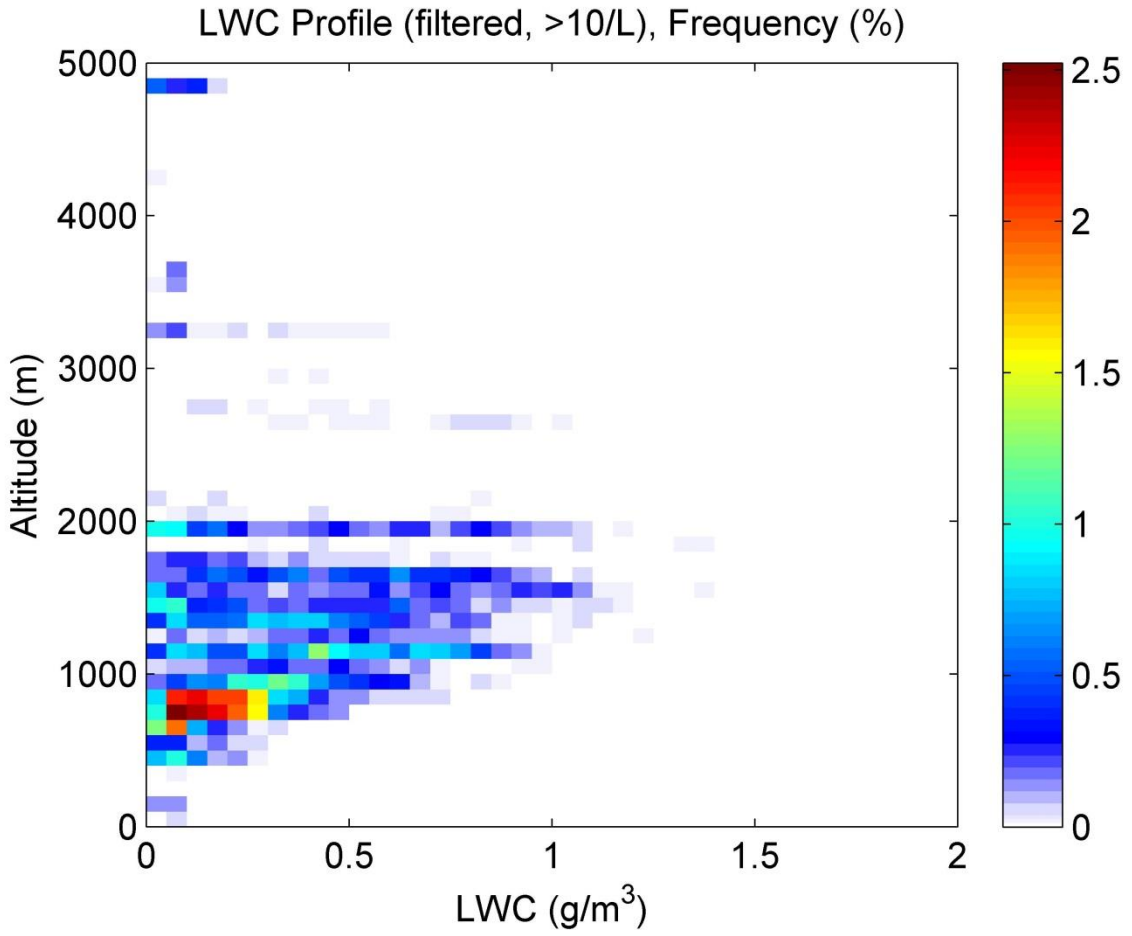

Figure 3.4(a) – FSSP LWC profile for RF03-RF18 using 2D-C 10/L concentration threshold, where the x-axis is LWC in g/m^3, the y-axis is the altitude in meters, and the colors represent the frequency in percent.

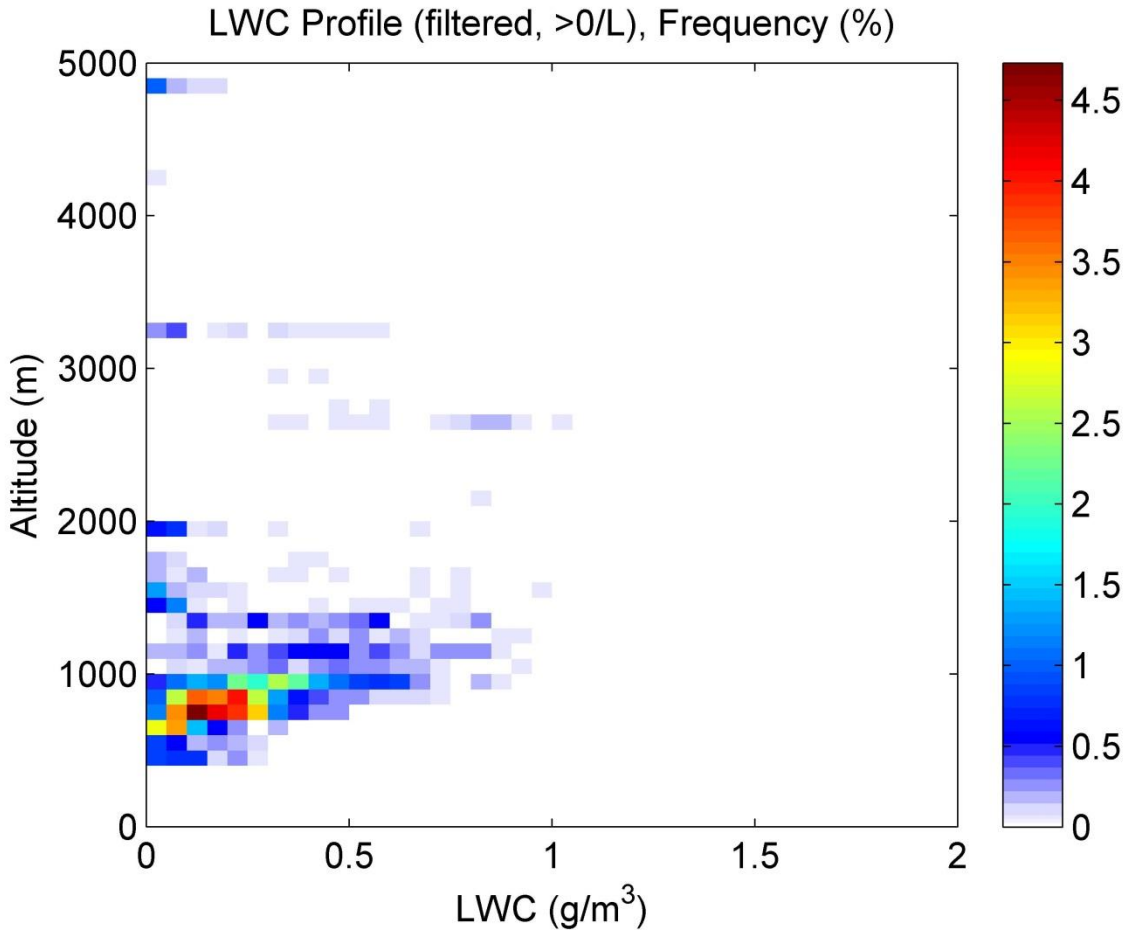

Figure 3.4(b) – FSSP LWC profile for RF03-RF18 using 2D-C 0/L concentration threshold, where the x-axis is LWC in g/m^3, the y-axis is the altitude in meters, and the colors represent the frequency in percent.

CHAPTER 4

MODIS OVERVIEW AND METHODOLOGY

4.1 Overview

MODIS, the "Moderate Resolution Imaging Spectroradiometer", is an instrument that is aboard two separate low-Earth orbiting platforms, the EOS-Terra and EOS-Aqua platforms. It has a 2330 km swath, 36 spectral channels between 0.4 μm and 14.4 μm. Depending on the channel, it reports at 250 m, 500 m, or 1km resolutions at a nadir view angle.

This study utilizes the datasets provided by MODIS and compares them with the in-situ C-130 aircraft data. In particular, this study uses the cloud effective radius retrievals from the Level 2 data given by MODIS and compares it with the effective radius distribution of the FSSP. The 2D-C is also used in tandem with the FSSP at some points in the analysis, but it is used more as a supplement for the FSSP.

4.2 MODIS and Aircraft comparison Methodology

In order to compare the cloud drop effective radius retrievals from MODIS with those of the aircraft data, eight different MODIS products from Collection 5.1 will be utilized, where four are from the instrument aboard the Terra platform (designated by "MOD" at the front of the product name), and the other four are from the instrument aboard the Aqua platform (designated by "MYD"). The MOD06/MYD06 products, referred to as the cloud product, report the cloud drop effective radius at 1 km resolution, and as derived by three different spectral channels,

where the 2.1 μm spectral channel is the default given product. The 1.6 μm and the 3.7 μm channel are reported as separate variable in the cloud product. The effective radius from the 1.6, 2.1, and 3.7 μm bands will hereafter be denoted as $r_e(1.6)$, $r_e(2.1)$, and $r_e(3.7)$, respectively. The cloud product also provides quality assurance, of which a portion is imported from the MOD35/MYD35 product, also referred to as the *cloud mask*. This is where various "flags" for the data are stored, such as confidence, phase, and sunglint. The cloud product gives, geolocation as well, but it is aggregated up to 5 km resolution. However, the MOD03/MYD03 products give geolocation data at 1 km resolution. This matches the resolution of the cloud retrieval pixels, so this will be this analysis' source for geolocation. The MODL1B/MYDL1B provides radiance products at 250 m, 500 m, and 1 km resolution. This will primarily be used later for spatial heterogeneity tests.

4.2.1 FSSP-100 vs MODIS r_e(2.1 μm)

To prepare the MODIS retrievals for comparison with the aircraft data, geolocation from the aircraft data was utilized to grid the frequency of occurrence of the 1 second (100 m) aircraft data points over the span between RF03 and RF18 (excluding RF17) into 1° x 1° regions, as shown in Figure 4.1.

The MODIS 1 km retrievals were used if they met the following criteria: 1) the retrievals must be successful; 2) the retrieval must fall within the bounds of the non-zero frequency regions shown in Figure 4.1 on the same day that aircraft data was collected in the region; 3) the retrieval was designated as a liquid phase cloud as reported in the cloud mask; 4) the retrieval was

designated as “confident cloudy” by the cloud mask; 5) the QA had indicated that there was no sunglint.

The FSSP data and the MODIS effective radius retrievals were each separately binned into 0.5 μm bins. The results are shown and discussed in Section 5.1.

4.2.2 Aircraft 100 m and 1 km transects vs MODIS r_e(2.1 μm)

In the same manner as done in section 2.3, another dataset was made by averaging over 10 seconds, instead of 1, to represent a larger transect length of the data points (about 1 km), the idea here being that in a cumulus environment, a larger horizontal transect would also indicate a larger cloud vertically. It is then binned in the same manner as the 100 m data points, and the results are shown and discussed in Section 5.1.

4.2.3 FSSP 100m, MODIS r_e(2.1 μm), r_e(1.6 μm), r_e(3.7 μm) Comparison

As noted before, the MODIS Collection 5.1 MOD06/MYD06 product offers cloud drop effective radius retrievals using either the 1.6, 2.1, or 3.7 μm spectral bands. The default effective radius product uses the 2.1 μm band, while another variable, the cloud effective radius difference, reports both the difference between the 1.6 and 2.1 μm bands and the difference between the 3.7 and 2.1 μm bands. This implies that a successful 1.6 or 3.7 μm retrieval in this product is dependent on whether or not the 2.1 μm retrieval was successful as well, therefore limiting our 1.6 and 3.7 μm retrievals to less samples than the 2.1 μm band.

A comparison between these three channels and the FSSP are shown and discussed in Section 5.4.

4.2.4 H_σ vs r_e

The spatial heterogeneity, H_σ (eq. 3, Chapter 1), of each of the retrieved 1 km pixels will be examined and compared with its corresponding r_e value. As the H_σ defined in *Liang et al. (2009)* was based upon the MISR instrument, our analysis will instead need to be based on MODIS, where we use the 12 x 12 250 m pixel domain surrounding the considered 1 km pixel and using the reflectance of the 0.865 μm band. Section 5.5 shows the results of spatial heterogeneity analysis against the r_e retrievals.

4.2.5 Smooth Cloud Examination

In order to simulate what would be considered a smooth cloud, it would have to have a very low H_σ value for the pixel. An analysis is done to view how the statistics of the distribution of the $r_e(2.1\ \mu m)$ from Terra would change if we were to limit our sample to only those below a certain threshold value for H_σ. In *Di Girolamo et al. (2010)*, it was suggested that a plane-parallel cloud would have to have an H_σ less than either 0.112, 0.088, or 0.076, depending on the criteria for angular consistency. Using the 0.088 or 0.076 threshold for H_σ yields too little data from our setting for proper analytical use, so only the 0.112 threshold will be used. The results of this are shown in section 5.7. Note that *Di Girolamo et al. (2010)* based these numbers off of a MISR and MODIS analysis aboard Terra, so only Terra will be assessed for spatial heterogeneity.

This threshold limitation is also applied to the cloud optical depth retrievals for the same pixels. The results are shown in section 5.6.

4.3 Figures

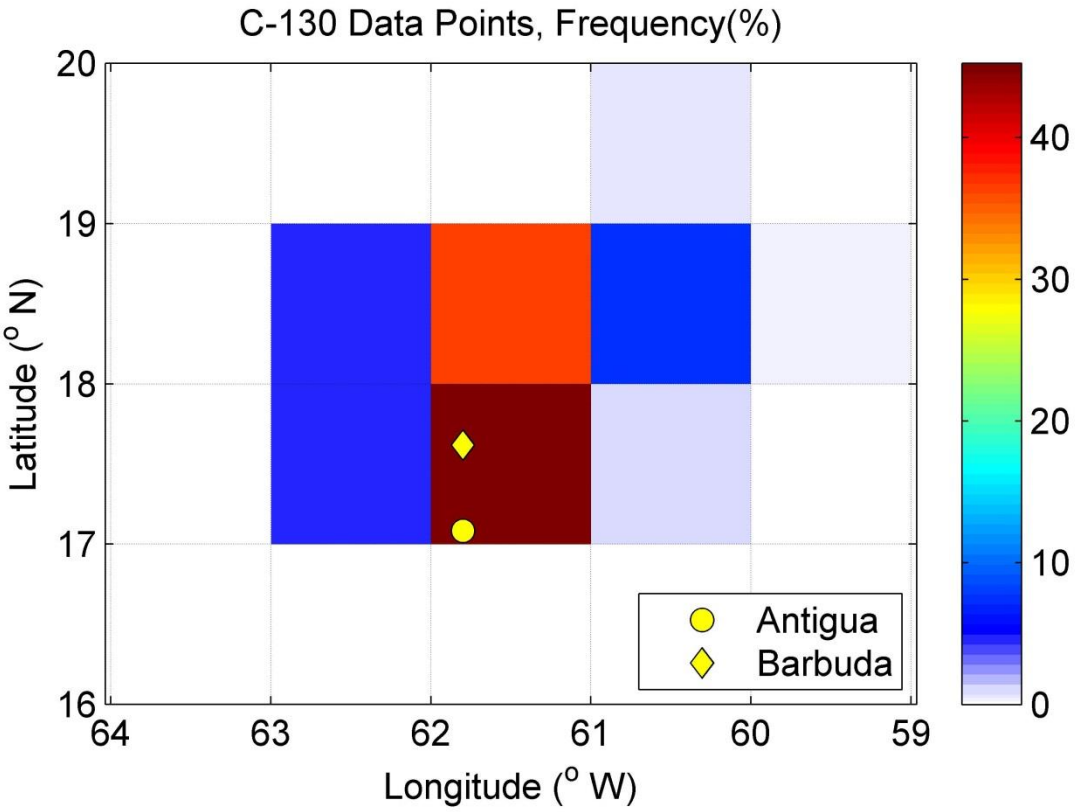

Figure 4.1 – 1°x1° regions and the frequency of occurrence of the 1 second aircraft data points.

CHAPTER 5

MODIS RESULTS

5.1 FSSP vs r_e(2.1 µm)

The comparison illustrated in Figure 5.1 shows the r_e redistribution of the 100 m FSSP, $r_e(2.1)$ from Terra, and $r_e(2.1)$ from Aqua. As can be seen, there is a large disparity between the FSSP distribution and both MODIS platforms. The mean r_e of the binned FSSP, Terra, and Aqua sets are 10.8 µm, 23.6 µm, and 20.7 µm, respectively—both MODIS mean effective radii are about a factor of 2 larger than that of the in-situ FSSP. It is also noted that the spread of the MODIS r_e is far larger than that of the FSSP, and the MODIS data appears to cut off at 30 µm—this is because the MODIS algorithm sets any r_e liquid phase cloud retrieval beyond 30 µm as a fill value (*Platnick et al., 2003*).

Figure 5.2 shows the same datasets as those listed above, but with the addition of the FSSP datasets that filtered any data that had 2D-C total concentration greater than either 10/L or 0/L. Restricting the FSSP data in this manner reduces the r_e means to 10.2 µm for the 10/L restriction and 8.8 µm for the conservative 0/L restriction. This creates a slightly larger disparity between the in-situ and MODIS datasets.

It is possible to make an argument that the FSSP data is representing transects that are too small for viable comparison against MODIS pixels (100 m would be sub-pixel to the 1 km MODIS pixels), and therefore should not be compared to such MODIS data. This possibility is explored by creating another FSSP aircraft dataset that is averaged over 10 seconds (~1000 m) instead of the 1 second (~100 m), in order to represent larger clouds. This is shown in Figure

5.3. While using 1 km aircraft pixels does increase the mean r_e, it only increases it by 0.8 µm—still not anywhere near the high mean values of MODIS on either platform. This method was also used for exploring even longer transects as well, including 2km, 3km and 5km, but there was such a drastic reduction in data points that it was decided to not include them in the analysis, but it can be said that the mean values hardly increase at all for these longer transects.

5.2 FSSP + 2D-C Interpolation vs r_e(2.1 um)

It was considered that the size range detectable by the FSSP-100 is too small to be effectively compared to the MODIS r_e retrievals. As explained in section 2.3.2, an interpolated distribution that combined the FSSP and the beginning of the 2D-C was created in order to explore the possibility of this. Figure 5.4 shows the results of this, keeping the other distributions present as a comparison. The maximum of the distribution is increased and even covers some r_e larger than that of MODIS, but the shape of the aircraft distribution has barely changed, and the interpolated mean is only about 0.8 µm larger than that of the regular FSSP distribution. Because this interpolated distribution was not much different from the regular FSSP distribution, the regular FSSP distribution will be used for the rest of the analysis.

5.3 Viewing Geometry

The apparent extreme overestimation of r_e by the MODIS instrument for trade wind cumuli could be an artifact of viewing geometry, where the retrieved pixels at scan edges show

larger r_e than those at nadir (*Maddux et al., 2010*). Figure 5.5 shows the frequency of the retrievals, grouped into 10° bins of sensor zenith angle.

Pixels from Terra show sensor zenith angles that are weighted heavily towards the edge of the scans, and there are hardly any pixels with SZA less than 20° in magnitude. The bulk of the SZA distribution for Aqua is similar to Terra, but there are less of the extreme SZAs at scan edge and more towards nadir. Comparing this to the r_e distributions shown in Figure 5.1, it can be noted that the differences between Terra and Aqua in these figures could be related. Terra has more pixels with extreme SZAs and more pixels with high r_e, while Aqua has more pixels near nadir and more low r_e pixels. *Maddux et al., 2010* demonstrated with long-term composites of Level 3 MODIS data that near scan edge r_e values could be up to 7 µm larger than near-nadir r_e, in particular in regions of trade wind cumuli. While it is likely that the viewing angle here may have some contribution to the large MODIS r_e retrievals, chances are that it is just a component of the reason for this overestimation. To explore other potential culprits, the r_e retrievals using alternate absorbing spectral bands will be assessed.

5.4 FSSP vs r_e(1.6 µm), r_e(2.1 µm), r_e(3.7 µm)

The three different infrared bands used for cloud drop effective radius retrievals, the 1.6, 2.1, and 3.7 µm bands, are chosen because they are all very absorptive of water vapor, but have different degrees of said absorption. The 1.6 µm band is the least absorptive, then the 2.1 µm, and the 3.7 µm band is the most absorptive. These should in theory be very useful for r_e retrievals, since theoretically in a plane-parallel cloud the r_e should increase with increasing height (*Platnick (2000)*). Since the 3.7 µm band is the most absorptive of the three, the r_e

detected by this band should be higher in the cloud, then the 2.1 μm band, and then the 1.6, being the least absorptive, should be observing a level lower in the cloud. Figure 5.6 shows the results of the retrievals for the FSSP vs the three retrieval bands, where the MODIS platforms are (a) Terra, and (b) Aqua.

From Figure 5.6(a), it can be noted that the 1.6 μm band shows a slightly bimodal feature in the distribution, and its mean r_e is 22.7 μm, just slightly less than the 2.1 μm band's 23.6 μm mean. However, the distribution that stands out is the 3.7 μm band, which shows a distribution shaped fairly similar to the FSSP's, and has a mean that is far closer to the FSSP as well, being at 14.1 μm. The same can be said about Figure 5.6 (b), where the 1.6 μm band has a mean of 18.2 μm, which is slightly smaller than Aqua's 2.1 μm band, but the 3.7 μm band is again much closer to the FSSP, with a mean r_e of 15.0.

This behavior of the 3.7 μm band has been seen before in other studies, and it is usually attributed to either drizzle, or cloud heterogeneity (*Seethala & Horváth, 2010*; *Nakajima et al., 2010; Zhang & Platnick, 2011*). In recent studies, drizzle has been shown to not demonstrate a strong sensitivity to MODIS r_e retrievals (*Zinner et al., 2010*; *Zhang et al., 2012*), so the next section will assess the possibility of cloud heterogeneity being responsible for this behavior.

5.5 H_σ vs r_e

It has been suggested that large r_e (often accompanied by small τ) can be an indication of a mixture of sub-pixel cloudiness and clear sky, where the sub-pixel clear regions decrease the reflectance of the whole pixel (*Platnick et al., 2003*; *Marshak et al., 2006*). However, it should be pointed out that even fully cloudy pixels can be heterogeneous. The effect of this cloud pixel

heterogeneity on the retrieved r_e is assessed by calculating the H_σ of each retrieved pixel. Density plots are created and the pixels are binned into 1 μm r_e bins and 0.1 H_σ bins. The results are shown in Figures 5.7(a-c), corresponding to the 1.6, 2.1 and 3.7 μm bands of Terra, respectively. The color bar represents the frequency of occurrence. Figure 5.7(a) seems to be generally clustered into three different areas of the figure, identifiable as the two peaks and high r_e end in Figure 5.6(a). Most of the pixels in this plot have r_e > 16 μm, and most H_σ values are between 0.1 and 0.8. There is not much of a noticeable trend of the data for the 1.6 μm band. Figure 5.7(b) shows a clearer trend, where there is a reduction in lower-r_e pixels as H_σ increases. Most of the pixels in this band have H_σ between 0.5 and 0.7, and these highly clustered pixels typically have r_e > 20. Clear sky contamination or cloud heterogeneity could likely be the cause of these high r_e pixels in the 2.1 μm band, as the lower reflectance of the pixel due to "holes" in clouds or clear sky increases the r_e (*Platnick et al., 2003*).

Figure 5.7(c) shows a different trend from the 2.1 μm band, where here the r_e generally decreases as H_σ increases. Another way to view this difference is shown in Figure 5.8, which shows the difference between $r_e(3.7)$ and $r_e(2.1)$ per pixel vs H_σ. This figure shows that for an overwhelming majority of the analyzed pixels, $r_e(2.1)$ is much larger that $r_e(3.7)$. *Zhang & Platnick (2011)* showed similar results; while their study found that $r_e(3.7)$ had a weak dependence on H_σ, they also encountered large negative $r_e(3.7) - r_e(2.1)$ for increasing H_σ.

5.6 Smooth cloud examination

In order to further assess the effect of cloud heterogeneity upon the r_e retrievals, we introduce a version of the MODIS data that has the "plane-parallel threshold" of H_σ < 0.112, as

described in Section 4.2.5. The results for *re(1.6)*, *re(2.1)*, and *re(3.7)* are shown in Figures 5.9(a-c). While this significantly reduces the samples, it is still enough to demonstrate a pattern. Figure 5.9(a) shows that the mean for $r_e(1.6)$ has been reduced from the original 22.7 µm down to 20.3, closer to the FSSP distribution than before. Figure 5.9(b) shows that the mean for $r_e(2.1)$ has been reduced from 23.6 µm down to 17.7 µm, once again closer to the FSSP distribution. Figure 5.9(c) does not appear to be following the expected pattern of the other two channels. Here the mean for $r_e(3.7)$ has actually increased from the original 14.1 µm up to 15.8 µm. Using the H_σ threshold, the 1.6 and 2.1 µm band r_e datasets are acting "more plane-parallel", which indicates that cloud heterogeneity could likely be a significant factor. The reason for the behavior of the 3.7 µm band when the threshold is applied to it is currently up for speculation.

The overestimation of r_e is straightforward, but the question remains of whether or not the cloud optical depth shows an underestimating behavior, as is usually paired with overestimation of r_e. By viewing the cloud optical depth of the retrieved pixels, and also using a dataset with the H_σ threshold, this question may be explored. The results are shown in Figure 5.10. The retrievals without the threshold have lower values, where Terra has a mean τ of 5.7 and Aqua has a mean τ of 7.2. The retrievals with the H_σ threshold in place show much higher values, with a mean τ of 14.4. This overestimation/underestimation pairing shown supports the idea that plane-parallel theory applied to heterogeneous scenes may induce 3-D effects which end up overestimating effective radius and underestimating optical thickness, as is found in the simulations by *Marshak et al., (2006*).

5.7 Figures

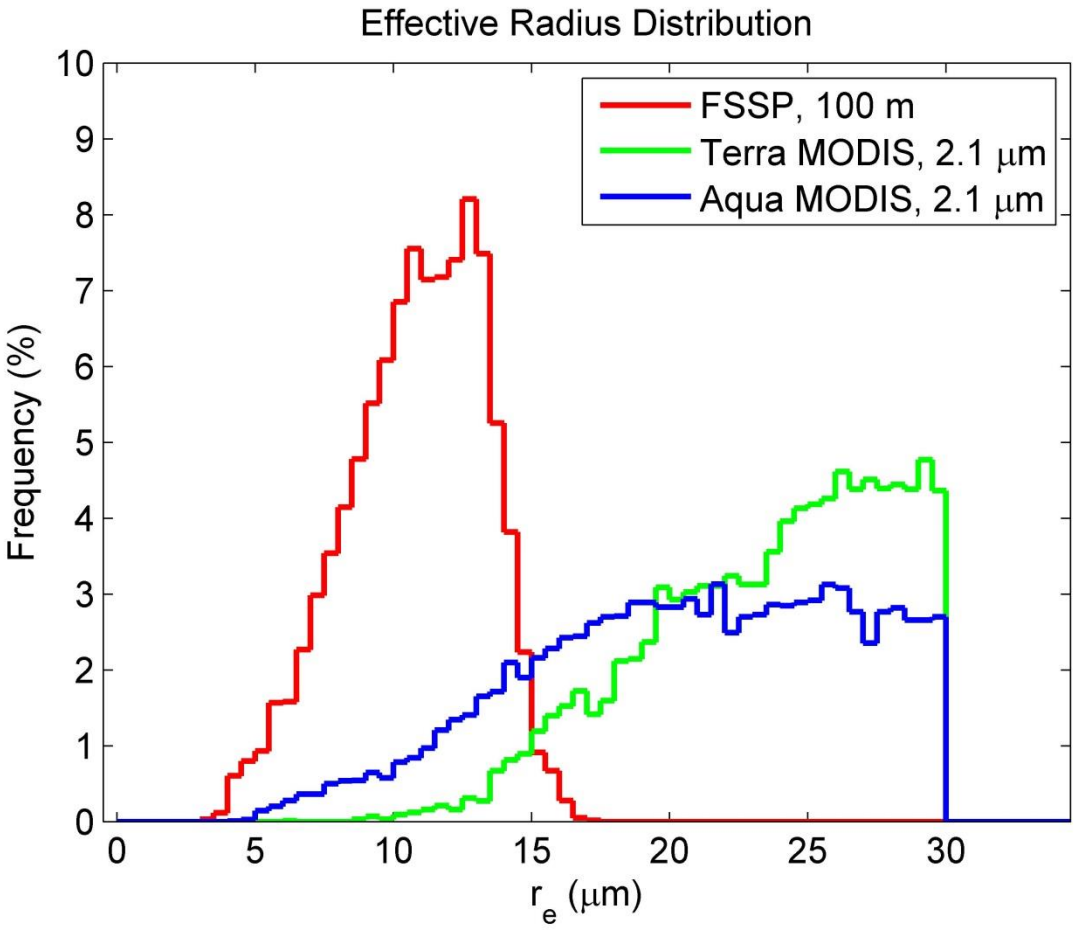

Figure 5.1 – r_e distributions of the FSSP (red), Terra-MODIS (green), and Aqua-MODIS (blue), where r_e in μm is on the x-axis and frequency in percent is on the y-axis.

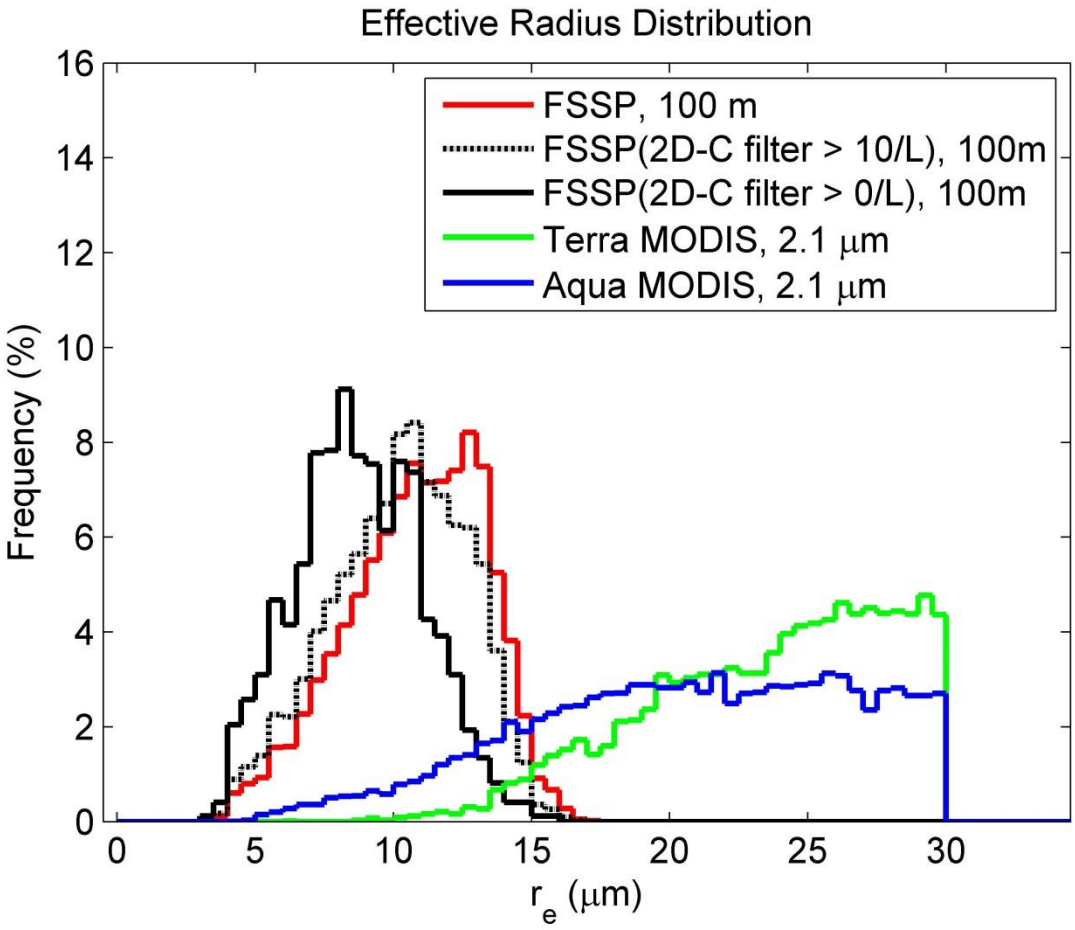

Figure 5.2 – r_e distributions of the FSSP (red), FSSP filtering 2D-C concentrations > 10/L (dotted black), FSSP filtering 2D-C concentrations > 0/L (solid black), Terra-MODIS (green), and Aqua-MODIS (blue), where r_e in μm is on the x-axis and frequency in percent is on the y-axis.

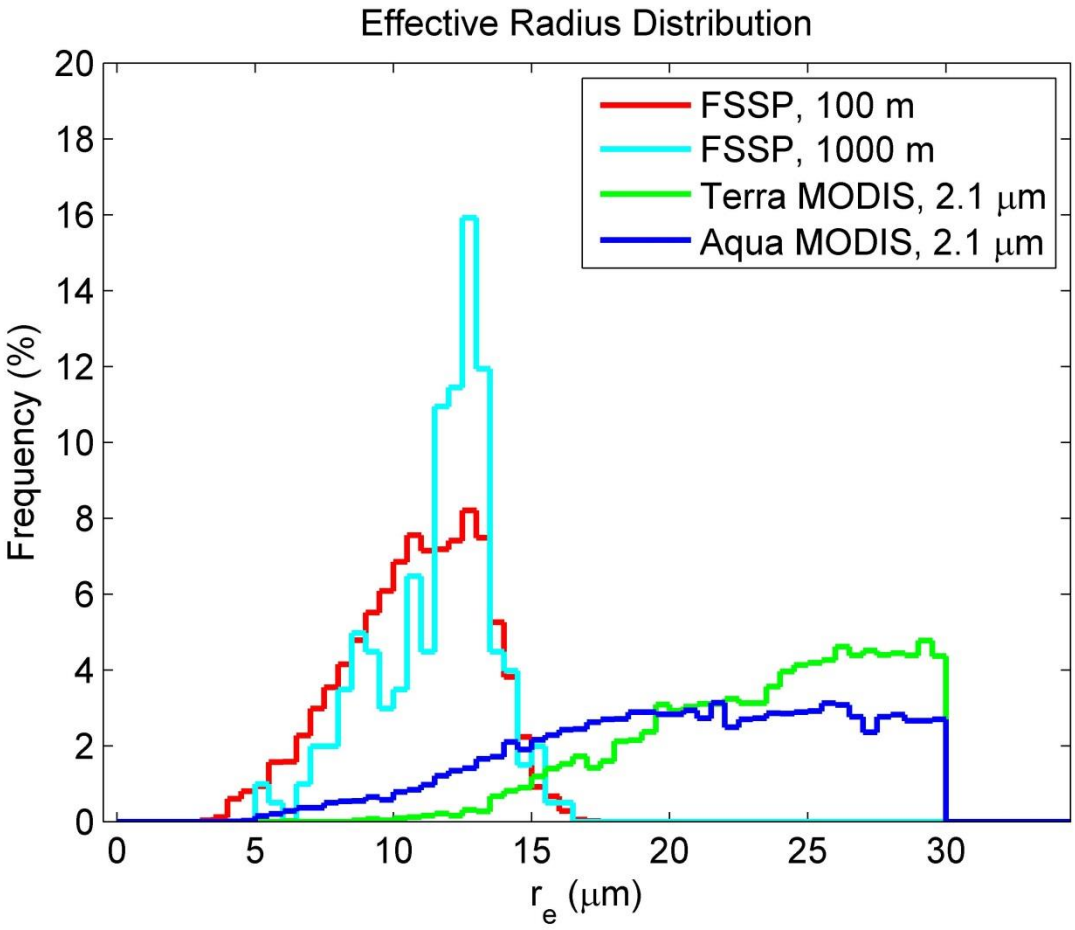

Figure 5.3 – r_e distributions of the FSSP 100 m (red), FSSP 1 km (cyan), Terra (green), and Aqua (blue), where r_e in µm is on the x-axis and frequency in percent is on the y-axis.

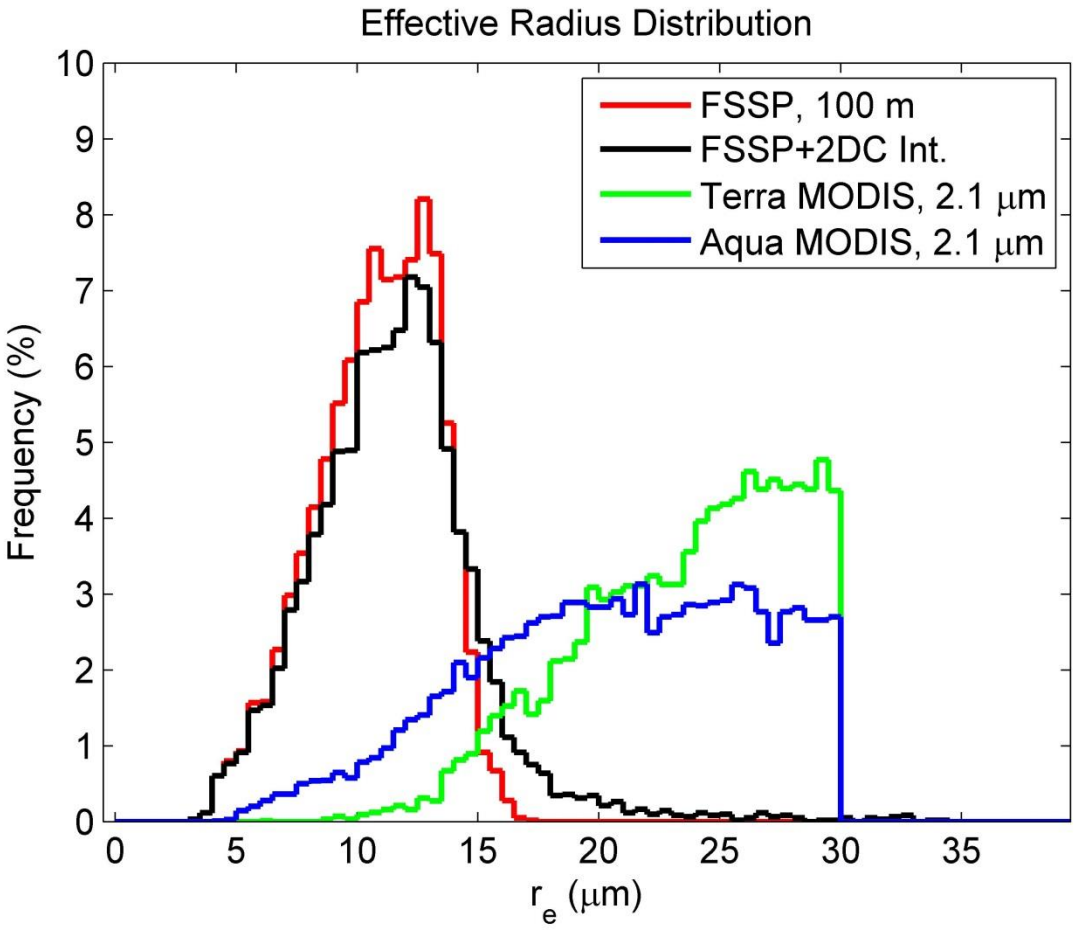

Figure 5.4 – r_e distributions of FSSP (red), FSSP+2D-C Interpolation (black), Terra (green), and Aqua (blue), where r_e in µm is on the x-axis and frequency in percent is on the y-axis.

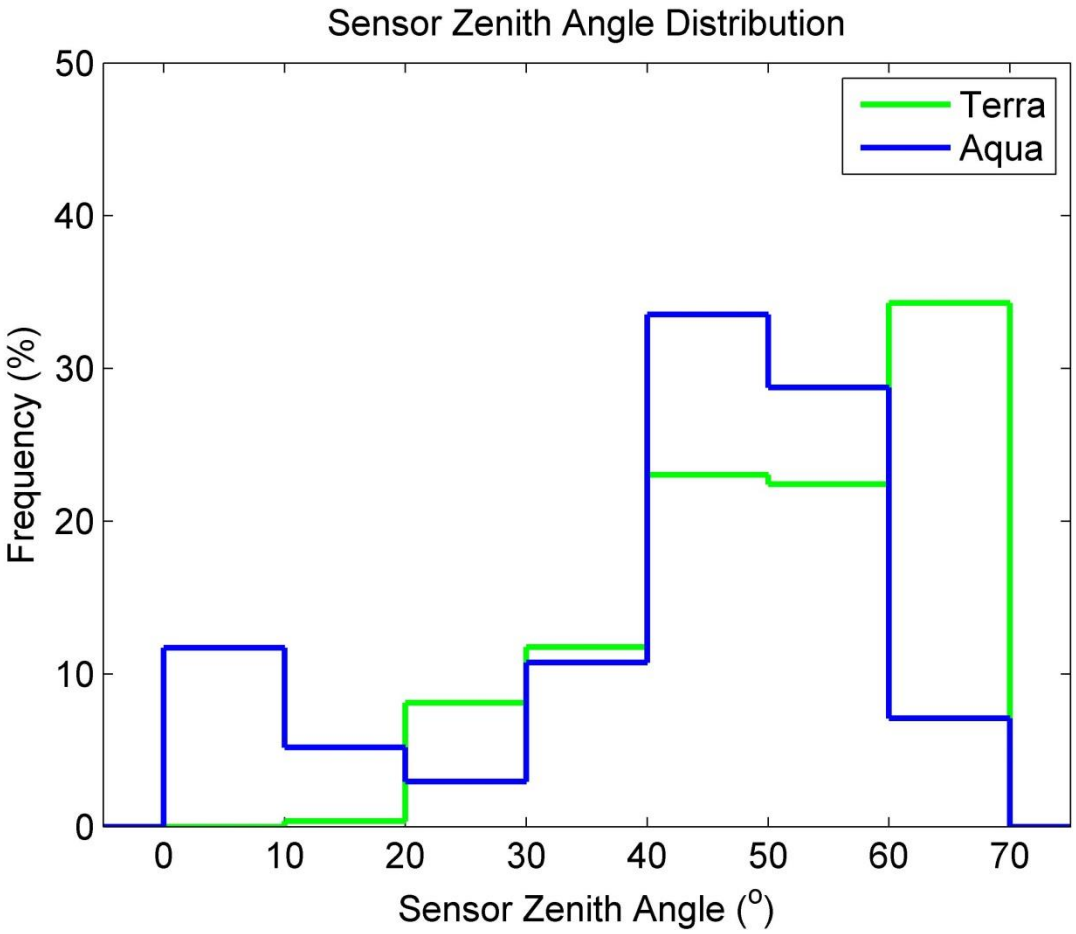

Figure 5.5 – Distribution of sensor zenith angles for retrieved pixels for Terra (green) and Aqua (blue), where sensor zenith angle in degrees is on the x-axis and frequency in percent is on the y-axis.

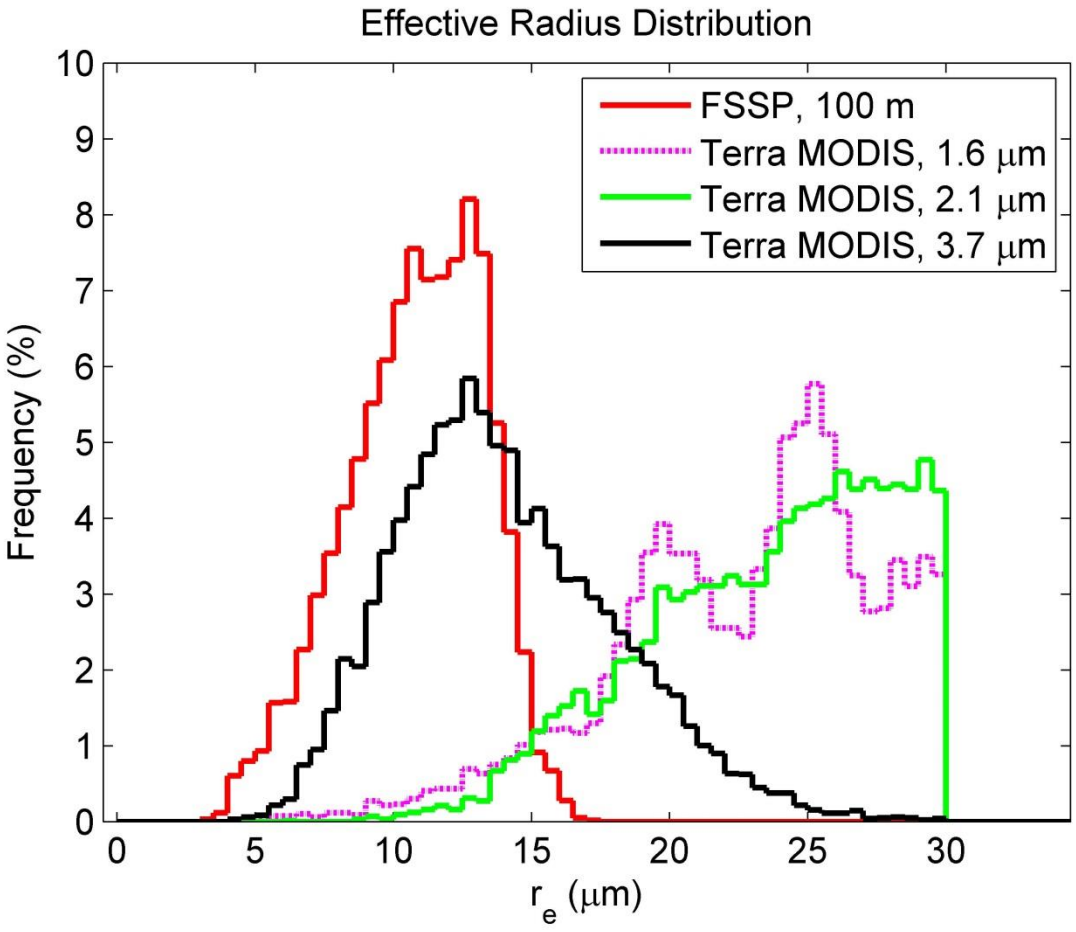

Figure 5.6(a) – r_e distributions of FSSP (red), Terra 1.6 μm (dotted purple), Terra 2.1 μm (green), and Terra 3.7 μm (black), where r_e in μm is on the x-axis and frequency in percent is on the y-axis.

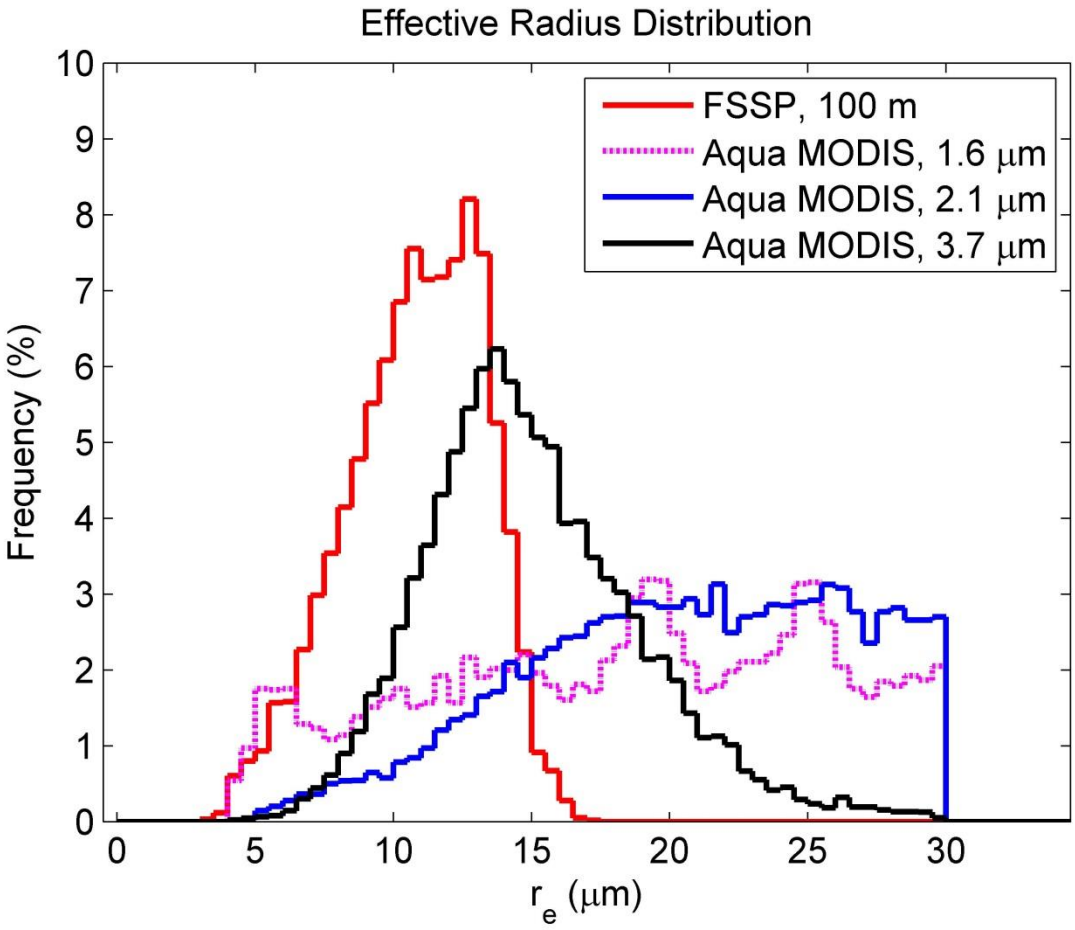

Figure 5.6(b) – r_e distributions of FSSP (red), Aqua 1.6 µm (dotted purple), Aqua 2.1 µm (blue), and Aqua 3.7 µm (black), where r_e in µm is on the x-axis and frequency in percent on the y-axis.

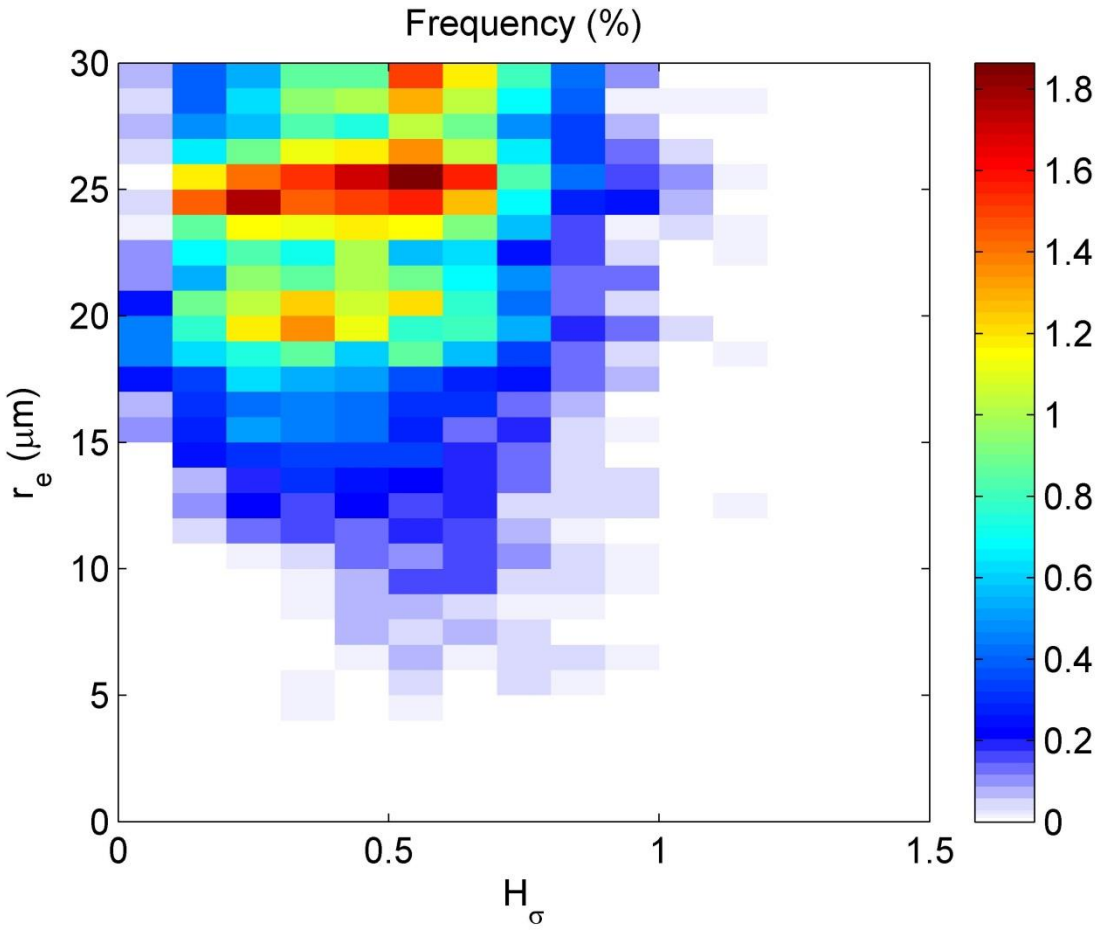

Figure 5.7(a) – Density plot of Terra H_σ vs $r_e(1.6)$, where H_σ is on the x-axis, r_e in µm is on the y-axis, and the colors represent the frequency in percent.

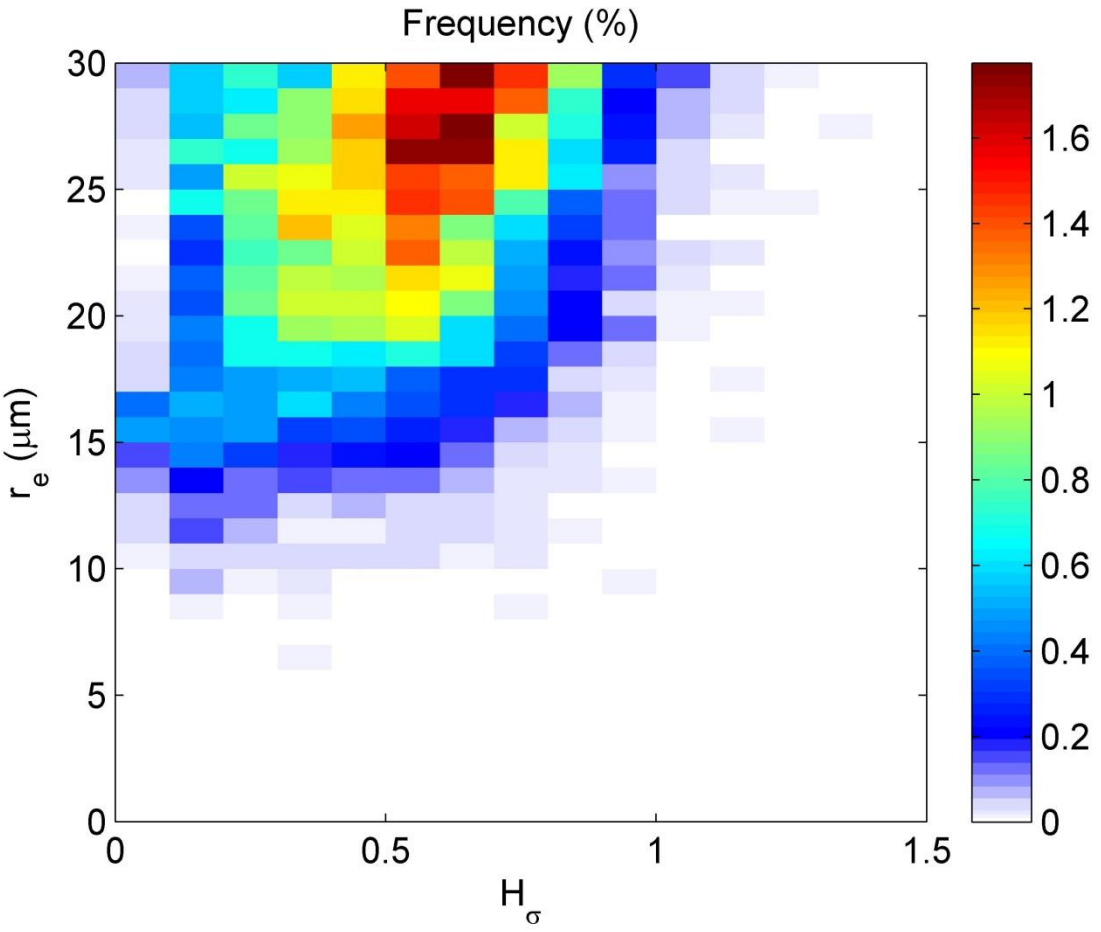

Figure 5.7(b) – Density plot of Terra H_σ vs r_e*(2.1)*, where H_σ is on the x-axis, r_e in µm is on the y-axis, and the colors represent the frequency in percent.

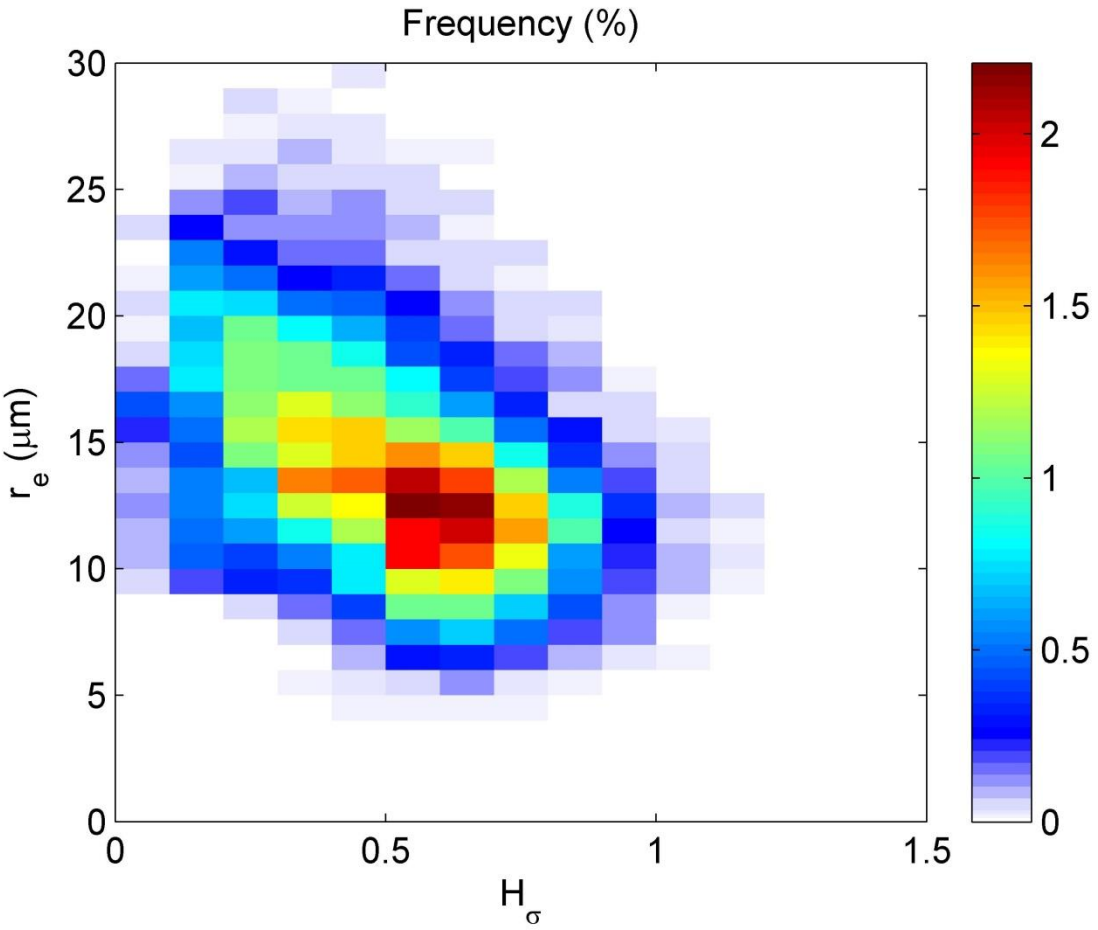

Figure 5.7(c) – Density plot of Terra H_σ vs r_e*(3.7)*, where H_σ is on the x-axis, r_e in µm is on the y-axis, and the colors represent the frequency in percent.

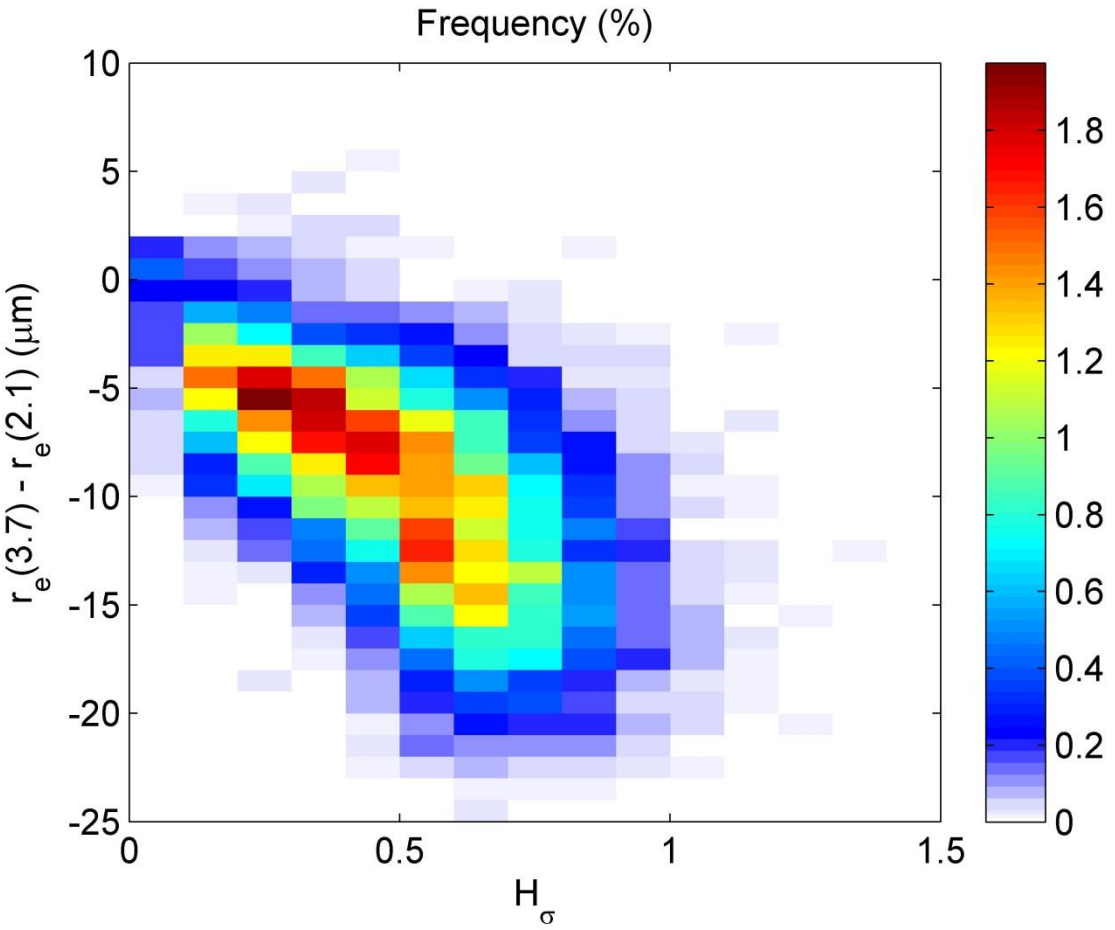

Figure 5.8 – Density plot of Terra H_σ vs the difference between $r_e(3.7)$ and $r_e(2.1)$, where H_σ is on the x-axis, $r_e(3.7)$-$r_e(2.1)$ in µm is on the y-axis, and the colors represent the frequency in percent.

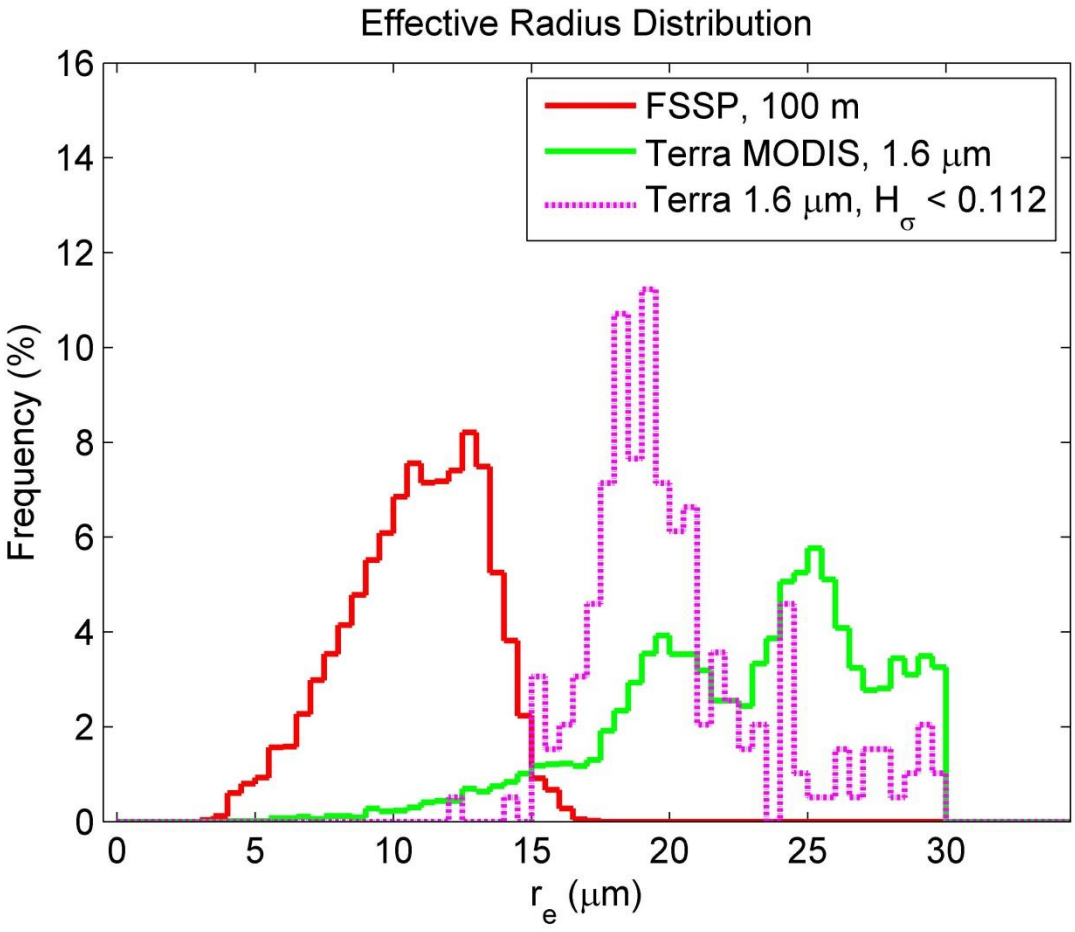

Figure 5.9(a) - Frequency of the r_e distributions of the FSSP 100m (red), Terra $r_e(1.6)$ (green), and Terra $r_e(1.6)$ with the H_σ threshold (dotted purple), where r_e in μm is on the x-axis and frequency in percent is on the y-axis.

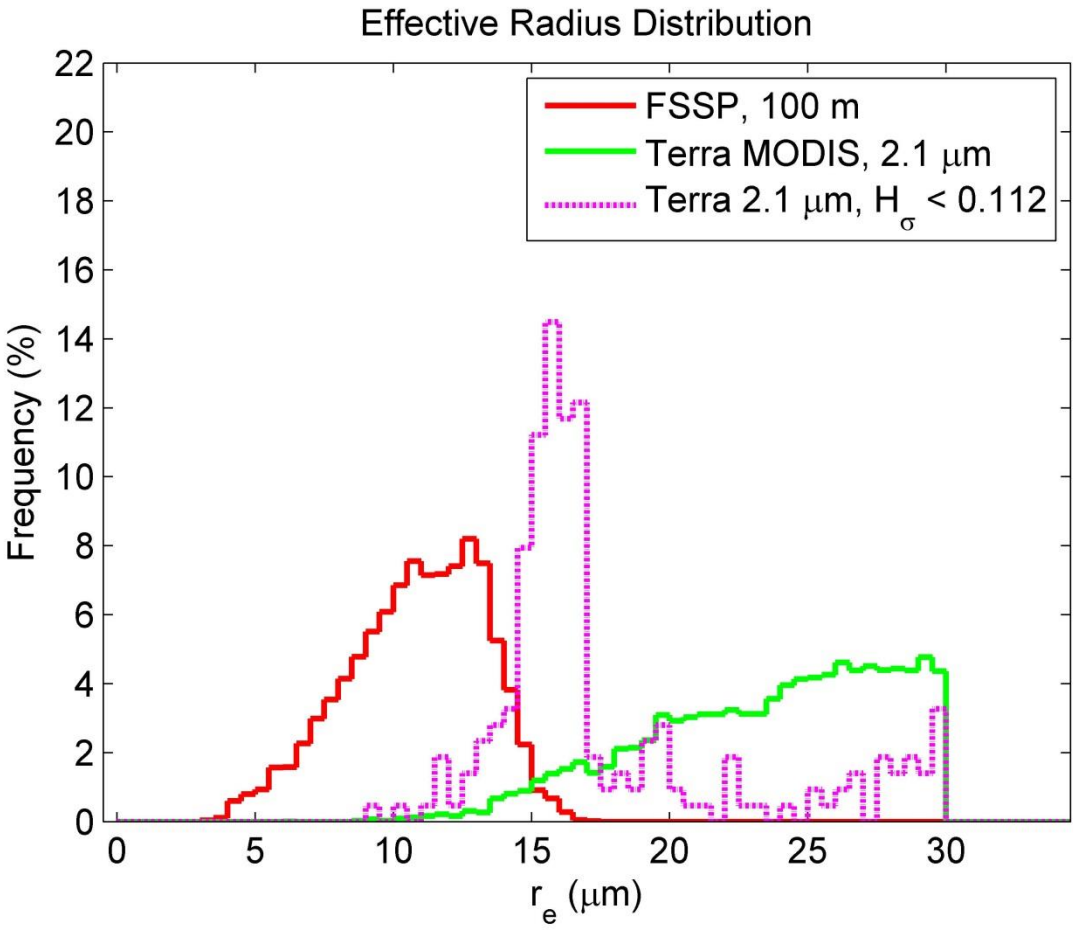

Figure 5.9(b) – Frequency of the r_e distributions of the FSSP 100m (red), Terra $r_e(2.1)$ (green), and Terra $r_e(2.1)$ with the H_σ threshold (dotted purple), where r_e in μm is on the x-axis and frequency in percent is on the y-axis.

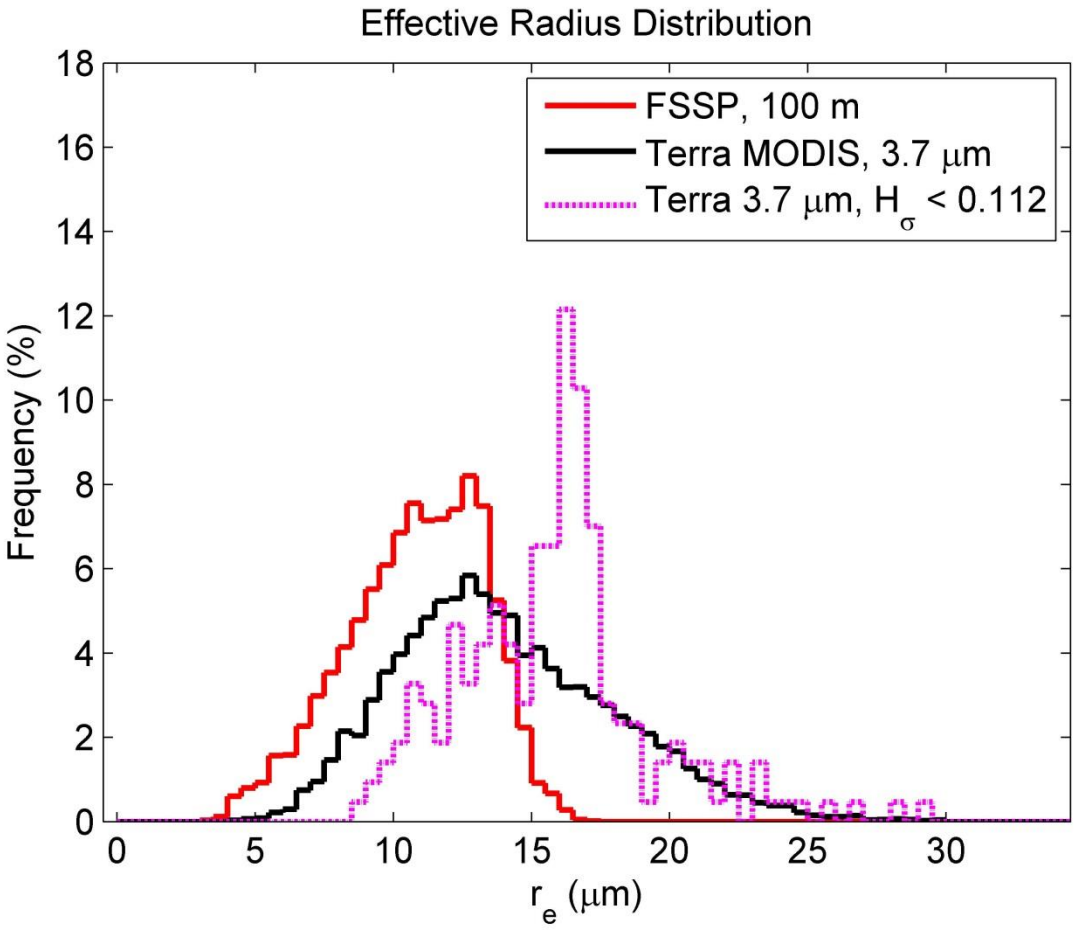

Figure 5.9(c) - Frequency of the r_e distributions of the FSSP 100m (red), Terra $r_e(3.7)$ (black), and Terra $r_e(3.7)$ with the H_σ threshold (dotted purple), where r_e in μm is on the x-axis and frequency in percent is on the y-axis.

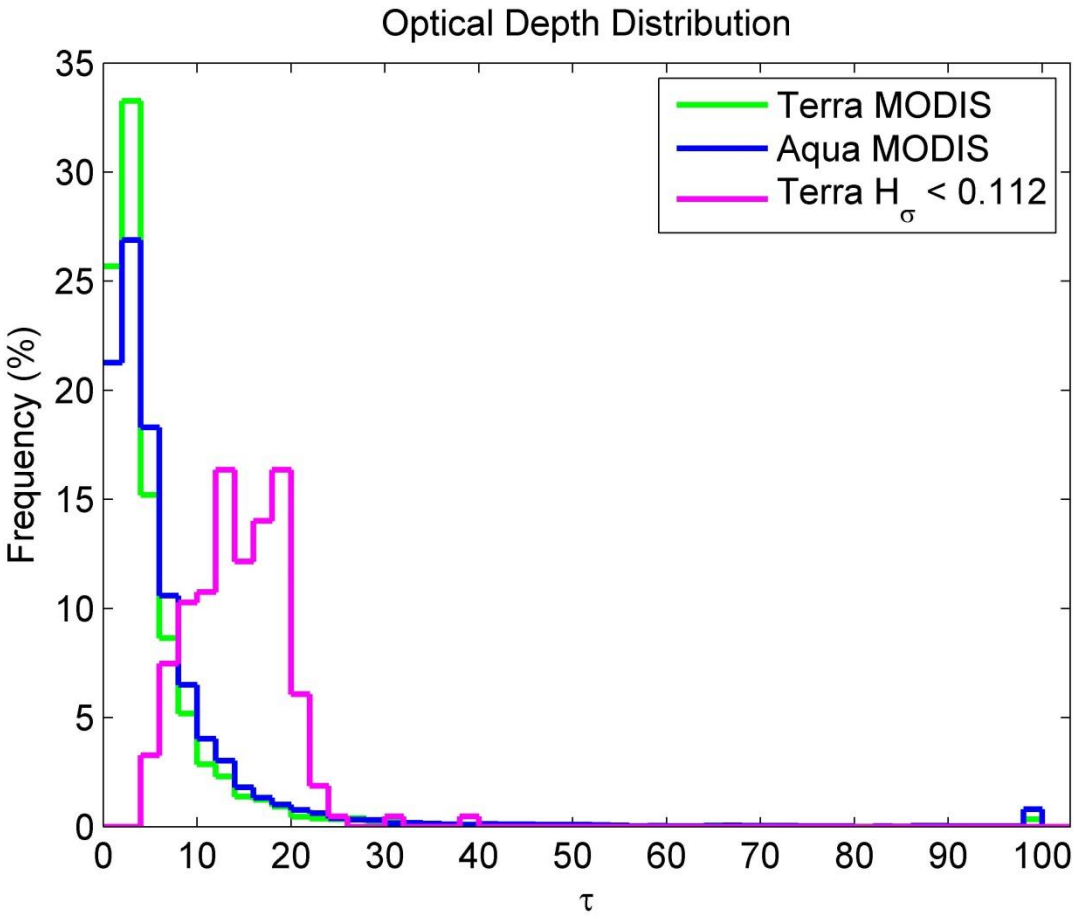

Figure 5.10 - Frequency of the τ distributions of Terra (green), Aqua (blue), and Terra with the H_σ threshold (dotted purple), where τ is on the x-axis and frequency in percent is on the y-axis.

CHAPTER 6

CONCLUSIONS

This study aimed to evolve the knowledge of trade wind cumuli, both in terms of vertical structure and of remotely sensed microphysics. The RICO field campaign was used here to provide insight into what reasonable cloud droplet effective radii could be attained via in-situ measurements from the FSSP-100 and OAP 2D-C instruments aboard the NSF/NCAR C-130Q Hercules. Using this data from the considered research flights, mean vertical profiles of r_e and LWC were constructed, and these profiles seem to provide expected results as compared to prior studies (*Arabas et al., 2009*; *Zhang et al., 2010*).

Using these aircraft measurements as "truth", comparisons with MODIS r_e retrievals for the same days and near the same locations were made. The results showed that MODIS overestimates the r_e retrievals for trade wind cumuli by varying degrees that depended on the spectral channel used in the retrieval. The 1.6 and 2.1 μm channel retrievals overestimated the aircraft data by nearly a factor of 2, while the 3.7 μm retrieval showed a distribution that was more similar to that of the aircraft, though still overestimating by a factor of about a 1.3 for Terra and 1.4 for Aqua. Sensor zenith angle analysis reveals that most of the retrieved pixels are away from nadir, increasing the likelihood of 3-D effects playing a role in skewing the retrievals. The high H_σ values for the retrieved MODIS pixels and their corresponding behavior further enhances this statement. Limiting the MODIS retrievals to those of only $H_\sigma < 0.112$ (i.e. nearly plane-parallel) reduces the mean $r_e(2.1)$ of the retrieved pixels from 23.6 to 17.7 μm for Terra, and also increases the mean τ of the same pixels from 5.7 to 14.4. Using the H_σ threshold for $r_e(1.6)$ also reduces the mean r_e from 22.7 to 20.3 μm. The threshold applied to $r_e(3.7)$ increases

the mean from 14.1 to 15.8 μm, for reasons up for speculation. This analysis has shown a systematic r_e overestimation in the 1.6 and 2.1 μm band, paired with τ underestimation, for heterogeneous trade wind cumuli scenes, and any use of the retrievals in these scenes should be used with caution.

There are some uncertainties in this analysis that should be noted in addition to the instrumental uncertainties. Uncertainties in the in-situ data from the C-130 include the thresholds used for various declarations, such as the number concentration threshold measured by the FSSP to indicate the presence of a cloud. Although it was not the main focus of the analysis, the 2D-C total concentration thresholding could have some uncertainty with it as well—just because the 2D-C did not measure anything does not mean that particle shattering did not affect the FSSP data. We have no clear path to access the magnitude of this uncertainty. In terms of the MODIS retrieval analysis, due to the method used for declaring usable pixels, some of the scans of MODIS could be happening hours apart from when the C-130 was collecting data, and a cloud scene may change significantly in this time period. While it may not be ideal, this is the limitation of a satellite validation study using data from a field campaign. Still, given the small differences between Terra and Aqua, this is likely not a major issue.

Future work should entail more validation studies using H_σ as basis of the accuracy of retrievals from a cloud scene. This should be more accessible in the future, as Collection 6 of the MODIS cloud mask is currently planned to have H_σ as a stored value (*Zhang et al., 2012*). Further along, a proper use of H_σ would be to actually use it in an algorithm to provide some sort of correction to the cloud product. This would render heavily heterogeneous cumuli regions of the globe more viable for accurate use in climate studies.

REFERENCES

Arabas, S., H. Pawlowska, and W. W. Grabowski (2009), Effective radius and droplet spectral width from in-situ aircraft observations in trade-wind cumuli during RICO, *Geophys. Res. Lett., 36*, L11803, doi:10.1029/2009GL038257.

Baker, B., Q. Mo, R. P. Lawson, D. O'Connor, A. Korolev (2008), The effects of precipitation on cloud droplet measurement devices, *J. Atmos. Oceanic. Technol., 26,* 1404-1409, doi: 10.1175/2009JTECHA1191.1.

Bréon, F., and M. Doutriaux-Boucher (2005), A comparison of cloud droplet radii measured from space, *IEEE Trans. Geosci. Remote Sens., 43,* 1796-1805, doi: 10.1109/TGRS.2005852838.

Colón-Robles, M., R. M. Rauber, and J. B. Jensen (2006), Influence of low-level wind speed on droplet spectra near cloud base in trade wind cumulus, *Geophys. Res. Lett., 33*, L20814, doi: 10.1029/2006GL027487.

Di Girolamo, L., L. Liang, and S. Platnick (2010), A global view of one-dimensional solar radiative transfer through oceanic water clouds, Geophys. Res. Lett.,37, L18809, doi:10.1029/2010GL044094.

Dye, J, E., and D. Baumgardner (1984), Evaluation of the Forward Scattering Spectrometer Probe. Part I: Electronic and Optical Studies, *J. Atmos. Oceanic Technol.,1,* 329-344.

Hansen, J. E., and L. D. Travis (1974), Light scattering in planetary atmospheres. *Space Sci. Rev.*, *16*, 527-610.

Heymsfield, A. J., and J. L. Parrish (1978), A computational technique for increasing the effective sampling volume of the PMS two-dimensional particle size spectrometer, *J. Appl. Meteorol., 17,* 1566-1572.

King, N. J., K. N. Bower, J. Crosier, and I. Crawford (2013), Evaluating MODIS cloud retrievals with in situ observations from VOCALS-Rex, *Atmos. Chem. Phys.,13*, 191-209, doi: 10.5194/acp-13-191-2013.

Kuji, M., T. Hayasaka, N. Kikuchi, T. Nakajima, M. Tanaka (2000), The retrieval of effective particle radius and liquid water path of low-level marine clouds from NOAA AVHRR data, *J. Appl. Meteor., 39,* 999-1016, doi: 10.1175/1520-0450(2000)039<0999:TROEPR>2.0.CO;2.

Liang, L., L. Di Girolamo, and S. Platnick (2009), View-angle consistency in reflectance, optical thickness, and spherical albedo of marine water-clouds over the northeastern Pacific through MISR-MODIS fusion, *Geophys. Res. Lett., 36,* L09811, doi: 10.1029/2008GL037124.

Maddux, B. C., S. A. Ackerman, and S. Platnick (2010), Viewing geometry dependencies in MODIS Cloud Products, *J. Atmos. Oceanic Technol.*,*27,*1519-1528, doi:10.1175/2010JTECHA1432.1.

Marshak, A., S. Platnick, T. Várnai, G. Wen, and R. F. Cahalan (2006), Impact of three-dimensional radiative effects on satellite retrievals of cloud droplet sizes, *J. Geophys. Res., 111,* D09207, doi:10.1029/2005JD006686.

Nakajima, T., and M. D. King (1990), Determination of the optical thickness and effective particle radius of clouds from reflected solar radiation measurements. Part I: Theory, *J. Atmos. Sci. 47*(15), 1878-1893.

Nakajima, T., M. D. King, J. D. Spinhirne, L. F. Radke (1991), Determination of the optical thickness and effective particle radius of clouds from reflected solar radiation measurements. Part II: Marine stratocumulus observations, *J. Atmos. Sci., 48,* 728-751, doi: 10.1175/1520-0469(1991)048<0728:DOTOTA>2.0.CO;2.

Nakajima, T. Y., K. Suzuki, and G. L. Stephens (2010), Droplet growth I warm water clouds observed by the A-train. Part I: Sensitivity analysis of the MODIS-derived cloud droplet sizes, *J. Atmos. Sci., 67*(6), 1884-1896, doi:10.1175/2009JAS3280.1.

Nakajima, T. Y., A. Uchiyama, T. Takamura, N. Tsujioka, T. Takemura, T. Nakajuma (2005), Comparisons of warm cloud properties obtained from satellite, ground, and aircraft measurements during APEX intensive observation period in 2000 and 2001, *J. Meteor. Soc. Japan, 83,* 1085-1095.

Oreopoulos, L., and S. Platnick (2008), Radiative susceptibility of cloudy atmospheres to droplet number perturbations: 2. Global analysis from MODIS, *J. Geophys. Res., 113,* D14S21, doi:10:1029/2007JD009655.

Painemal, D., and P. Zuidema (2011), Assessment of MODIS cloud effective radius and optical thickness retrievals over the southeast pacific with VOCALS-Rex in situ measurements (2011), *J. Geophys. Res., 116,* D24206, doi:10.1029/2011JD016155.

Pinnick, R. G., D. M. Garvey, L. D. Duncan (1981), Calibration of Knollenberg FSSP light-scattering counters for measurement of cloud droplets, *J. Appl. Meteor., 20,* 1049-1057, doi: 10.1175/1520-0450(1981)020<1049:COKFLS>2.0.CO;2.

Platnick, S., F.P.J. Valero (1995), A validation of a satellite cloud retrieval during ASTEX, *J. Atmos. Sci., 52,* 2985-3001.

Platnick, S., and S. Twomey (1994), Determining the susceptibility of cloud albedo to changes in droplet concentration with the Advanced Very High Resolution Radiometer, *J. Appl. Meteorol., 33*,334-347,doi:10.1175/1520-0450(1994)033<0334:DTSOCA>2.0CO;2.

Platnick, S., M. D. King, S. A. Ackerman, W. P. Menzel, B. A. Baum, J. C. Riedi, and R. A. Frey (2003), The MODIS cloud products: Algorithms and examples from Terra, *IEEE Trans. Geosci. Remote Sens., 41*(2), 459-473, doi:10.1109/TGRS.2002.808301.

Platnick, S (2000), Vertical photon transport in cloud remote sensing problems, *J. Geophys. Res., 105*, pp. 22919-22935.

Rauber, R., et al. (2007), Rain in shallow cumulus over the ocean—The RICO campaign, *Bull. Am. Meteorol. Soc., 88*, 1912 – 1928.

Snodgrass, E. R., L. Di Girolamo, R. M. Rauber (2008), Precipitation characteristics of trade wind clouds during RICO derived from radar, satellite, and aircraft measurements, *J. Appl. Meteor. Clim.,48*,464-483.

Szczodrak, M., P. H. Austin, P. B. Krummel (2001), Variability of optical depth and effective radius in marine stratocumulus clouds, *J. Atmos. Sci., 58*, 2912-2926, doi: 10.1175/1520-0469(2001)058<2912:VOODAE>2.0.CO;2.

Seethala, C., and Á. Horváth (2010), Global assessment of AMSR-E and MODIS cloud liquid water path retrievals in warm oceanic clouds, *J. Geophys. Res., 115*, D13202, doi:10.1029/2009JD012662.

Twomey, S. (1974), Pollution and the planetary albedo, *Atmos. Environ., 8*, 1251-1256, doi:10.1016/0004-6981(74)90004-3.

Várnai, T., and A. Marshak (2003), A method for analyzing how various parts of clouds influence each other's brightness, *J. Geophys. Res., 108*(D22), 4706, doi:10.1029/2003JD003561.

Wetzel, M. A., W. T. Thompson, G. Vali, S. K. Chai, T. Haack, M. J. Szumowski, R. Kelly (2001), Evaluation of COAMPS forecasts of coastal stratus using satellite microphysical retrievals and aircraft measurements, *Wea. Forecasting, 16*, 588-599, doi: 10.1175/1520-0434(2001)016<0588:EOCFOC>2.0.CO;2.

Zhang, S., H. Xue, and G. Feingold (2011), Vertical profiles of droplet effective radius in shallow convective clouds, *Atmos. Chem. Phys.,11*, 4633-4644, doi:10.5194/acp-11-4633-2011.

Zhang, Z., and S. Platnick (2011), An assessment of differences between cloud effective particle radius retrievals for marine water clouds from three MODIS spectral bands, *J. Geophys. Res., 116*, D20215, doi:10.1029/2011JD016216.

Zhang, Z., A. S., Ackerman, G. Feingold, S. Platnick, R. Pincus, and H. Xue (2012), Effects of cloud horizontal inhomogeneity and drizzle on remote sensing of cloud droplet effective radius: Case studies based on large-eddy simulations, *J. Geophys. Res., 117*, D19208, doi: 10.1029/2012JD017655.

Zhao, G., and L. Di Girolamo (2007), Statistics on the macrophysical properties of trade wind cumuli over the tropical western Atlantic, *J. Geophys. Res., 112*, D10204, doi:10.1029/2006JD007371.

Zinner, T., G. Wind, S. Platnick, and A. S. Ackerman (2010), Testing remote sensing on artificial observations: Impact of drizzle and 3-D cloud Structure on effective radius retrievals, *Atmos. Chem. Phys., 10*(19), 9535-9549, doi:10.5194/acp-10-9535-2010.

APPENDIX A

This section is dedicated to showing the individual C-130 research flight vertical profiles for the 1 second averaged data, whereas in the analysis all flights from RF03 – RF18 were used together, except for RF17. The following figures have no 2D-C thresholding applied, and the color bar represents the frequency in counts of the in-cloud 1 second data points for that flight only.

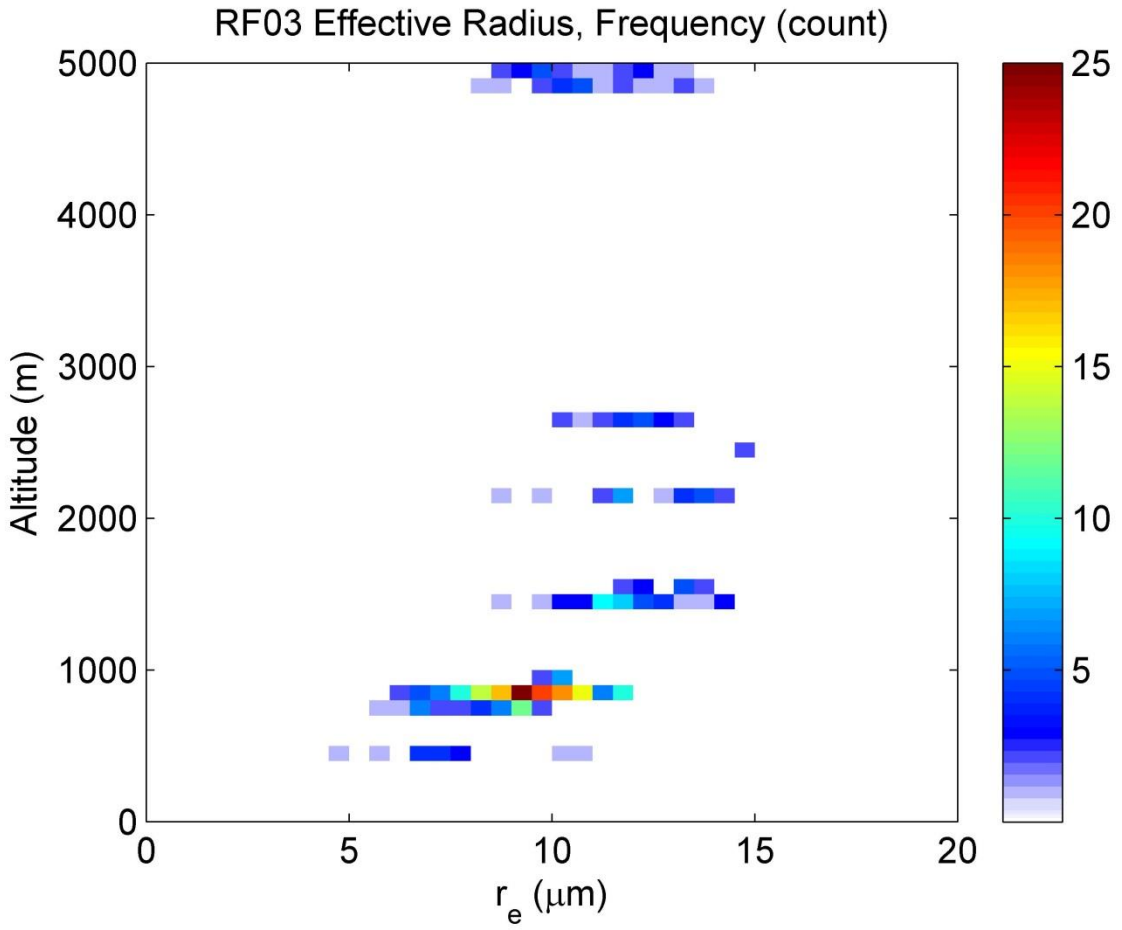

Figure A.1(a) – r_e distribution for RF03, where r_e in μm is on the x-axis, altitude in meters is on the y-axis, and the colors represent the frequency in number of points

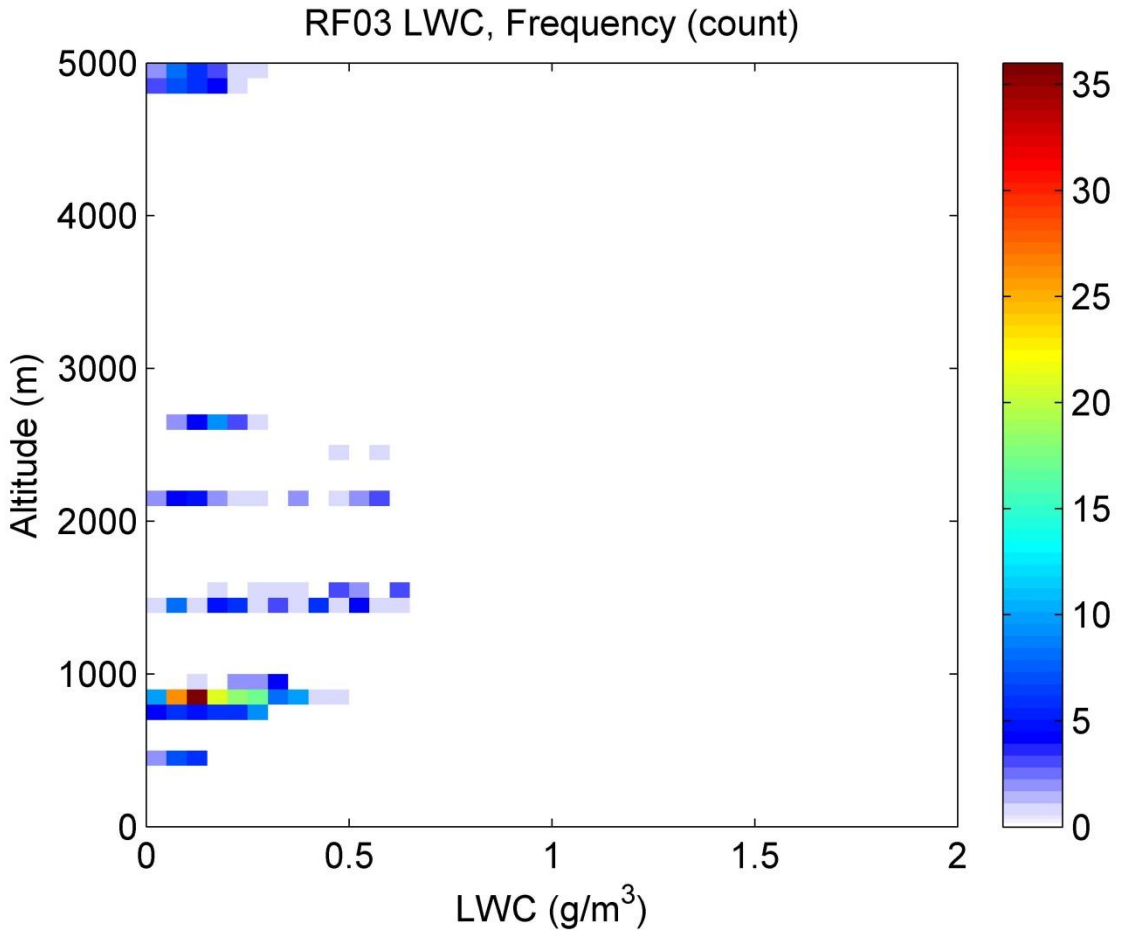

Figure A.1(b) – LWC distribution for RF03, where LWC in g/m^3 is on the x-axis, altitude in meters is on the y-axis, and the colors represent the frequency in number of points.

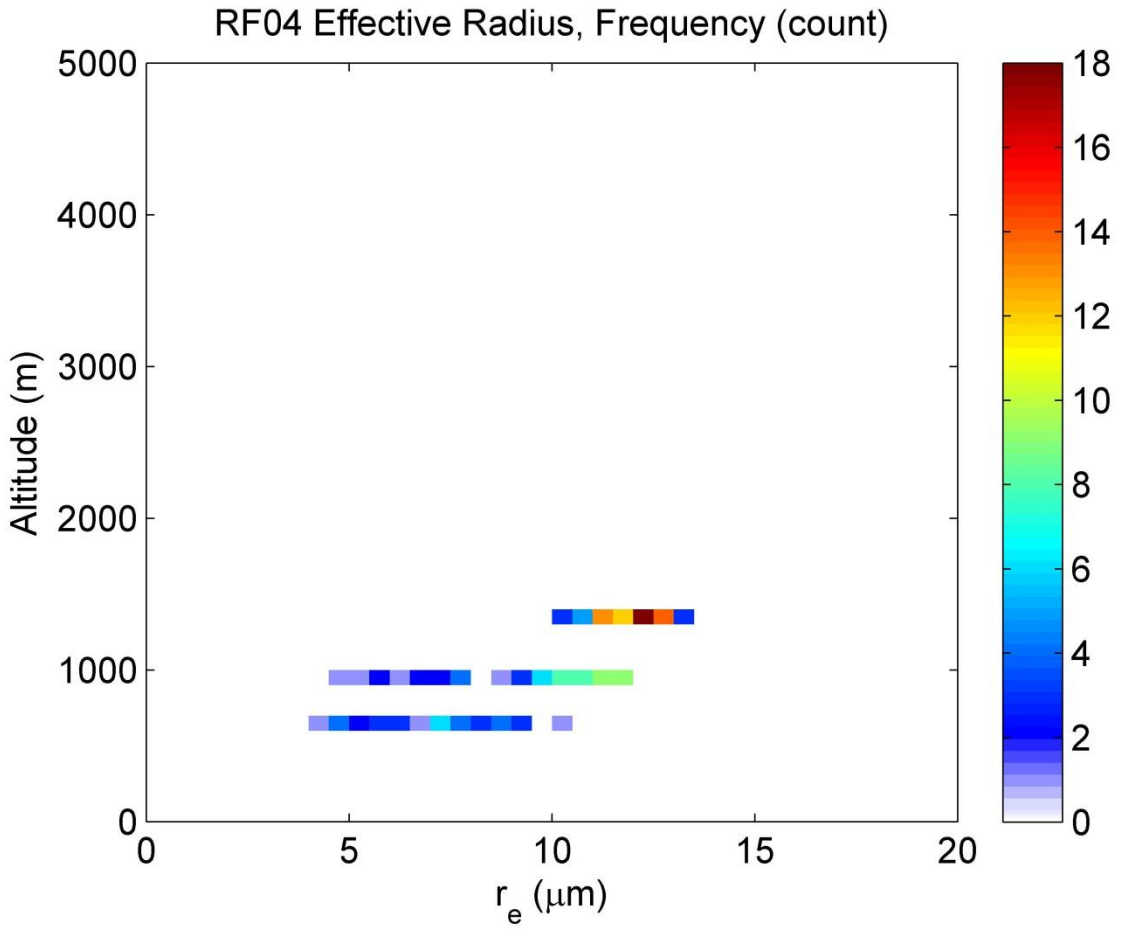

Figure A.2(a) – r_e distribution for RF04, where r_e in μm is on the x-axis, altitude in meters is on the y-axis, and the colors represent the frequency in number of points

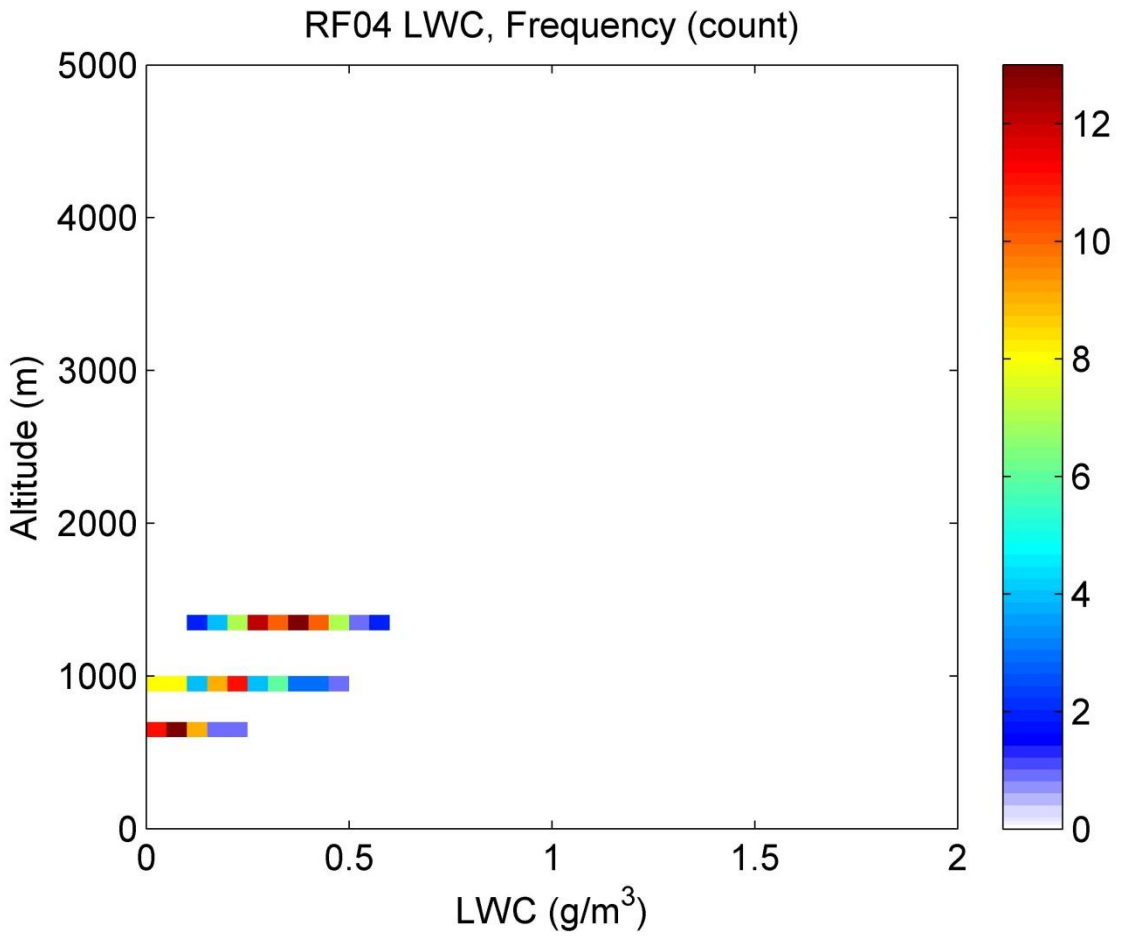

Figure A.2(b) – LWC distribution for RF04, where LWC in g/m^3 is on the x-axis, altitude in meters is on the y-axis, and the colors represent the frequency in number of points.

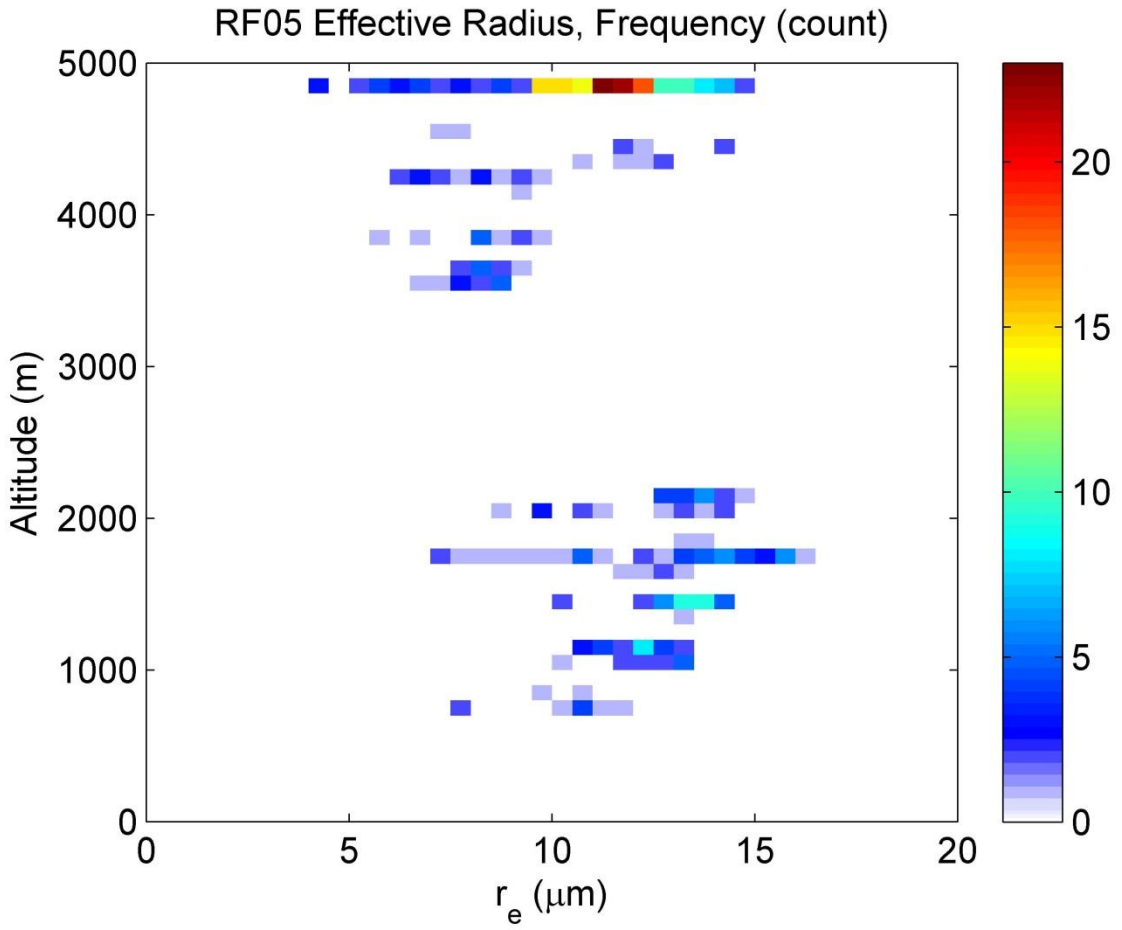

Figure A.3(a) – r_e distribution for RF05, where r_e in μm is on the x-axis, altitude in meters is on the y-axis, and the colors represent the frequency in number of points

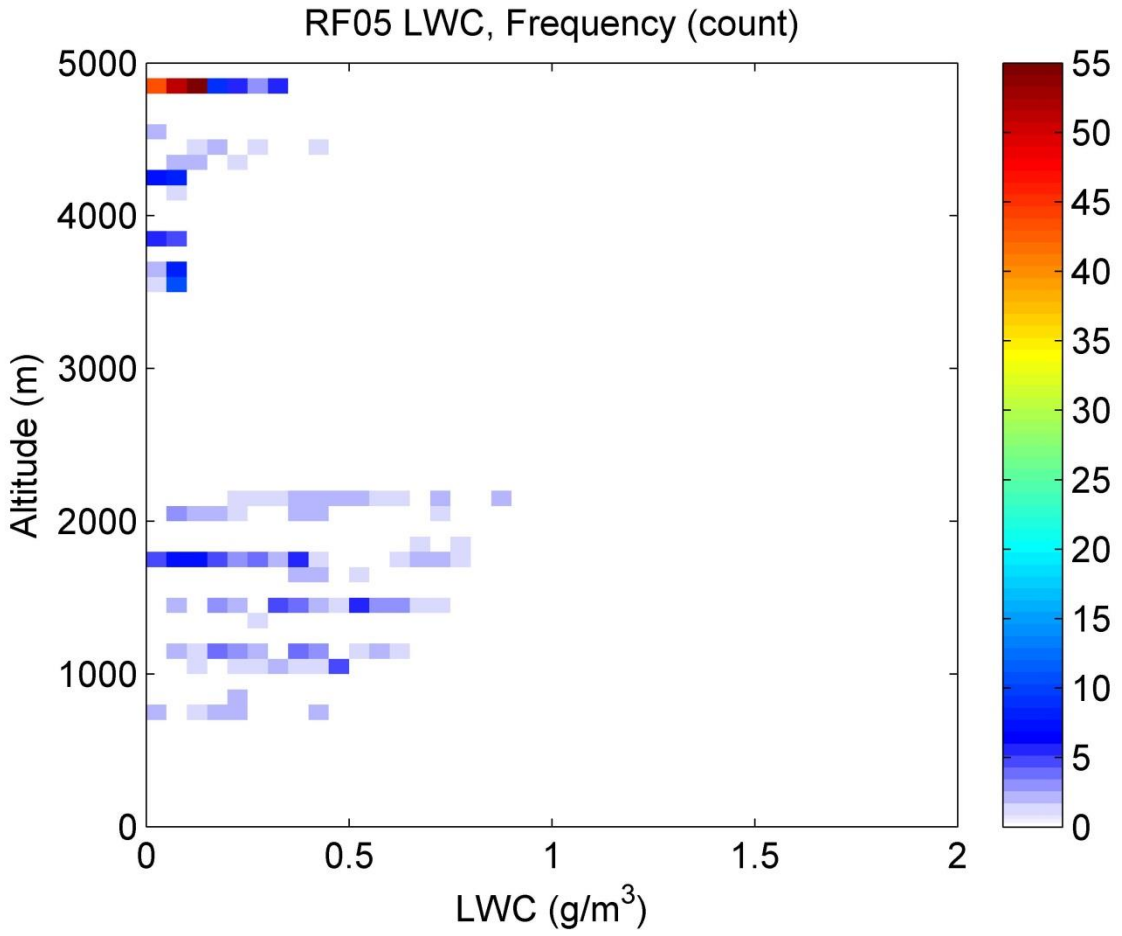

Figure A.3(b) – LWC distribution for RF05, where LWC in g/m^3 is on the x-axis, altitude in meters is on the y-axis, and the colors represent the frequency in number of points.

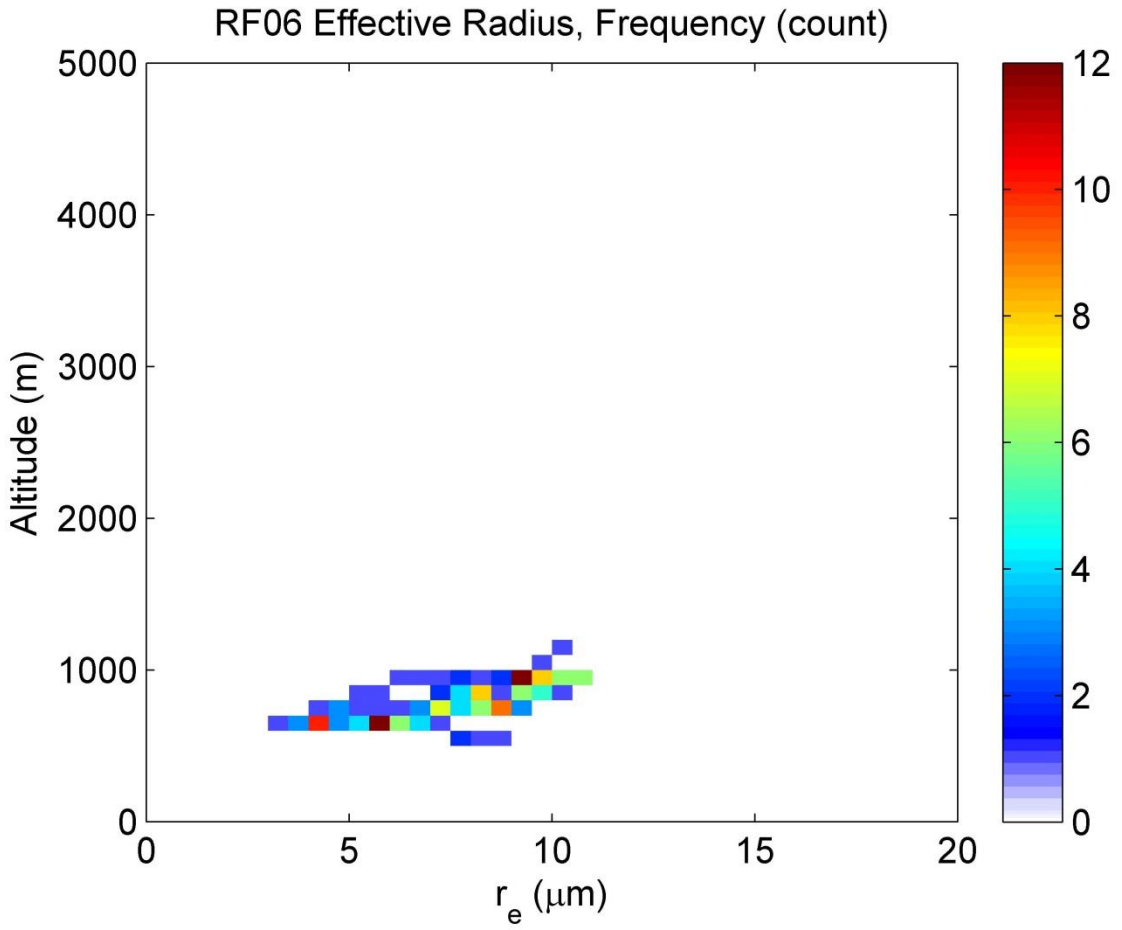

Figure A.4(a) – r_e distribution for RF06, where r_e in μm is on the x-axis, altitude in meters is on the y-axis, and the colors represent the frequency in number of points

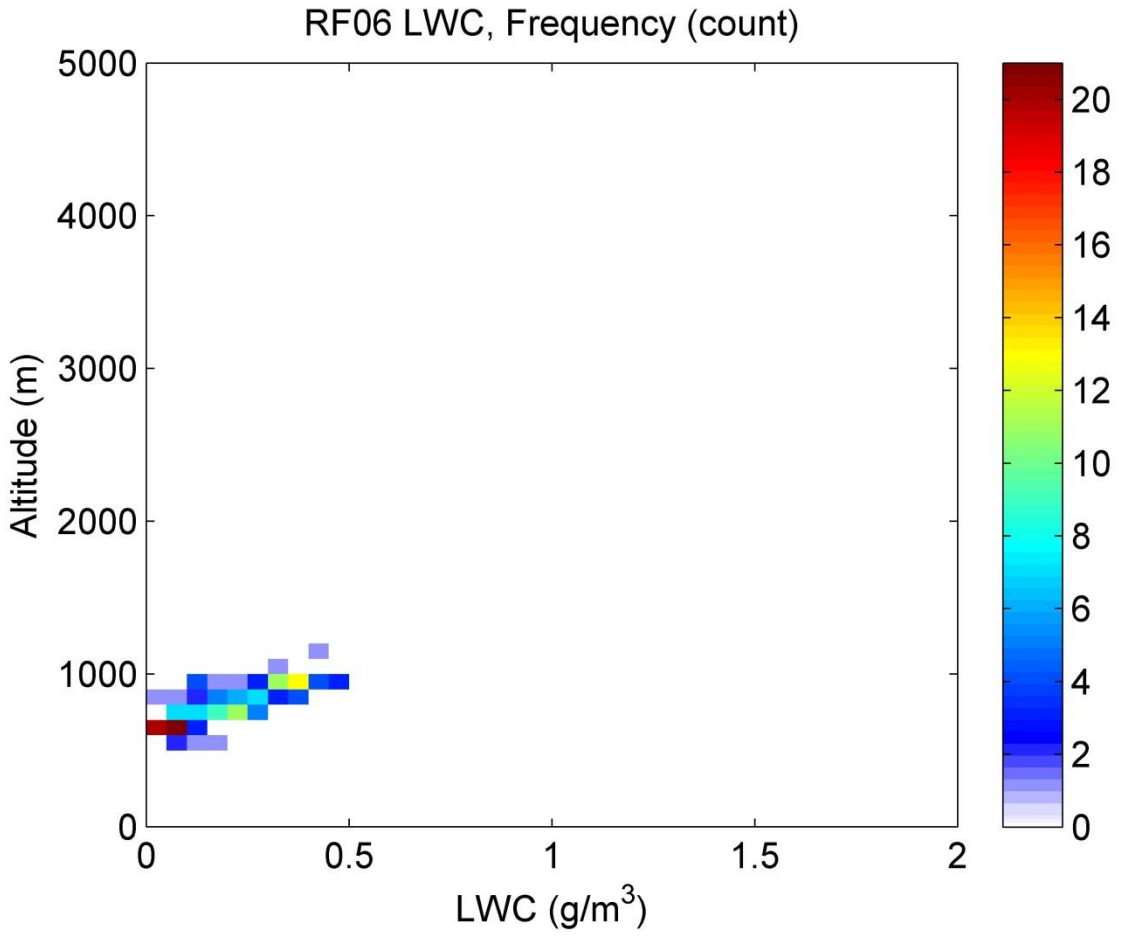

Figure A.4(b) – LWC distribution for RF06, where LWC in g/m^3 is on the x-axis, altitude in meters is on the y-axis, and the colors represent the frequency in number of points.

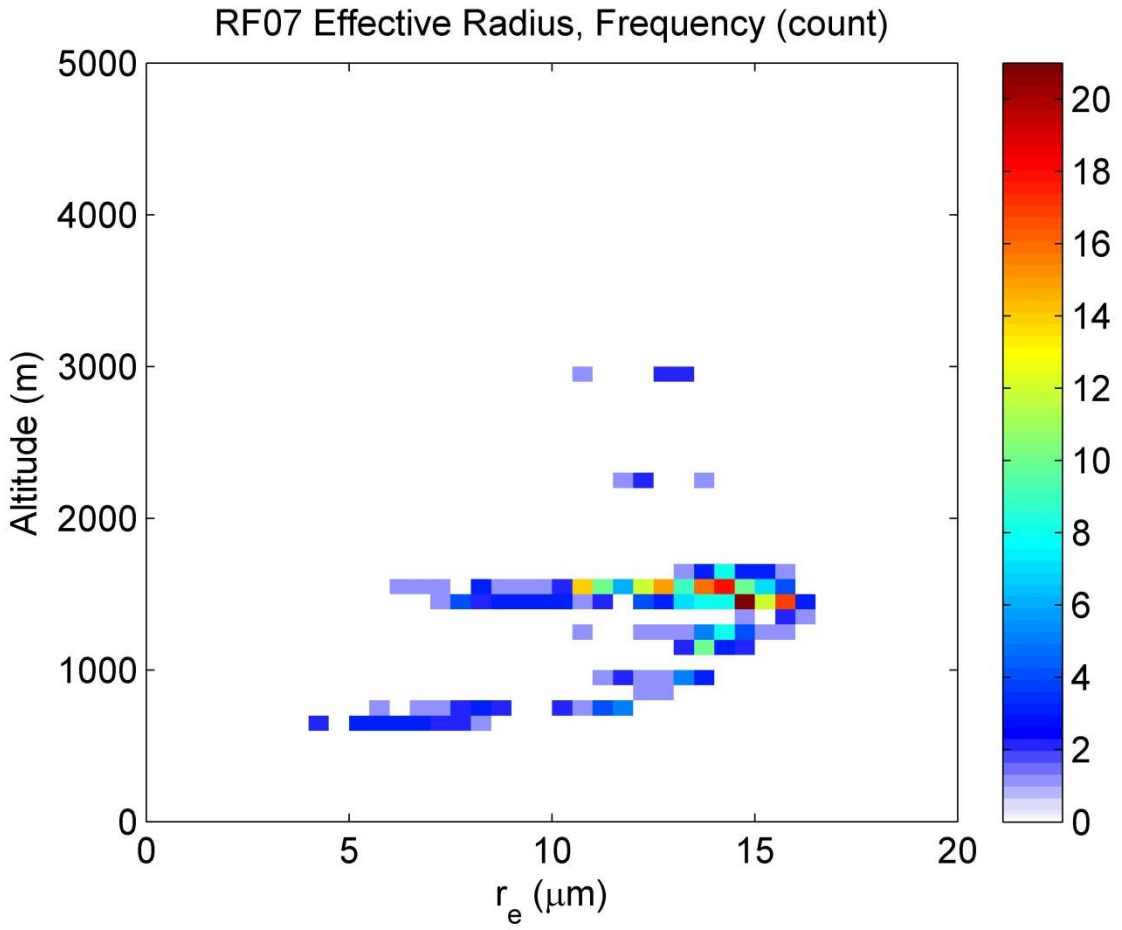

Figure A.5(a) – r_e distribution for RF07, where r_e in μm is on the x-axis, altitude in meters is on the y-axis, and the colors represent the frequency in number of points

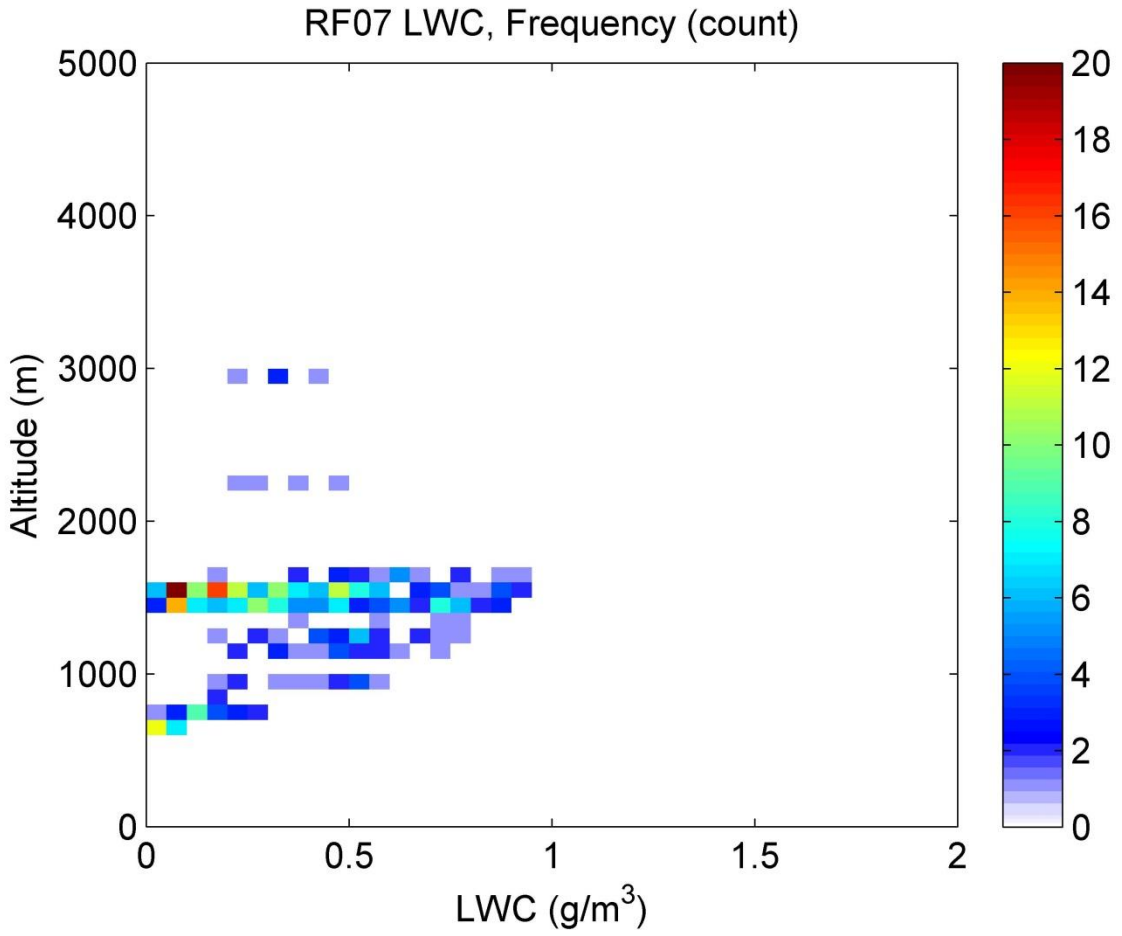

Figure A.5(b) – LWC distribution for RF07, where LWC in g/m^3 is on the x-axis, altitude in meters is on the y-axis, and the colors represent the frequency in number of points.

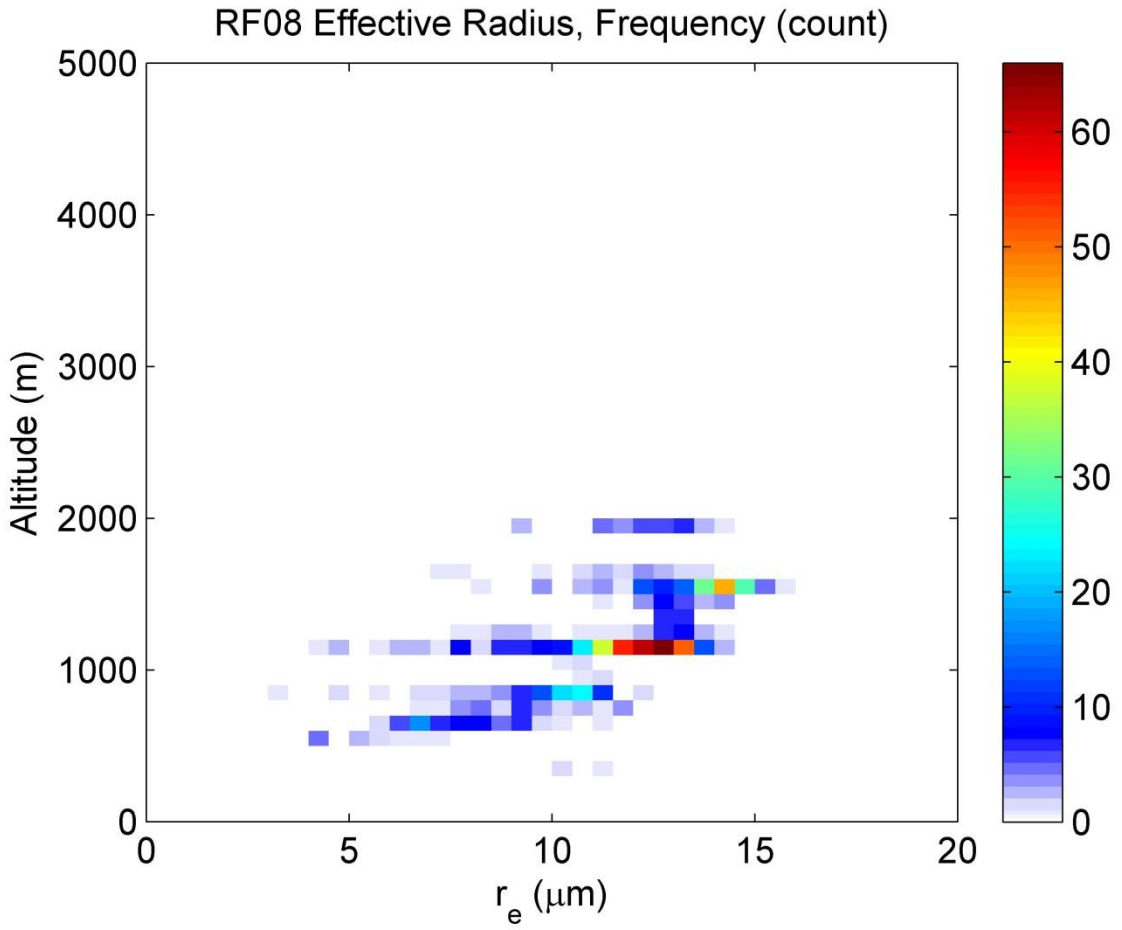

Figure A.6(a) – r_e distribution for RF08, where r_e in μm is on the x-axis, altitude in meters is on the y-axis, and the colors represent the frequency in number of points

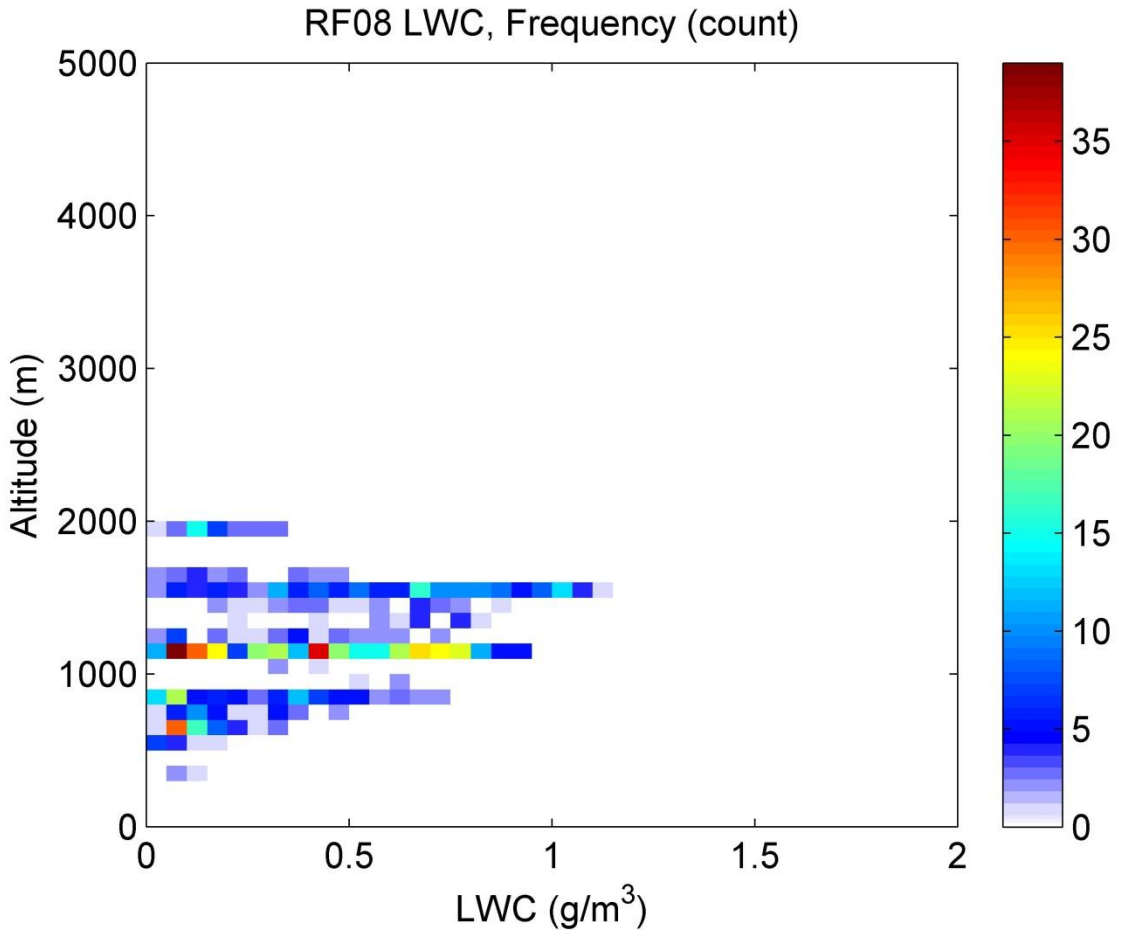

Figure A.6(b) – LWC distribution for RF08, where LWC in g/m^3 is on the x-axis, altitude in meters is on the y-axis, and the colors represent the frequency in number of points.

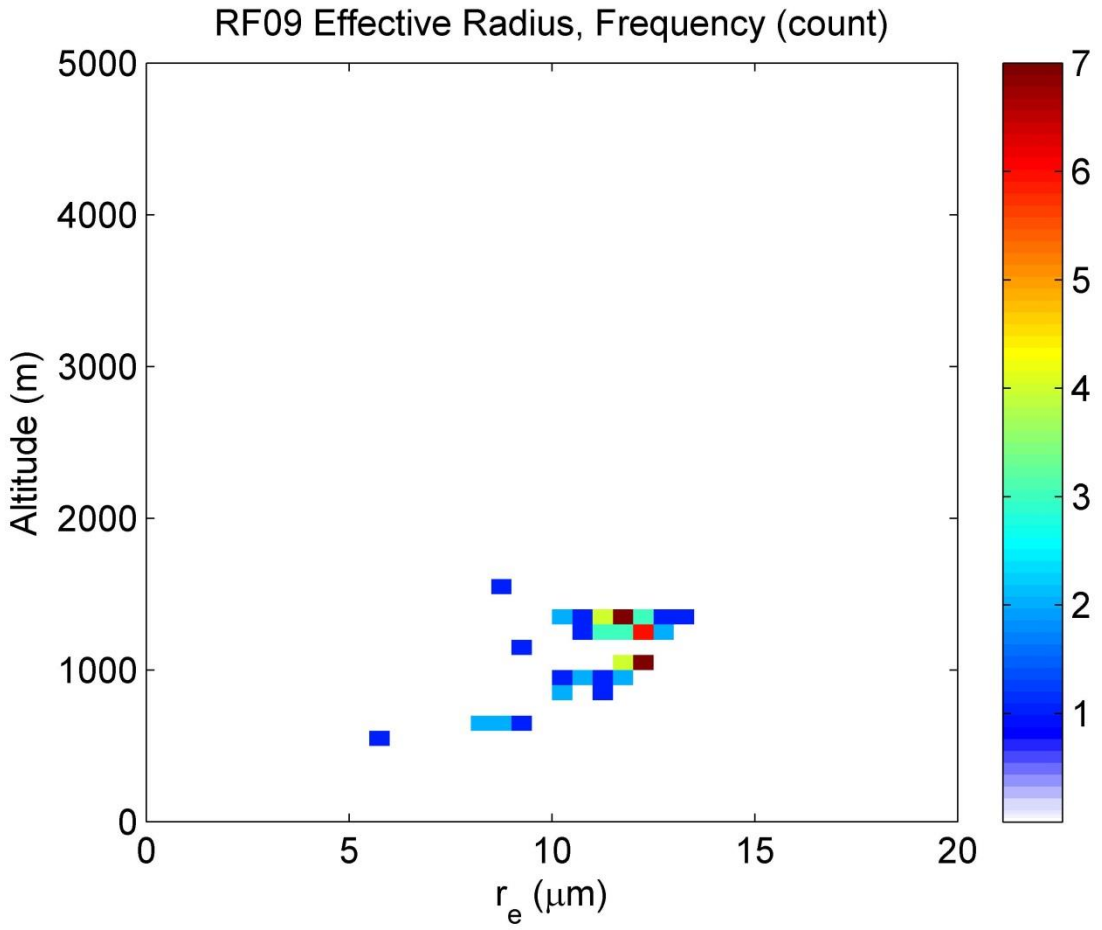

Figure A.7(a) – r_e distribution for RF09, where r_e in μm is on the x-axis, altitude in meters is on the y-axis, and the colors represent the frequency in number of points

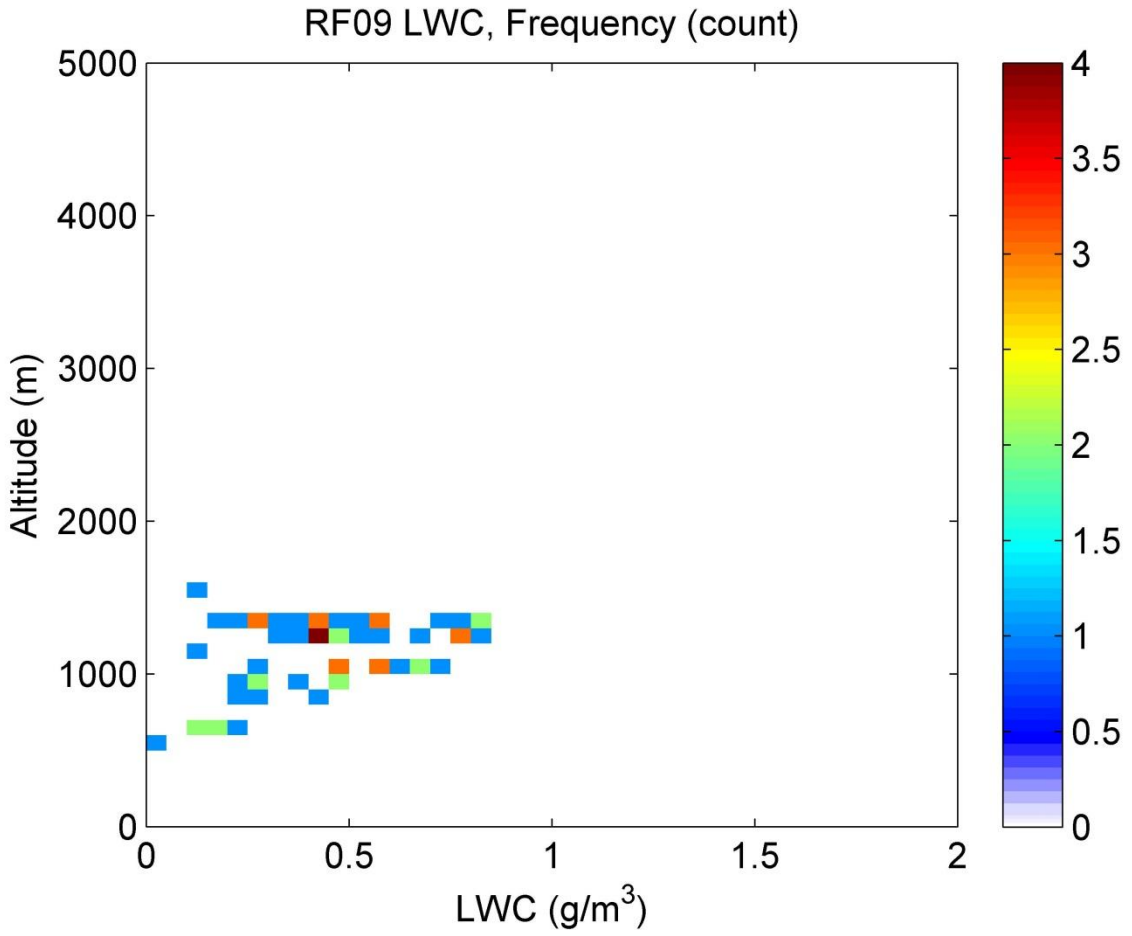

Figure A.7(b) – LWC distribution for RF09, where LWC in g/m^3 is on the x-axis, altitude in meters is on the y-axis, and the colors represent the frequency in number of points.

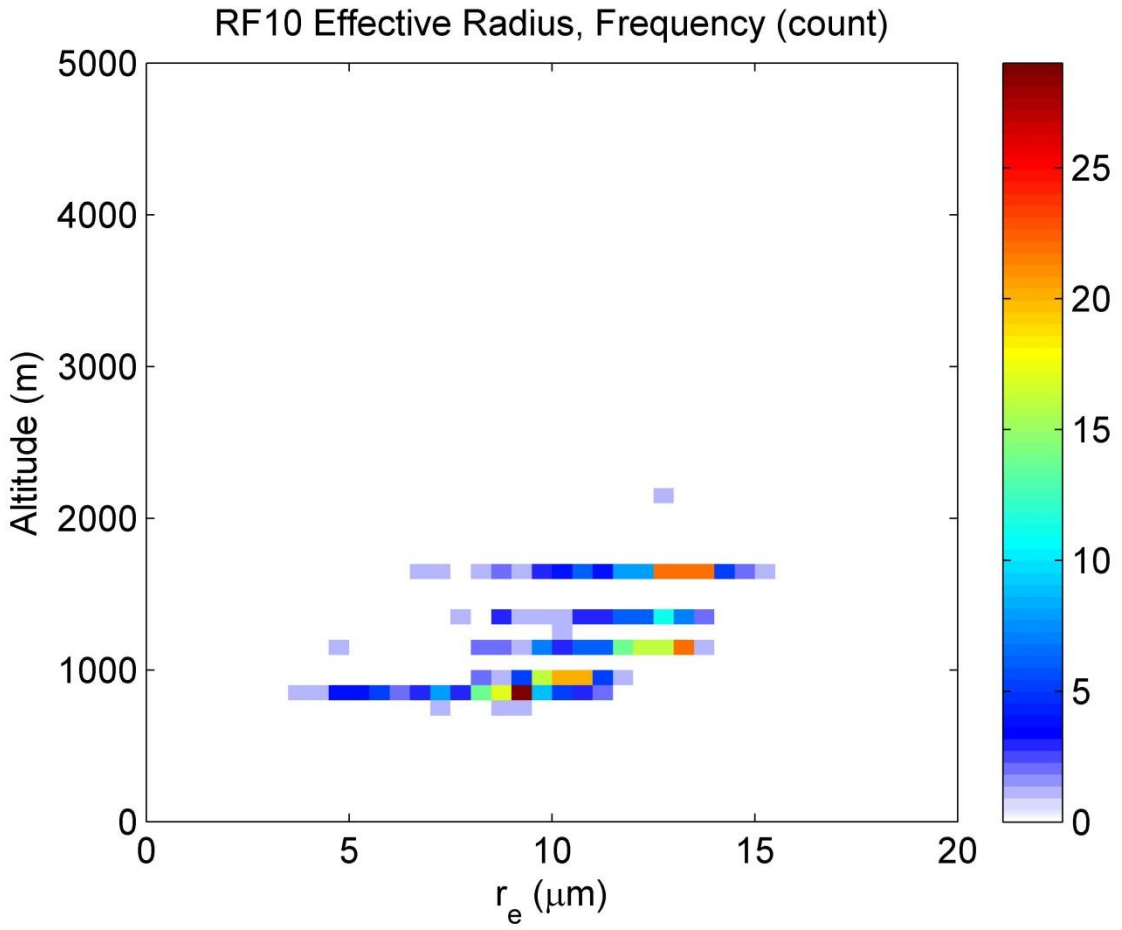

Figure A.8(a) – r_e distribution for RF10, where r_e in μm is on the x-axis, altitude in meters is on the y-axis, and the colors represent the frequency in number of points

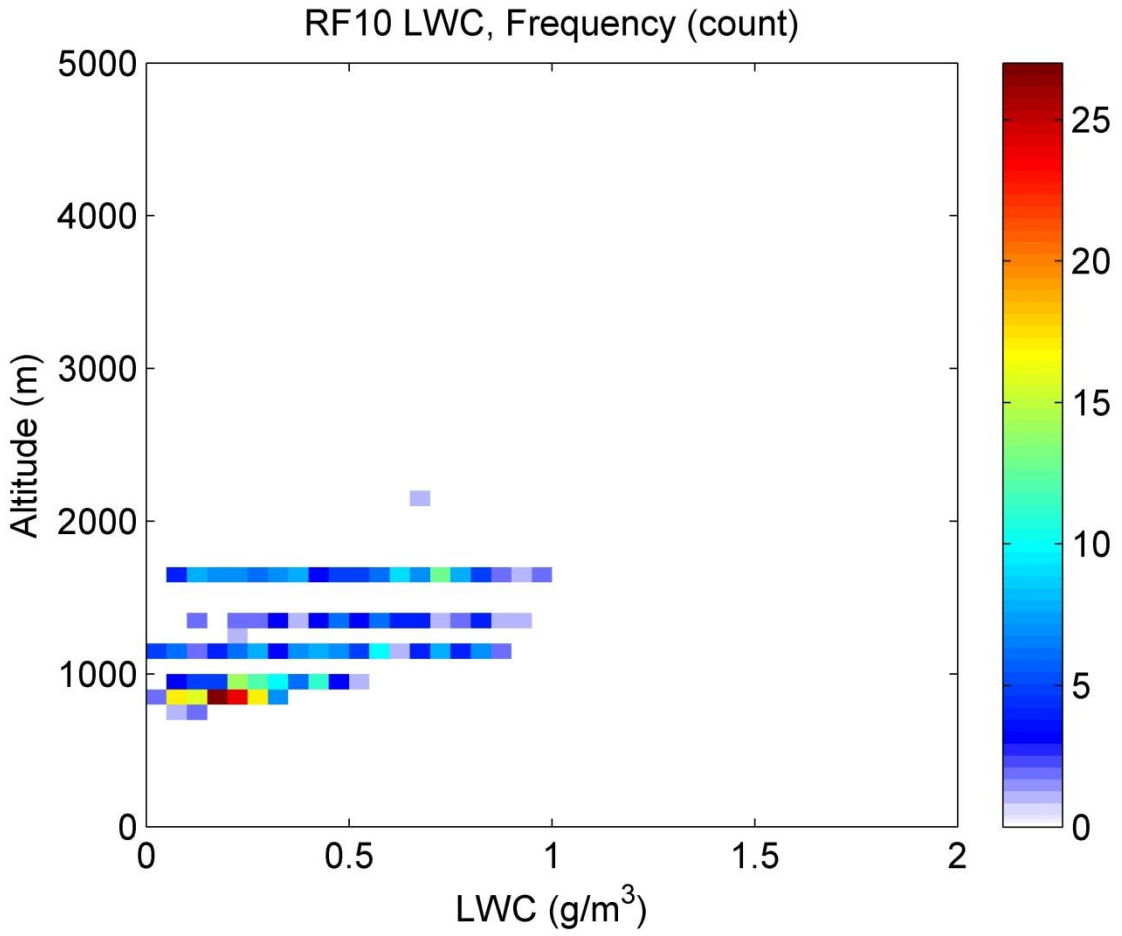

Figure A.8(b) – LWC distribution for RF10, where LWC in g/m^3 is on the x-axis, altitude in meters is on the y-axis, and the colors represent the frequency in number of points.

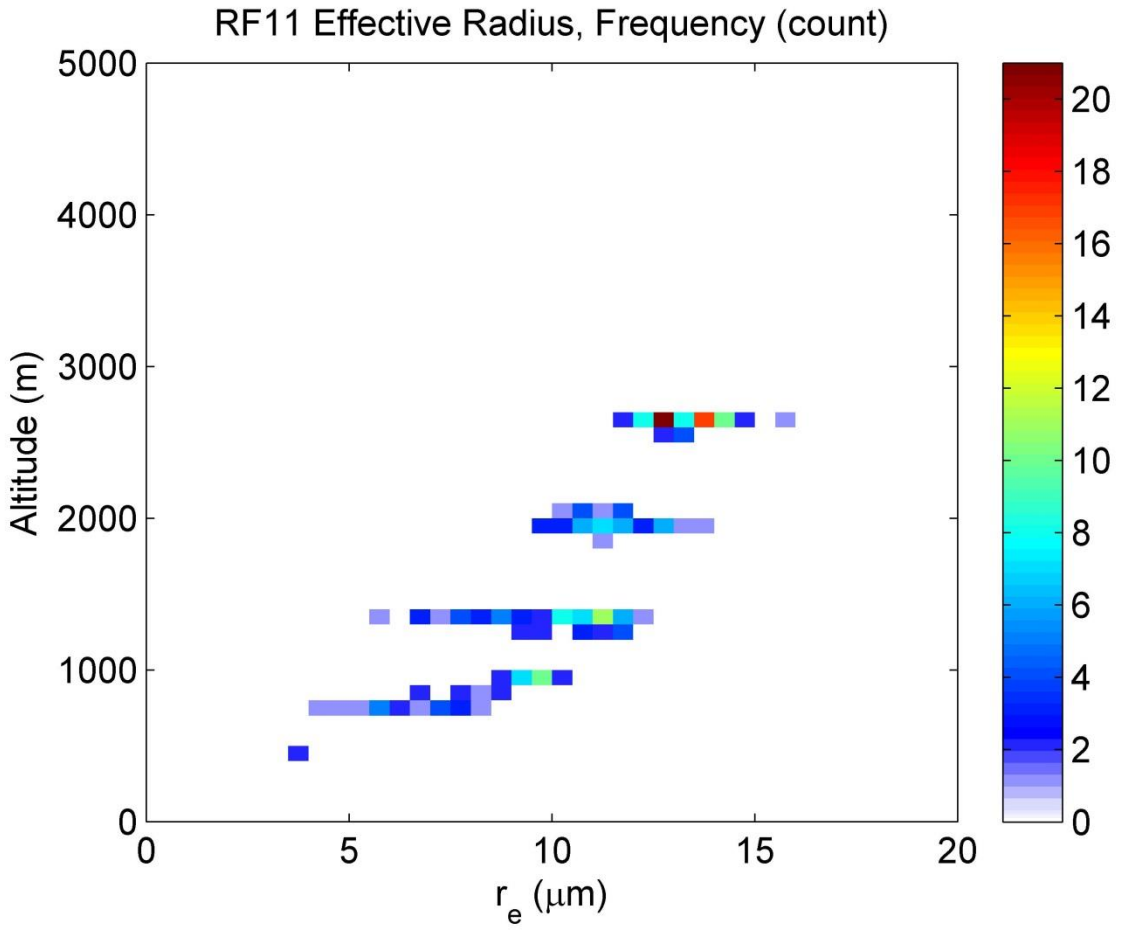

Figure A.9(a) – r_e distribution for RF11, where r_e in μm is on the x-axis, altitude in meters is on the y-axis, and the colors represent the frequency in number of points

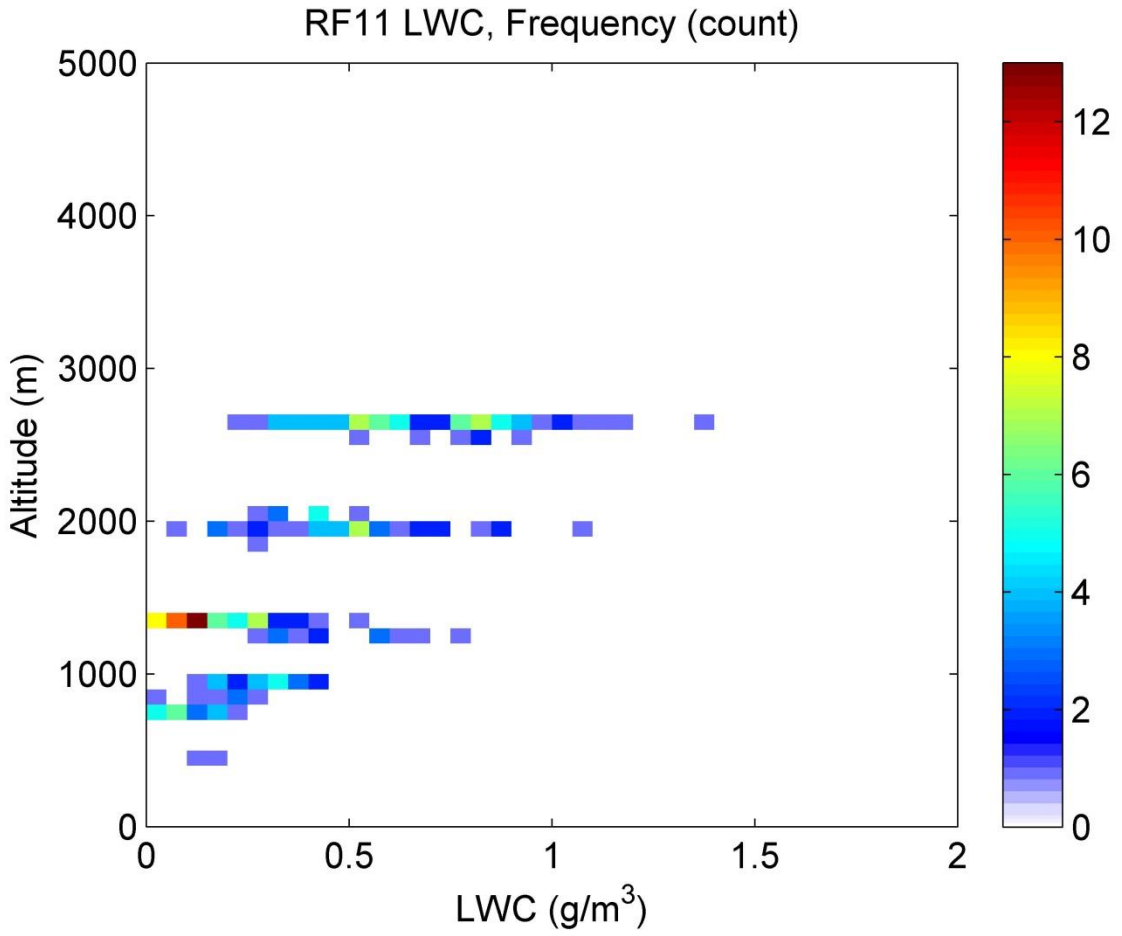

Figure A.9(b) – LWC distribution for RF11, where LWC in g/m^3 is on the x-axis, altitude in meters is on the y-axis, and the colors represent the frequency in number of points.

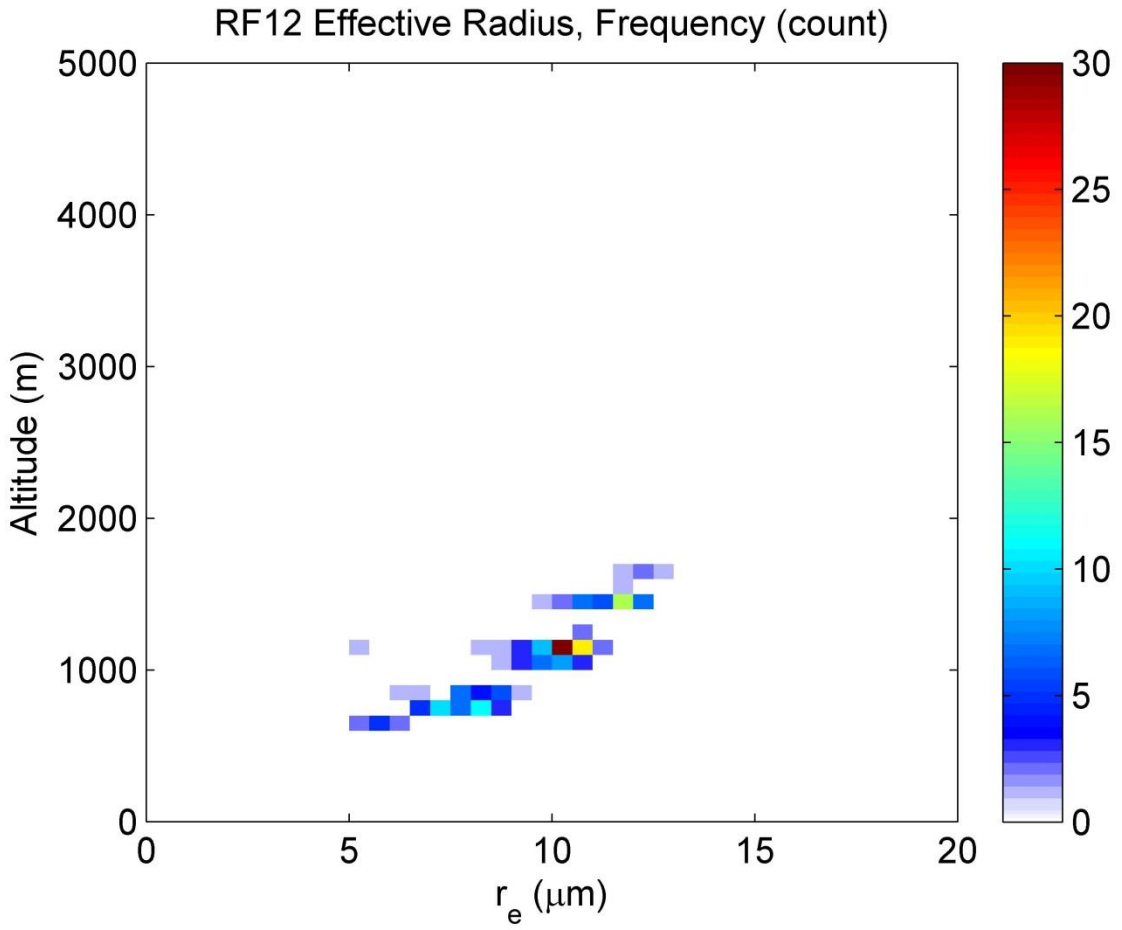

Figure A.10(a) – r_e distribution for RF12, where r_e in μm is on the x-axis, altitude in meters is on the y-axis, and the colors represent the frequency in number of points

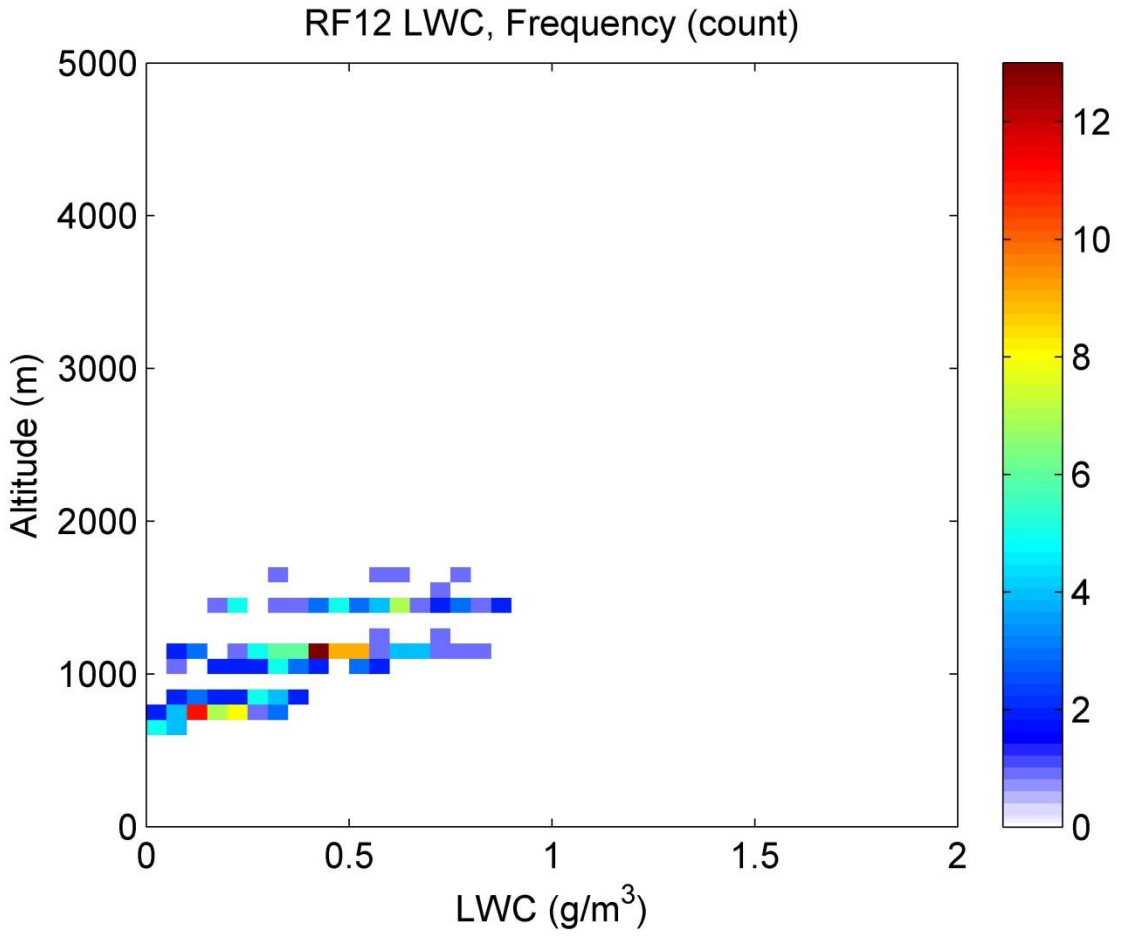

Figure A.10(b) – LWC distribution for RF12, where LWC in g/m^3 is on the x-axis, altitude in meters is on the y-axis, and the colors represent the frequency in number of points.

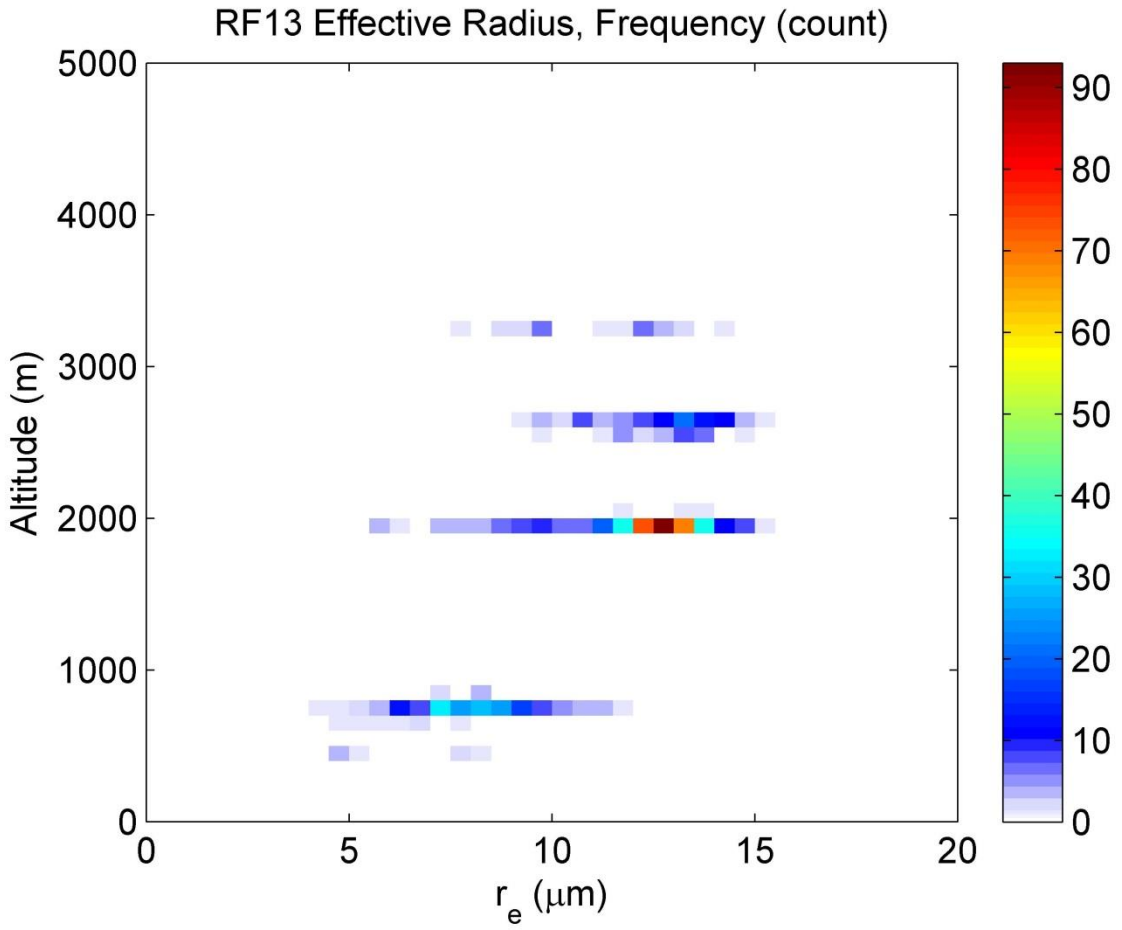

Figure A.11(a) – r_e distribution for RF13, where r_e in μm is on the x-axis, altitude in meters is on the y-axis, and the colors represent the frequency in number of points

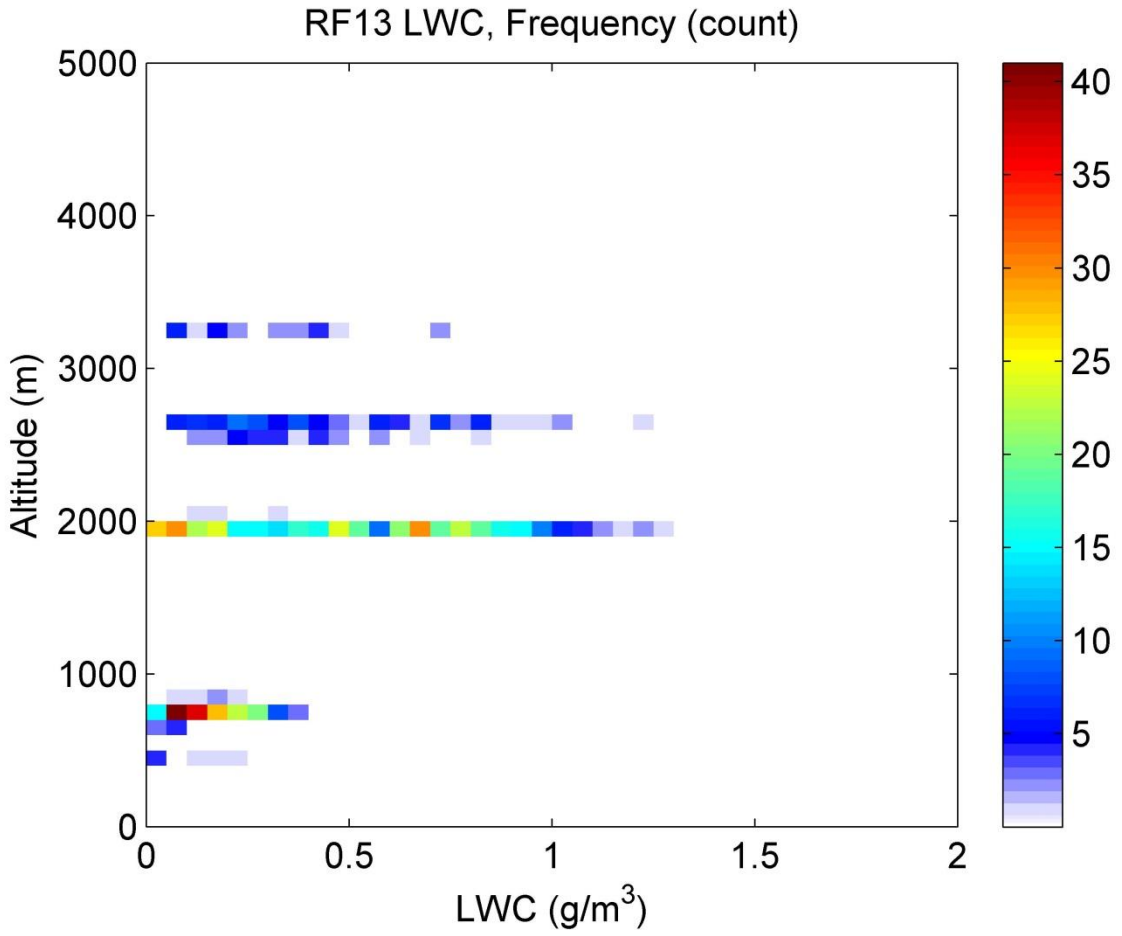

Figure A.11(b) – LWC distribution for RF13, where LWC in g/m^3 is on the x-axis, altitude in meters is on the y-axis, and the colors represent the frequency in number of points.

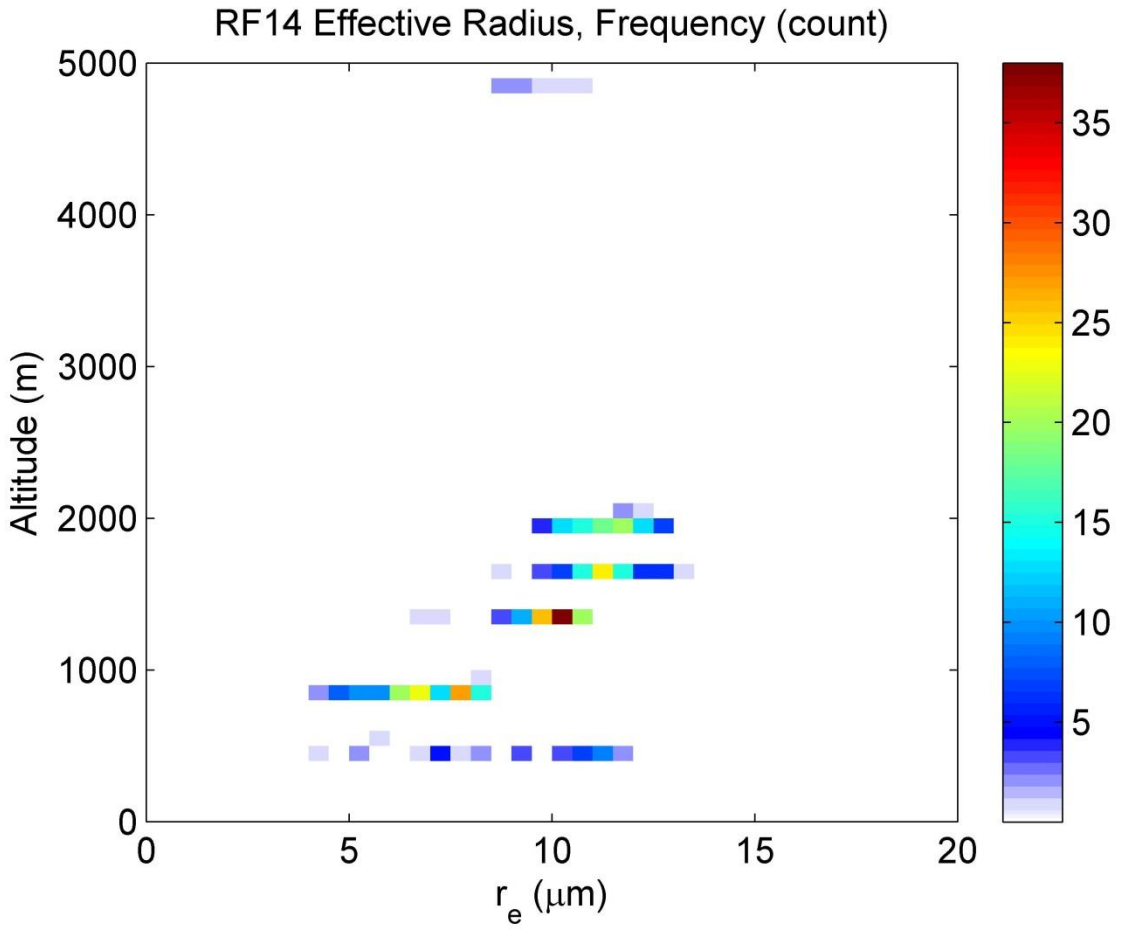

Figure A.12(a) – r_e distribution for RF14, where r_e in μm is on the x-axis, altitude in meters is on the y-axis, and the colors represent the frequency in number of points

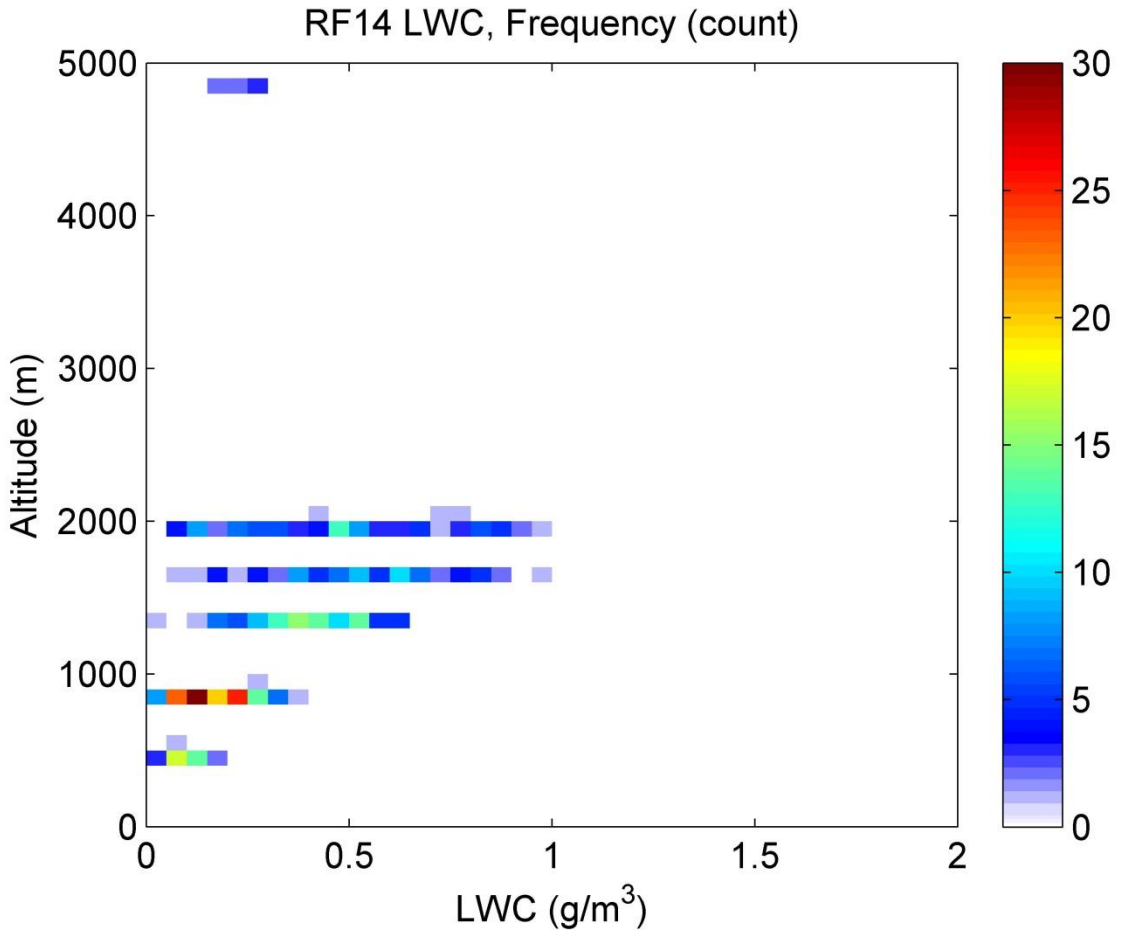

Figure A.12(b) – LWC distribution for RF14, where LWC in g/m^3 is on the x-axis, altitude in meters is on the y-axis, and the colors represent the frequency in number of points.

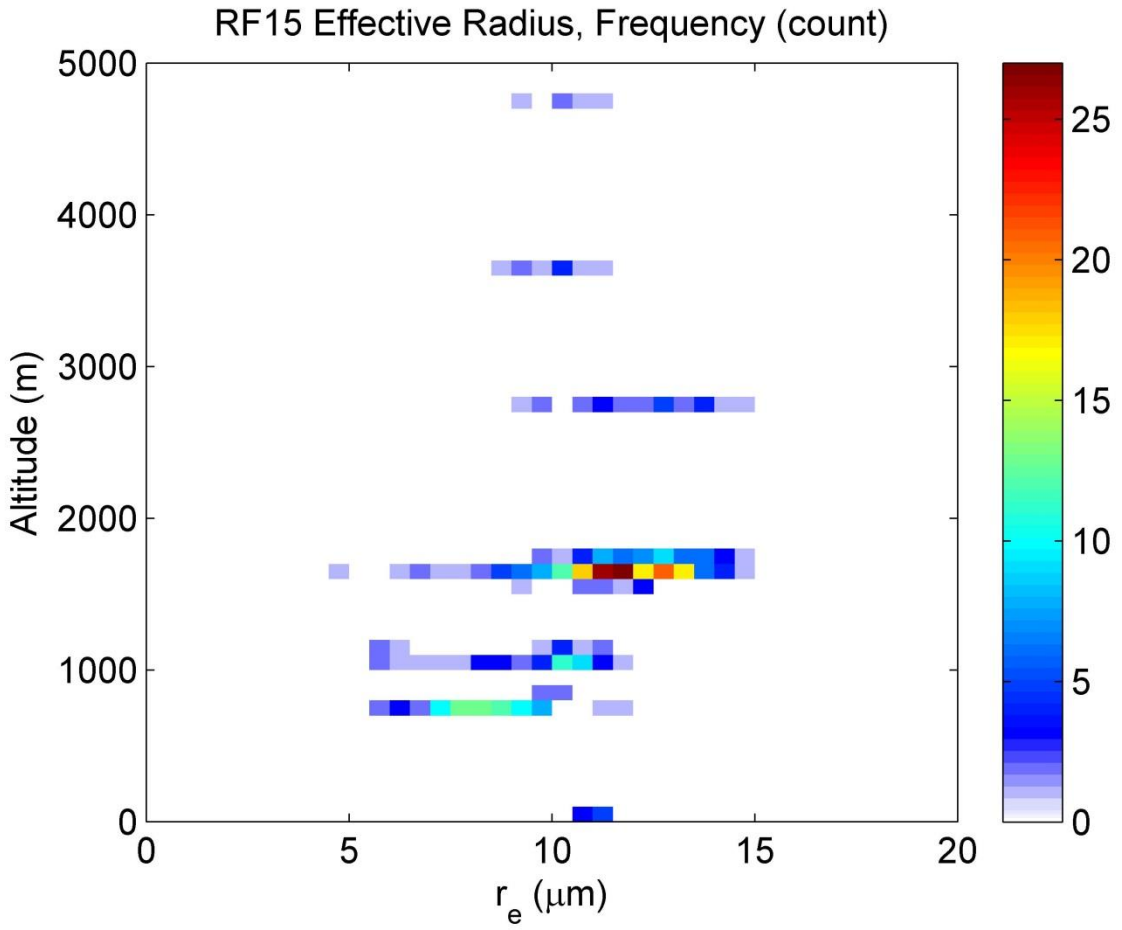

Figure A.13(a) – r_e distribution for RF15, where r_e in μm is on the x-axis, altitude in meters is on the y-axis, and the colors represent the frequency in number of points

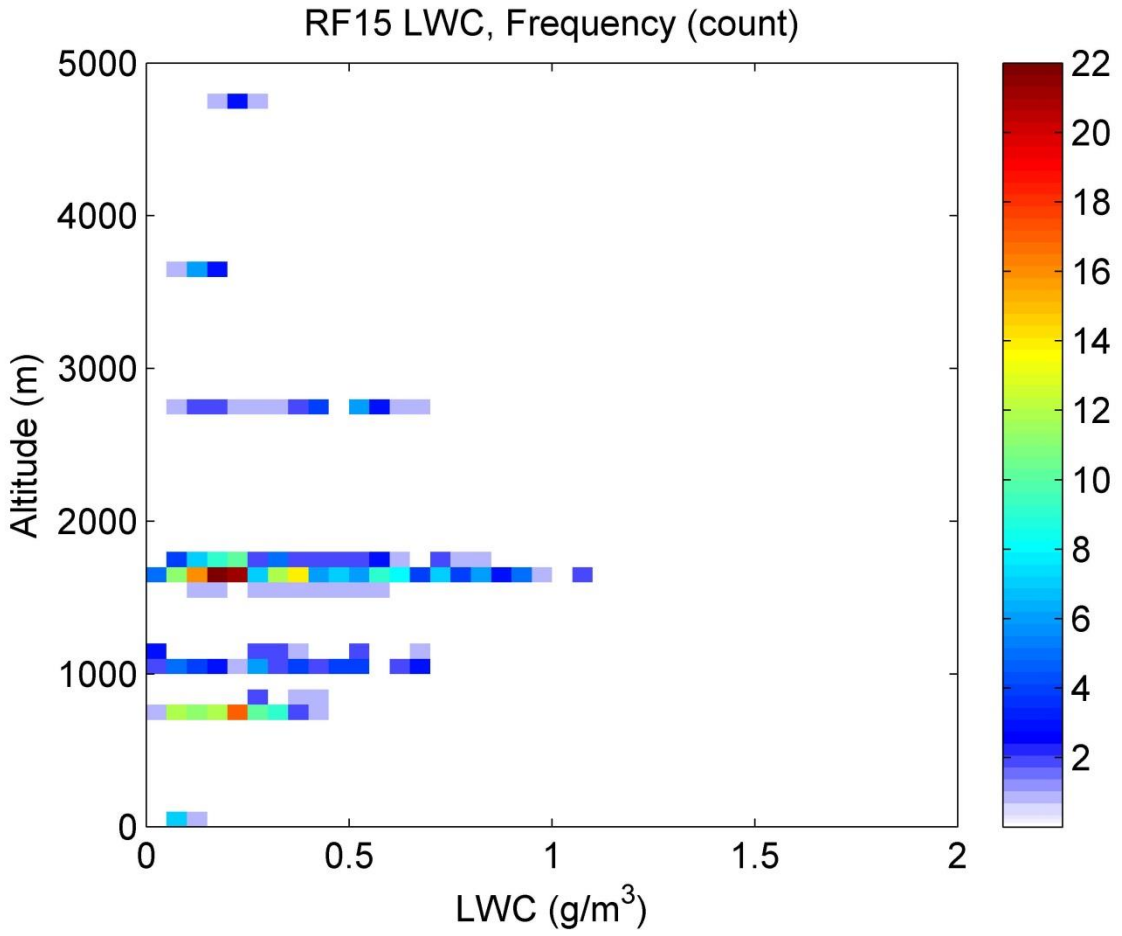

Figure A.13(b) – LWC distribution for RF15, where LWC in g/m^3 is on the x-axis, altitude in meters is on the y-axis, and the colors represent the frequency in number of points.

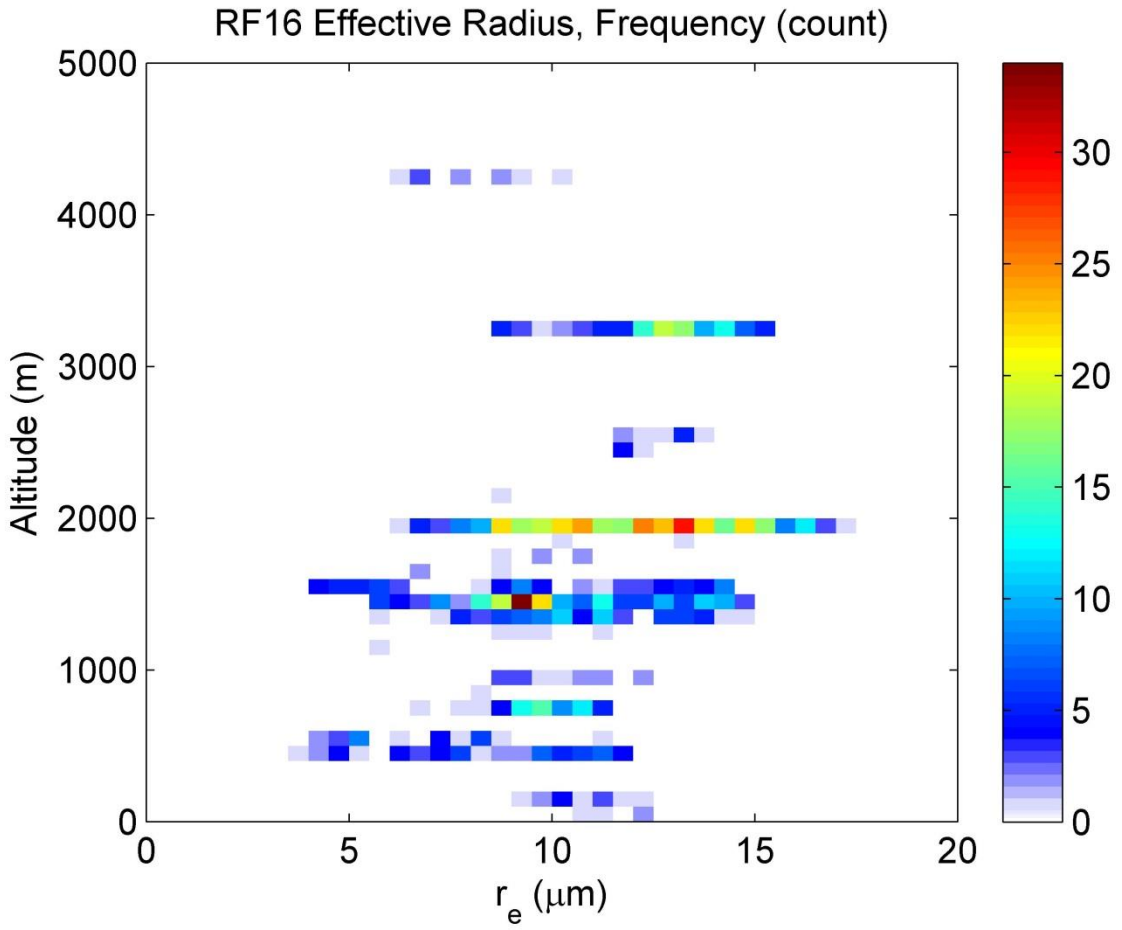

Figure A.14(a) - r_e distribution for RF16, where r_e in μm is on the x-axis, altitude in meters is on the y-axis, and the colors represent the frequency in number of points

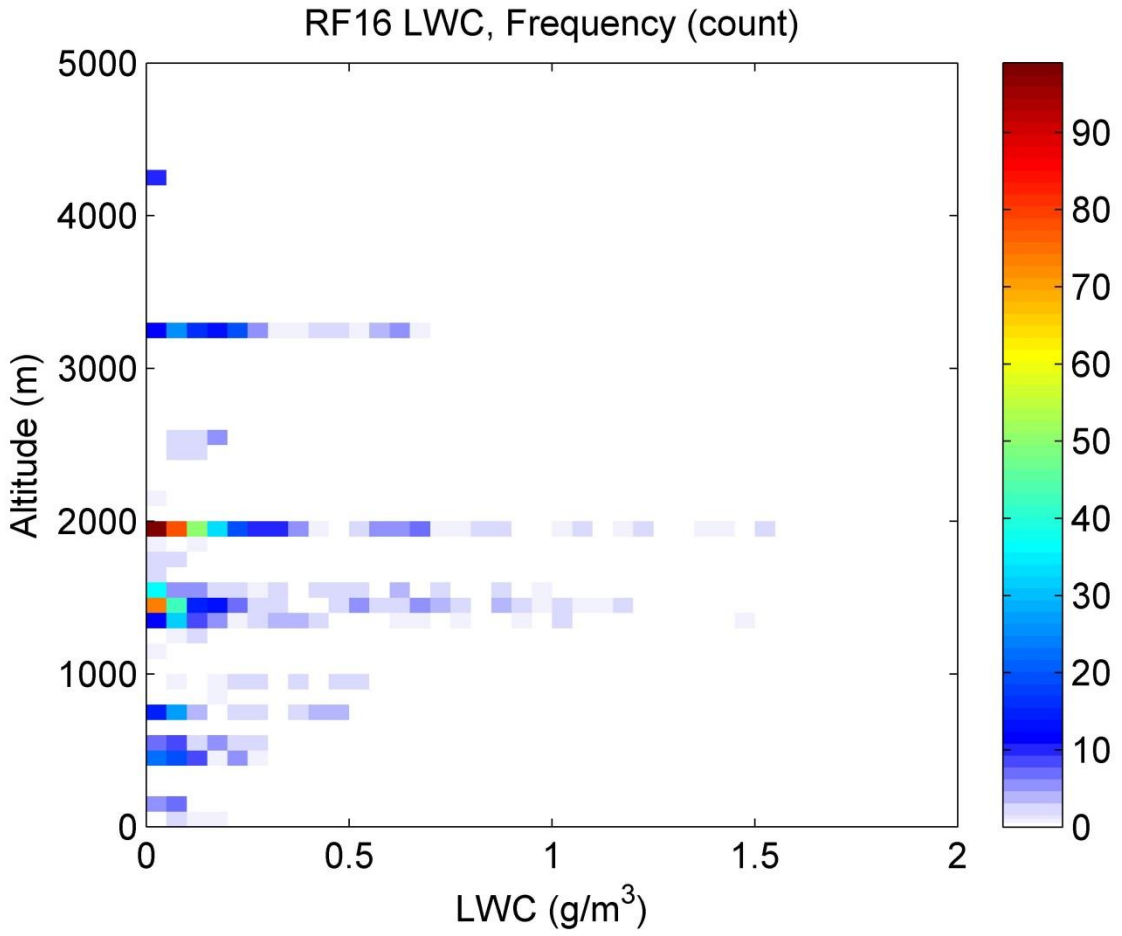

Figure A.14(b) – LWC distribution for RF16, where LWC in g/m^3 is on the x-axis, altitude in meters is on the y-axis, and the colors represent the frequency in number of points.

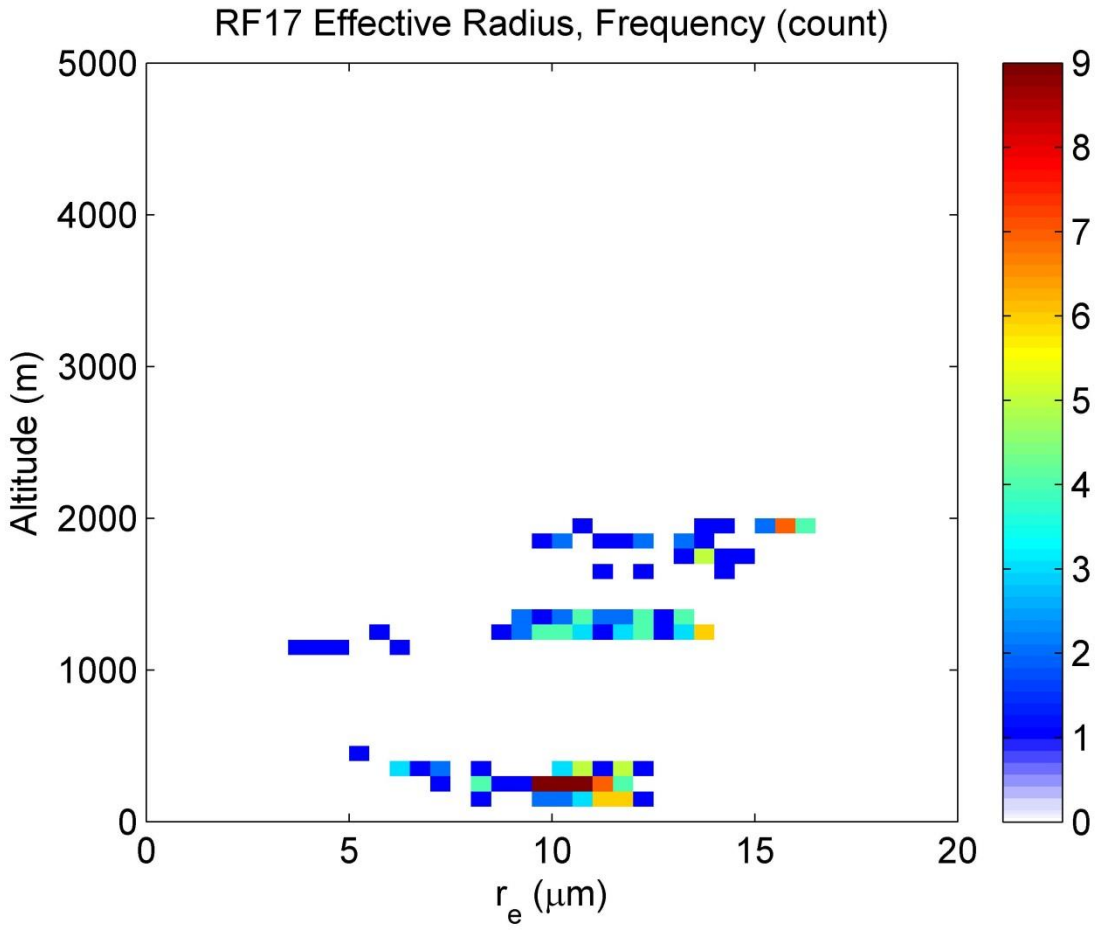

Figure A.15(a) – r_e distribution for RF17, where r_e in μm is on the x-axis, altitude in meters is on the y-axis, and the colors represent the frequency in number of points. This flight was not included in the analysis.

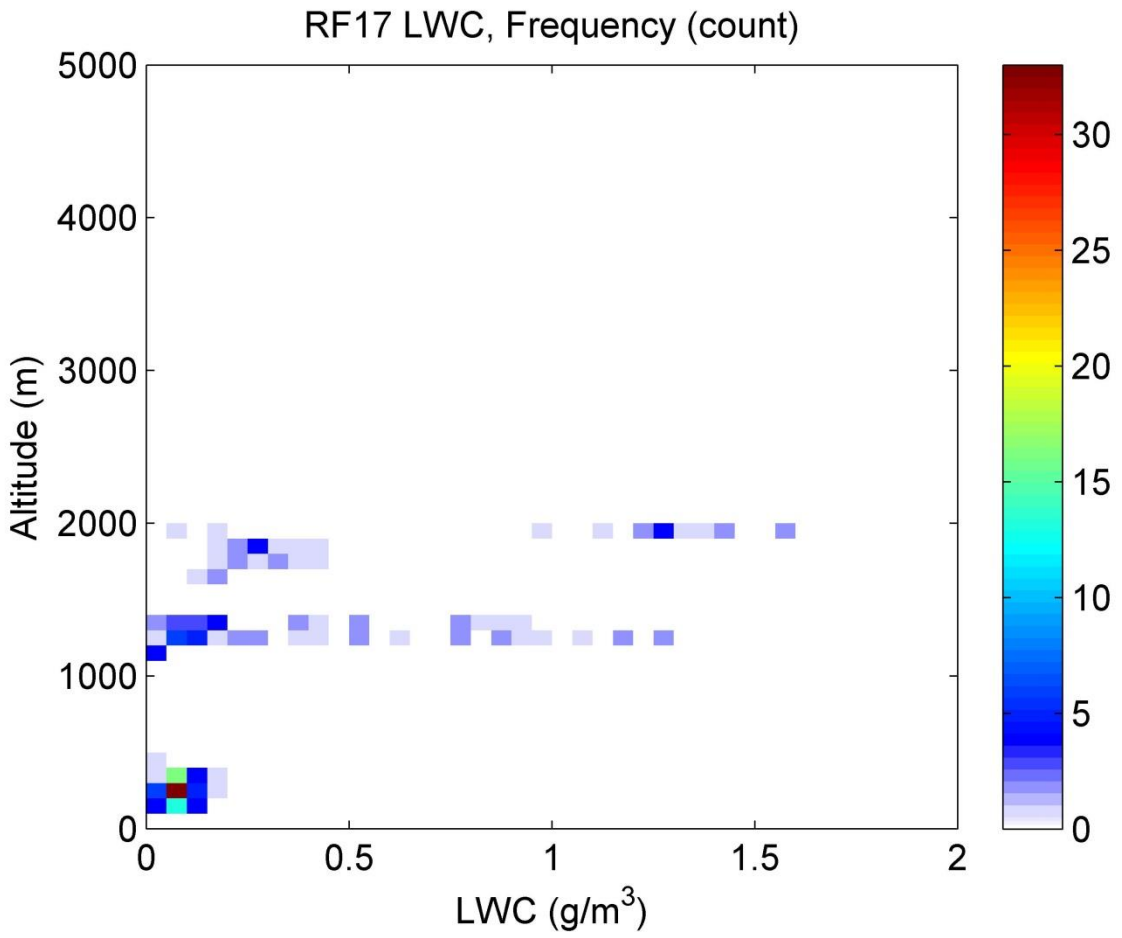

Figure A.15(b) – LWC distribution for RF17, where LWC in g/m^3 is on the x-axis, altitude in meters is on the y-axis, and the colors represent the frequency in number of points. This flight was not included in the analysis.

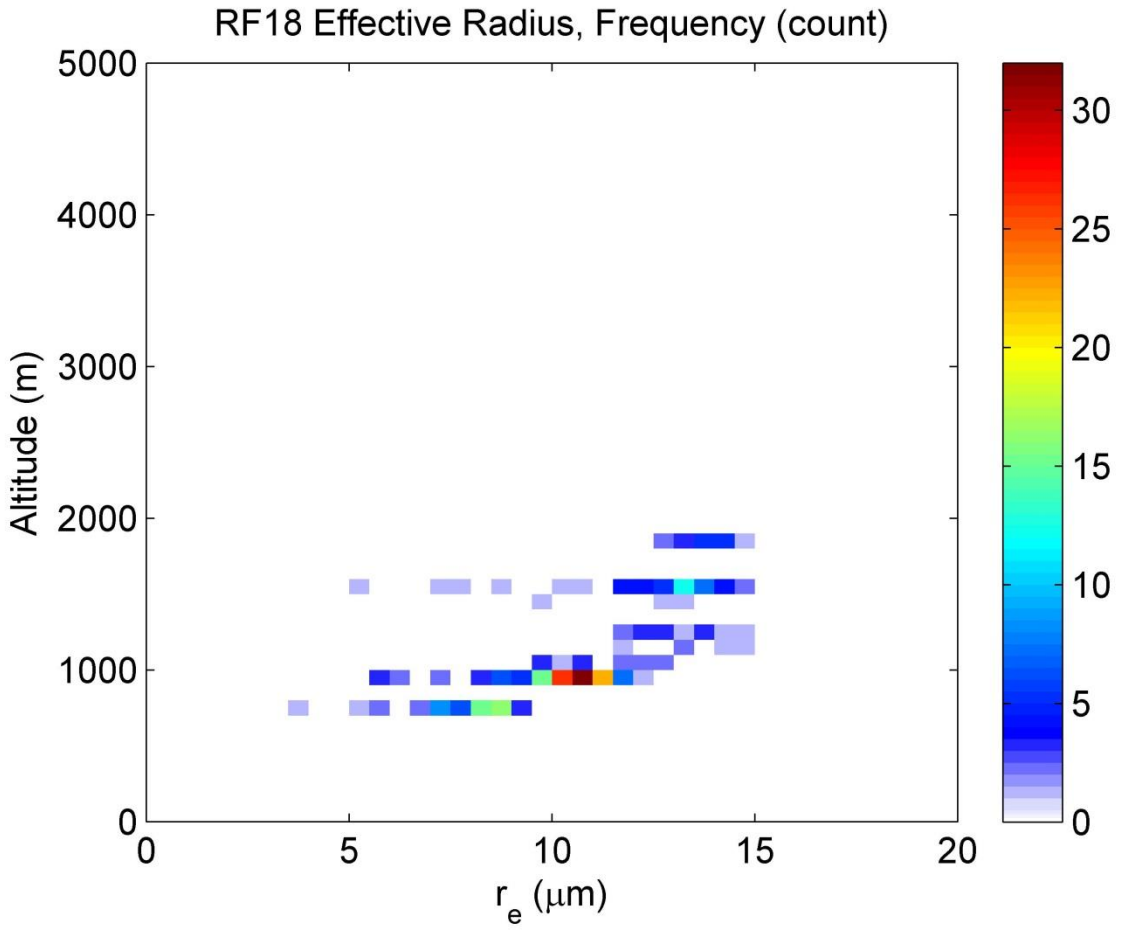

Figure A.16(a) – r_e distribution for RF18, where r_e in μm is on the x-axis, altitude in meters is on the y-axis, and the colors represent the frequency in number of points

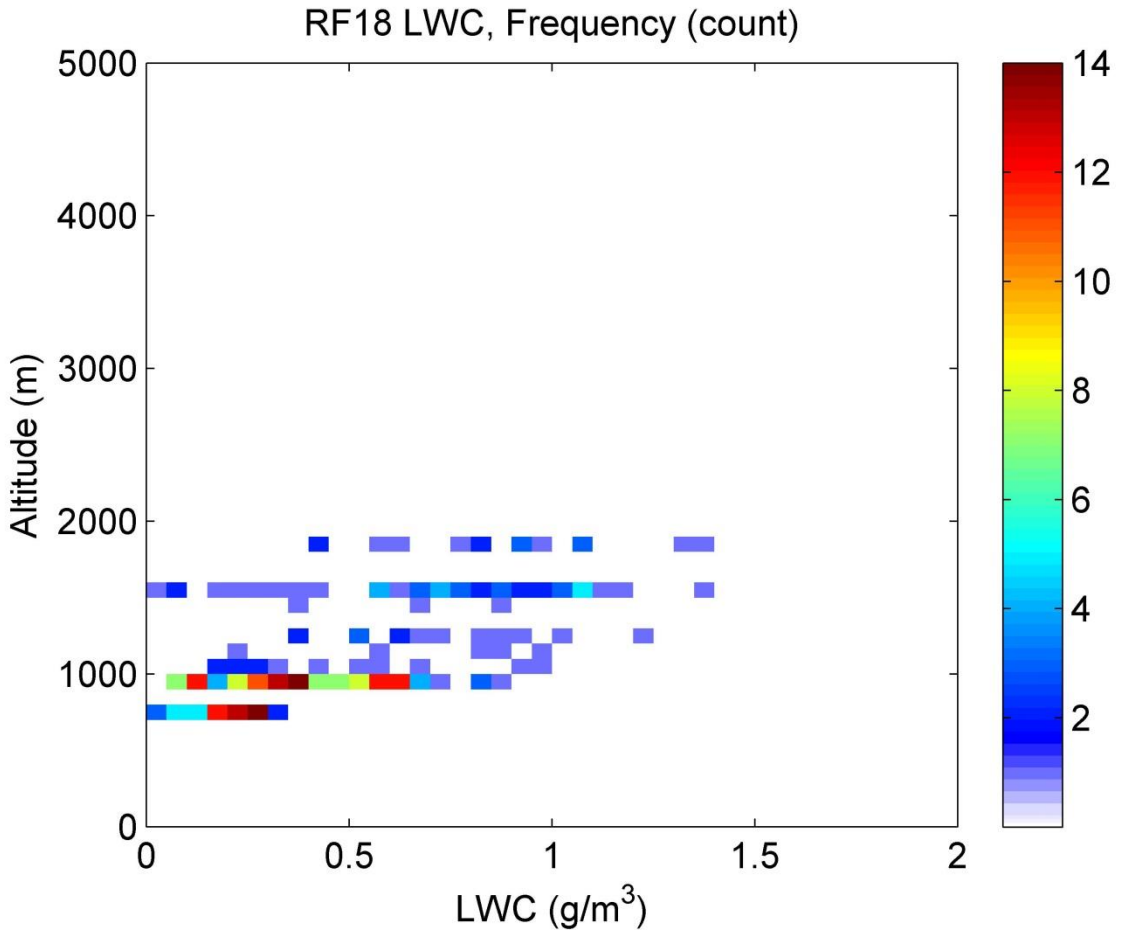

Figure A.16(b) – LWC distribution for RF18, where LWC in g/m^3 is on the x-axis, altitude in meters is on the y-axis, and the colors represent the frequency in number of points.